PHOTOFRAGMENTATION DYNAMICS OF HIGHLY EXCITED DIATOMIC MOLECULES

Photofragmentation dynamics of highly excited diatomic molecules
B.L.G. Bakker
Thesis Katholieke Universiteit Nijmegen - Illustrated
With references - With summary in Dutch
ISBN 90-9014327-0
NUGI 812
Subject headings: velocity map imaging / photofragmentation
excited states / diatom / laser-spectroscopic techniques

Cover: Corridor of the Molecular and Laser Physics Department.
Open door at the right of the frontcover is the room of the author.

PHOTOFRAGMENTATION DYNAMICS OF HIGHLY EXCITED DIATOMIC MOLECULES

EEN WETENSCHAPPELIJKE PROEVE OP HET GEBIED VAN
DE NATUURWETENSCHAPPEN, WISKUNDE EN INFORMATICA

PROEFSCHRIFT

TER VERKRIJGING VAN DE GRAAD VAN DOCTOR
AAN DE KATHOLIEKE UNIVERSITEIT NIJMEGEN,
VOLGENS BESLUIT VAN HET COLLEGE VAN DECANEN
IN HET OPENBAAR TE VERDEDIGEN
OP WOENSDAG 10 JANUARI 2001,
DES NAMIDDAGS OM 1.30 UUR PRECIES

DOOR

BERNARDUS LEONARDUS GERARDUS BAKKER

GEBOREN OP 21 DECEMBER 1973
TE NIJMEGEN

PROMOTORS : PROF. DR. D.H. PARKER

PROF. DR. W.J. VAN DER ZANDE

MANUSCRIPTCOMMISSIE : PROF. DR. J.J. TER MEULEN

PROF. DR. T.N. KITSOPOULOS
UNIVERSITY OF CRETE, HERAKLION

DR. M.C. VAN HEMERT
UNIVERSITEIT LEIDEN

This work is part of the research program of the “Stichting voor Fundamenteel Onderzoek der Materie” (FOM), which is financially supported by the “Nederlandse organisatie voor Wetenschappelijk Onderzoek” (NWO).

I love it when a plan comes together
George Peppard, as Colonel John "Hannibal" Smith in "The A-Team"

Voorwoord

Eindelijk is het dan zover dat u zich in dit proefschrift te goed kunt doen aan, hopelijk, leuke en interessante wetenschap. Dus een advies van mijn kant is dan ook om het niet te laten zitten bij het gebruikelijke “alleen maar” lezen van dit voorwoord, maar om ook eens wat verder te bladeren. In dit proefschrift worden immers de resultaten beschreven, die ik met de hulp van vele anderen heb verkregen. Ik wil daarom dan ook iedereen bedanken die maar enigszins geholpen heeft bij de totstandkoming van dit proefschrift. „Applausje voor je zelf”, zou meneer Kaktus dan zeggen en daar sluit ik me geheel bij aan. Toch wil ik de volgende mensen, in willekeurige volgorde, specifieker bedanken.

Allereerst wil ik David Parker bedanken voor de kans die hij mij geboden heeft om mijn afstudeerstage uiteindelijk voort te zetten als OIO. Tevens wil ik hem bedanken voor zijn begeleiding en hulp bij de totstandkoming van dit proefschrift.

Mijn tweede promotor Wim van der Zande verdient dank voor zijn goede raad en enthousiaste kijk op de wetenschap. Hierdoor stimuleerde hij mij enorm.

Ook wil ik de leden van de manuscriptcommissie bedanken voor het controleren van het manuscript en het geven van suggesties voor verbeteringen wat geleidt heeft tot dit uit eindelijke proefschrift. Ik wil nog een paar mensen specifieker vermelden.

Ik wil Hans ter Meulen bedanken voor zijn nimmer aflatende interesse in mijn werk en het voor feit dat hij mij net dat zetje gaf waardoor ik toch ben gaan promoveren. Ook is hij iemand waar ik op terug kon vallen.

Ik wil ook Theofanis Kitsopoulos bedanken, zijn AIO Petros Samartzis en technicus Apostolis Egglezis voor een leuk en zeer productief verblijf op Kreta. Thank you Theo for allowing me to play with your setup. It was good fun on Crete and we also produced nice results. Petros, thanks for giving me a nice time in the lab and for your short introduction to Greek culture: Δὺο φραπὲ, γλυκοὺς με γὰλα . And of course Apostolis who kept the lasersystem running and changes laserpulsewidth in a blink of an eye. Σας ευχαριςτὼ ὁλους.

Ik heb zelf ook werkbezoek gehad van gasten: Grant Ritchie uit Oxford, Liam McDonnel en Albert Heck uit Warwick, Benoit Soep en Niloufar Shafizadeh uit Parijs, Hans-Peter Loock uit Kingston, Pietro Candori uit Perugia, Pablo Quintana uit Madrid, Andrě Eppink uit Bielefeld en Eric Gloaguen uit Parijs. Thank you all.

Zonder technische ondersteuning ben je als experimentator helemaal nergens. Ik wil allereerst Cor Sikkens bedanken voor zijn hulp en advies bij het instandhouden en verbeteren van de opstelling. Cor staat altijd klaar met raad en daad. Vooral aan de discussie over honden- en kattenmensen op Sinterklaasavond tijdens het ontmantelen van een oude en verdachte gasfles vol 100% zoutzuur denk ik met veel plezier terug. Ook de electronische hulp van Chris Timmer was onmisbaar; met name zijn snelle reparaties en goed werkende apparatuur zullen mij bij blijven. Ook wil ik Eugěne van Leeuwen bedanken voor zijn hulp en anekdotes over de totstandkoming van de opstelling. Voor de secretariële ondersteuning wil ik Magda Speijers bedanken. Zij wist me altijd door de kluwe van formuliertjes en bureaucratie te loodsen. Ik bedank Nico Dam voor zijn hulp bij het afstembaar maken van de ArF excimer laser. Ik wil mijn (oud)collega's van de afdeling Molecuul & Laserfysica bedanken voor de gezelligheid in de koffiehoek, bij borrels en in de mensa: Michiel, Giel, Rik, Rick, Iulia, Peter, Simona, Floris, Ralph, Gijs, Leander, Frans, Maarten, Rienk, Martina, Luc-Jan, Eugène, Sacco, Leo, Gerard, Ine, Grzegorz, David, Stefan, Rudy, Jörg, Hans, André, Edi, Cor, Magda, Izabela, Brenda, Kasper, Monique, Nico, Ivan, Marianna, Raluca, Tim, Jan-Mathijs, Chris, Robert, Frank, Sergio, Rogier, Hans, René, Robert, Mike, Deniz, Gert, Wim, Bas, Jos, Rob, Tim, André, Karen, Erik-Jan, Richard, Nicholas, Iwan, Andrei, Jack, Koen, Charles, Genie, Karen, Rob etc. Harstikke bedankt voor de fijne tijd.

Twee jaar geleden kreeg ik een heuse collega in de vorm van een post-doc, Ralph Delmdahl genaamd. Ralph ging voortvarend te werk in het lab, zodat ik mij meer kon toeleggen op het schrijven. Ik heb veel van Ralph geleerd en het was altijd kei gezellig in onze kamer. Ik zal vooral zijn fascinatie met de Nederlandse taal niet vergeten, zoals het verhaal over "Rupsje NooitGenoeg". Bij deze tevens mijn welgemeende excuses voor mijn grapjes over de Duits-Nederlandse verhoudingen. Herzlichen Dank, Ralph.

Daarnaast mijn dank voor een paar mensen die onder mijn kamerregime hebben geleden: Stefan Persijn en Sergio Velazquez. Zo kon ik Sergio accentloos leren hoe hij mij "onbvesjgoft" kon noemen. Stefan wist mij altijd op te beuren met zijn favoriete uitspraak: "Het valt allemaal best wel mee!". Ook het opfleuren van mijn computerscherm met kakkerlak-karkassen, zal mij altijd bijblijven. "Muchas gracias" Sergio en "Veel dank" Stefan voor een onvergetelijke tijd op pakweg 30 vierkante meter. Een andere kamergenoot, mijn voorganger André Eppink, wil ik bedanken voor zijn blijvende aandacht voor het onderzoek.

Een belangrijke wetenschappelijke sparringpartner was Michiel van Beek voor mij. De vele discussies, tips en raad hebben me veel geholpen. Het was altijd fijn om even de afdeling af te lopen en tegen Michiel te kunnen zeuren over de gang van zaken. Het was tevens genoegelijk dat dit buiten het hek, samen met zijn vrouw Marieke, voortgezet kon worden. Vooral zijn heldhaftige optreden tegen de killer-eekhoorns in Bristol sierde hem. Ik ben dan ook zeer vereerd dat hij mijn paranimf wil zijn.

Tijdens de eerste avond van de introductie van Natuurkunde in 1992 liep ik een medestudent tegen het lijf waarmee het meteen klikte. Sindsdien waren André van Hameren en ik een soort Bert en Ernie in de Sesamstraat van de Natuurkunde. Ik had ook de vergelijking kunnen maken met Narziss en Goldmund uit het gelijknamige boek van Hermann Hesse, maar dat staat zo betweterig. Hoe dan ook, tijdens de studie was het al leuk, maar tijdens de promotie was het nog leuker. Ik ging knutselen bij de lasercowboys en André programmeren en integralen oplossen bij theoretische hoge-energiefysica. Deze uitersten in de wetenschap kwamen zeer goed tot hun recht tijdens de lunch, avondeten of bierproeverijen. Vooral Andrés eigenschap, dat hij altijd achter me staat, heeft me altijd, en specifiek tijdens deze promotie, geholpen. Hij is dan ook de uitgelezen persoon om mij bij te staan als paranimf.

Mensen die nog langer mijn "school"carrière hebben gevolgd zijn Günther Rensen en Erik van Deelen. Zij moesten in hun vrije tijd aanhoren, hoe groot het tranendal van een promovendus met opstelling is. Bij opmerkingen zoals: "Mijn Nd:Yag laser geeft te weinig milliJoule per puls" of "Ik moet weer naar Lunteren", wisten ze me toch nog altijd aandachtig en vol interesse aan te staren. Ook al wist ik dat ze er geen touw aan vast konden knopen. Dit kon trouwens ook liggen aan het vermaarde “zwaargewichten”biermenu van café Jos. Ze vroegen me altijd hoe het stond met het onderzoek en de artikelen en wisten mij ten alle tijde weer moed in te praten, anders was dit boekje nu nog niet af geweest. Nogmaals, bedankt.

Edith Dutmer stond altijd klaar met haar luisterend oor en gezelligheid. De chaos op het lab was zo snel vergeten. Ook werkt haar speciale taaltje zeer opmonterend in zware tijden, vooral in combinatie met zelfgemaakte wereldgerechten.

Ik wil mijn ouders bedanken voor alle steun, die ze me van begin af aan gegeven hebben. Ik kreeg weliswaar op mijn twaalfde verjaardag geen laseropstelling, maar ik denk toch dat ze me goed op deze aardbodem hebben neergezet.

Mijn broertje Richard en zusje Leonie met vriend Rens, wil ik ook graag bedanken. Zij toonden altijd interesse voor mijn onderzoek. Dat ging zelfs zo ver dat ze een keer op bezoek zijn gekomen op het lab. Ze waren vooral onder de indruk van het staal, de oliegeur en het lawaai. Dan moet je echt wat voor je grote broer over hebben! Ik kon lekker stoer doen door kleurtjes uit lasersystemen te toveren, wat zelfs nog meer indruk maakte.

Tevens wil ik mijn “schoonouders” bedanken voor de aandacht en het geduld, omdat ik toch maar 4 jaar heb verbruikt in plaats van gelijk een “echte” baan te zijn gaan zoeken. Voornamelijk per telefoon, bleven ze voortdurend op de hoogte vanwege de nog niet doorgetrokken A73.

Ik wil vooral Karin bedanken. Zij stond altijd voor me klaar en was dè grote steun voor mij. Toen ik mijn nieuwe blouse in het lab had verpest, kon ze er zelfs om lachen. De 10 Hz laser had witte puntjes erin gebrand en met de onderlinge afstand, kon ik de snelheid bepalen, waarmee ik door de laserstraal was gelopen. Een ieder ander was gelijk gillend weggelopen.
Karin, dit proefschrift is nu af, maar jij maakt alles echt compleet.

Bernard Bakker, Nijmegen, oktober 2000

Contents

Chapter 1

Introduction

Abstract

Fragmentation processes of photoexcited states in diatomic molecules are investigated in this thesis. A common decay mechanism is the breaking of the bond between the two atoms releasing two radicals after the absorption of a photon; a process known as photodissociation. Other possible processes, like ionization and dissociative ionization, will also be examined and treated in this thesis. All these processes play important roles in the photochemistry of atmospheres, in combustion and in interstellar space. This thesis deals with the investigation of different diatomic molecules irradiated with different wavelengths of pulsed light and characterizes the produced fragments in order to gain more insight into the different types of fragmentation decay mechanisms. The method of choice is the combination of lasers and the technique "velocity map imaging". This technique is very powerful and well suited for studying fragmentation processes of molecules. Lasers produces light with well known energy and polarization and are used to populate the specific excited state in the molecule. The "velocity map imaging" technique yields a two-dimensional representation of the velocity vectors of the formed fragments (also known as an image) that incorporates the angular distributions and kinetic energy distributions of these fragmentation products. These distributions provide a way for distinguishing the various fragmentation processes that the highly excited diatom suffered. This chapter will introduce the reader into these concepts in order to better understand the experimental results presented later in this thesis.

1.1 Interaction of light in diatomic molecules

A photon has two important properties, which influence a molecule after absorption; energy and angular momentum. The energy of the photon E_{photon} is given by $E_{photon}=\hbar\omega$, where $\hbar$ is Planck's constant and ω the angular frequency of the light. This energy can be used to raise the internal energy $E_{\rm int}$ of the diatom. This internal energy is divided in a first approximation in three types of energies: electronic energy $E_{\rm el}$, vibrational energy $E_{\rm vib}$ and rotational energy $E_{\rm rot}$. One of the electrons that orbit around the two nuclei absorbs the energy of the light and occupies a higher orbit, increasing the electronic energy $E_{\rm el}$ of the molecule. If we think of the diatomic molecule as two balls connected by a spring, the other energy types can be visualized. The diatom will vibrate when one moves the atoms along the internuclear axis. The energy involved is given in first order by $E_{\rm vib}=({\rm v}+\frac{1}{2})\hbar\omega_e$, where v is the vibrational quantum number and only has integer values 0,1,2,etc. The symbol ω_e is known as vibrational constant and it varies with different molecules [1]. The last mentioned energy is when the molecule rotates in the plane of the internuclear axis. The rotational energy is then given in first order by $E_{\rm rot}=J(J+1)\hbar B_e$, where J is the rotational quantum number and it also can only have integer values 0,1,2,etc. The constant B_e is the rotational constant that also depends on the type of diatomic [1]. Typical energy regions for the different types of energies are: $E_{\rm el}$ ~5 eV~40000 $\rm cm^{-1}$, $E_{\rm vib}$ ~[1000-2000]$\rm cm^{-1}$, $E_{\rm rot}$ ~[2-20]$\rm cm^{-1}$, where 1 eV = 8065 $\rm cm^{-1}$ = $1.602\ 10^{-19}$ Joule. The partitioning of the internal energy in the molecule can be summarized as followed:

$$E_{\rm int} = E_{\rm el} + E_{\rm vib} + E_{\rm rot} = E_{\rm el} + ({\rm v} + 1/2)\hbar\omega_e + J(J+1)\hbar B_e \tag{1.1}$$

Another quality of the absorption of light is that it changes the angular momentum properties of the molecule. The angular momentum properties of the molecule can be described with the electronic orbital angular momentum vector $\vec{L}$, the electronic spin angular momentum $\vec{S}$ and with each projection on the molecular axis (and quantum number) of respectively, Λ and Σ. The total electronic projection of angular momentum on the nuclear axis is denoted by Ω and is given by: $\Omega = |\Lambda + \Sigma|$. The different molecular electronic states are denoted with ${}^{2|\Sigma|+1}|\Lambda|_\Omega$. The values of Λ=0,1,2,.. are represented with the signs Σ, Π, Δ, respectively. Another feature is the symmetry property of the electronic eigenfunction for the non-degenerate Σ states in diatomics, due to the internuclear axis as symmetry plane and is designated with an added superscript '+' or '-'. If the diatom consists of two identical nuclei then point symmetry exists and the symmetry of the eigenfunction will change or remain with respect to inversion through this point. This property is denoted with a subscript 'u' or 'g', respectively. In order to drive a one-photon allowed (dipole) transition between two states the following selection rules are required [1]:

$$\Delta J = 0, \pm 1\ ;\ \Delta\Lambda = 0, \pm 1\ ;\ \Delta\Omega = 0, \pm 1\ ;\ u \leftrightarrow g\,;\ \Sigma^+ \not\leftrightarrow \Sigma^- \tag{1.2}$$

This section has given some basic rules how a diatomic interacts with a photon. In other words, how the molecule can be driven into a excited state. The next section will deal with how this excited state can decay.

1.2 Fragmentation dynamics of the excited state

After absorption of n photons by the diatom AB in the ground state, the excited molecule AB* can fragment via various decay processes [3]. These fragmentation processes are classified by the fragments produced and are schematically depicted in the following reactions:

$$AB + n\hbar\omega \rightarrow AB^* \rightarrow A + B \qquad \text{photodissociation} \tag{1.3}$$

$$\rightarrow AB^+ + e^- \qquad \text{photoionization} \tag{1.4}$$

$$\rightarrow A^+ + B + e^- \qquad \text{photodissociative ionization} \tag{1.5}$$

These decay processes can be visualized via a so-called *Potential Energy Surface* (PES) in which the potential energy of the molecule AB is plotted as function of the internuclear distance. A PES with the above different kinds of decay mechanisms is presented in Figure 1.1.

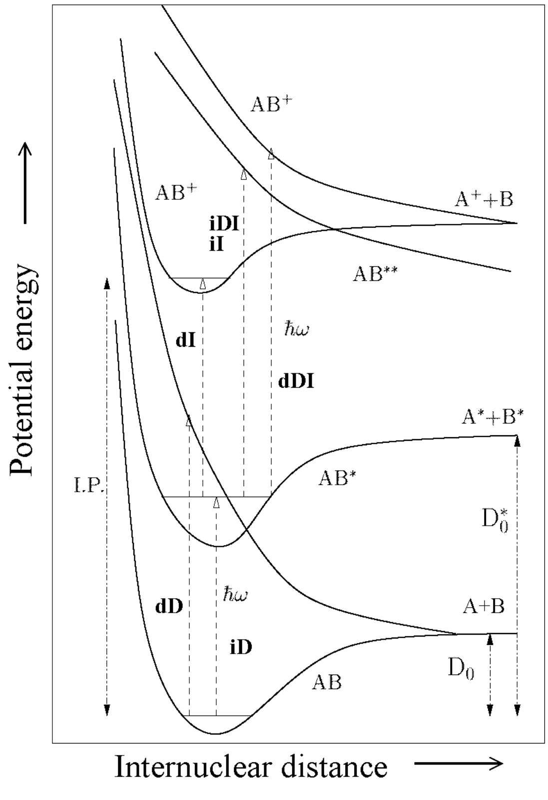

Figure 1.1: *Potential energy surfaces for different kind of decay dynamics. The capitals denote the type of process:* **D***issociation,* **I***onization and* **D***issociative* **I***onization. The small letters represent the* **d***irect or the* **i***ndirect variant.*

The first, and most important process in this thesis, presented in equation (1.3) is named *photodissociation*. In this process the bond between the two atoms A and B is broken and two neutral atoms fly apart. The energy required to break this bond is called *dissociation energy* (D_0). If the intermediate state of AB* is a repulsive one, the molecule will dissociate "immediately" and this process is called *direct* photodissociation. Otherwise the excited state lives longer before AB fragmentates and this process is named *indirect* photodissociation or *predissociation*. In this case the excited state of AB* can couple with a repulsive state which decay via dissociation. A way to view this difference in timescale of the two processes is when the angular distribution is determined by the rotation period of the molecule with respect to the lifetime of the excited state. This effect will be further explained in section 1.3.2. This period is typically 10^{-13} s or 0.1 ps. The neutral product atoms can have different internal energies corresponding to different atomic states. If the atom is so highly excited that the state lies above the ionization energy level of the atom, the atom can ionize subsequently. This process is called post-dissociative ionization and is described in Chapter 7 of this thesis.

The second process depicted in equation (1.4) is called *ionization*. Here the energy of the photon is used to eject an electron out of its orbital leaving the AB$^+$ ion in a certain state having certain values of vibrational and rotational quantum numbers. The minimum energy needed to emit an electron is called Ionization Potential (I.P.) and it typically has a value of $\sim$ 10 eV. Also ionization can be divided in a direct or indirect process. For *direct* ionization the electron leaves the molecule immediately in a fs timescale. In the process of *indirect* ionization or *autoionization* the intermediate state of AB* lies above the I.P. and can therefore decay into this ionization continuum. This autoionization process can also take place on a fs time scale.

The last reaction shown in equation (1.5) is a special process, because it is a combination of reactions (1.3) and (1.4). It is therefore named *dissociative ionization*. Another special feature is that this reaction results in three particles, instead of two in the other mechanisms. This process needs even more photon energy, because now the bond of the ion AB$^+$ needs to be broken. When the photoexcited intermediate state of AB* is a repulsive state in the ion the process will be depicted *direct* dissociative ionization. Otherwise the process is called *indirect* dissociative ionization. In that case the intermediate state is called a *superexcited* state of the superexcited molecule AB**. It should be noted that these superexcited states can also decay via the processes of photodissociation and ionization.

Finally, some other decay mechanisms that do not result in fragmention of the molecule should be mentioned. If the intermediate state of AB* does not decay via the above fragmentation processes, the molecule can undergo a transition to a lower state via emitting a photon. This process is called *fluorescence*. Another decay process for the excited state of AB* is a collision with another molecule and is named *Electronic Energy Transfer* (EET).

1.3 Photodissociation

The two important properties of light, energy and angular momentum, play also a key role in photodissociation dynamics [2]. The process of photodissociation can be viewed as a *half-collision* [4] and is also called an *unimolecular reaction*: $ABC+\hbar\omega \rightarrow AB+C$ or $A+BC$. Photodissociation investigations provide information about the chemical reactions as well. In chemical reaction experiments the products AB and C collide forming an intermediate complex ABC that subsequently decays into scattered products, each with different possible properties. However, in photodissociation one starts with the complex as a molecule ABC and after absorption of a photon, the formed fragments are detected among with their properties.

1.3.1 Kinetics in photodissociation

The major part of the total photon energy $E_{photon} = n\hbar\omega$ for n photons in photodissociation is used to break the bond between the two atoms A and B. This bond breaking requires an amount of energy mentioned earlier as the *dissociation energy* (D_0). The remaining energy is distributed over the internal energy of the atoms E_{int} and the kinetic energy of the fragments E_{kin}.

$$E_{int}(AB) + n\hbar\omega \; = \; E_{int}(A) + E_{int}(B) + E_{kin}(A) + E_{kin}(B) + D_0 \tag{1.6}$$

Another way of defining the dissociation energy is incorporating the internal energy of the ground state atoms into the excited atoms A^* and B^* and the corresponding *excited dissociation limit* D_0^* (also shown in Fig. 1.1):

$$E_{int}(A) + E_{int}(B) + \; D_0 \; = \; D_0^* \tag{1.7}$$

The total kinetic energy U_k delivered in the reaction, also known as *Kinetic Energy Release* (KER), is given by:

$$U_k \; = \; E_{kin}(A) \; + E_{kin}(B) \; = \frac{1}{2}\mathrm{m}_A \,|\, \vec{\mathrm{v}}_A \,|^2 \; + \; \frac{1}{2}\mathrm{m}_B \,|\, \vec{\mathrm{v}}_B \,|^2 \tag{1.8}$$

where m is the mass of the fragment and v the velocity. This equation combined with the following rule of conservation of linear momentum,

$$m_A\vec{\mathrm{v}}_A \; + \; m_B\vec{\mathrm{v}}_B \; = \; 0 \tag{1.9}$$

leads to the partition of the total kinetic energy release over that of the individual particles:

$$E_{kin}(A) \; = \; \frac{m_B}{m_A + m_B}U_k \tag{1.10}$$

The "velocity map imaging" technique determines the velocity of the fragment:

$$|\, \vec{\mathrm{v}}_A \,| = \sqrt{\left(\frac{2m_B}{m_A(m_A + m_B)}\right)U_k} \; = \; \sqrt{\left(\frac{2m_B}{m_A(m_A + m_B)}\right)(n\hbar\omega - D_0^*)} \tag{1.11}$$

For most diatoms the values of D_0^* are known and certainly the masses of the atoms [1]. In the experiment the dissociation photon energy $\hbar\omega$ is fixed and the specific fragments A are state- and mass selectively detected, making it possible to determine the number of photons n and the corresponding formed state of atom B. This enables a full description of the kinetics in the photofragmentation process.

1.3.2 Vector properties in photodissociation

In this section the role of vector correlations in photodissociation dynamics will be discussed The population of the different dissociation limits and the speed of the atoms are so called scalar quantities, but there are also vector properties involved [5]. When an electromagnetic field $\vec{E}$ is defined in the dissociation process by a linearly polarized laser source, several other vectors of interest can be measured in correlation with $\vec{E}$. The vectors of interest due to the vector correlations are:

- $\vec{E}_0$: the polarization vector of the laser light
- $\vec{\mu}$: the transition dipole moment vector of the diatom
- $\vec{v}$: the recoil velocity vector of the fragments
- $\vec{l}$: the rotational angular momentum of the atom

Under normal laboratory conditions the polarization $\vec{E}_0$ of the laser is chosen to be parallel to the z direction of the laboratory frame $\vec{E}_0 = |E_0|\vec{e}_z$. Now some important vector correlations will be discussed in the following subsections.

Angular distributions

This subsection will deal with the important $\vec{E}_0 - \vec{\mu} - \vec{v}$ correlation. Generally, an allowed one photon transition between two electronic states of a diatom is either parallel or perpendicular, depending on the symmetry properties of the initial and the final states. For example, the electronic transitions $\Sigma \leftrightarrow \Sigma$ and $\Pi \leftrightarrow \Pi$ are parallel transitions, but $\Pi \leftrightarrow \Sigma$ is a perpendicular transition. For a parallel transition the transition dipole moment vector $\vec{\mu}$ lies in the direction of the internuclear axis of the diatom and for a perpendicular transition $\vec{\mu}$ lies perpendicular to the internuclear axis. Let θ be the angle between $\vec{\mu}$ and $\vec{E}_0$, then the probability for the absorption of a photon is proportional to $\cos^2\theta$.

Thus, the molecules with their dipole moments parallel to the photon polarization are preferentially excited. Hence the excited molecules are aligned in the laboratory frame after absorption of the photon. If this excited diatom dissociates in a timescale shorter than a rotation period, this alignment of the excited molecule implies an alignment of the recoil velocity $\vec{v}$ since the recoil velocity $\vec{v}$ is directed along the internuclear axis for a diatom. As a result the relation between $\vec{v}$ and $\vec{E}_0$ is described as a function of θ if the molecule dissociates immediately after absorption of a photon. This function is proportional to the angular distribution of the photofragments $I(\theta)$ and is given by $\cos^2\theta$ for a parallel transition and by $\sin^2\theta$ for a perpendicular transition. For a general transition the angular distribution of products can be described with the formula obtained by Zare and Hershbach [6, 7]:

$$I(\theta) \propto 1 + \beta P_2(\cos\theta) \tag{1.12}$$

where $P_2(x) = \frac{1}{2}[3x^2 - 1]$ is the second-order Legendre polynomial. An important quantity is the *anisotropy parameter* β which ranges from -1 for a perpendicular transition to $+2$ for a parallel transition. These limiting cases only appear if the dissociation is significantly faster than the time for a complete rotation of the molecule. Therefore, these extreme values of the anisotropy parameter β mostly appear with direct photodissociation. Also a single electronic state must be excited to obtain the extreme values of the β parameter. A mixture of electronic states leads also to less extreme values of the anisotropy parameter even with fast photodissociation. Measuring the value of β provides therefore information on the type of dissociation. Furthermore, for a direct photodissociation process β gives information about the electronic transition and hence the electronic symmetry of the excited state. The lifetime τ of the excited state has to be shorter than the rotation period T of the diatom in order to get extreme β values. If this is not the case, then this extreme β value is diminished with the following classical mechanics factor [8]:

$$\beta(\tau) = \beta_{max} \cdot \frac{\omega^2\tau^2 + 1}{4\omega^2\tau^2 + 1} \tag{1.13}$$

where β_{max} is 2 or -1 for a parallel and perpendicular transition respectively, and ω is the molecular angular velocity. This implies that the minimum value of β for a parallel transition is 0.5 and for a perpendicular is -0.25 . The value β $\sim$0 then implies a mixture of pure perpendicular and parallel charactere.

The previous discussion dealt with a one-photon angular distribution, but in the general case of a N-photon process this distribution can be described with the following expression [5]:

$$I(\theta) \propto \sum_{n=0}^{n=N} \beta_{2n}^{N} \cdot P_{2n}(\cos\theta) \tag{1.14}$$

with β_{2n}^{N} as anisotropy parameter and $P_{2n}(x)$ as Legendre polynomial given by:

$$\begin{aligned} P_0(x) &= 1 \\ P_2(x) &= \frac{1}{2}[3x^2 - 1] \\ P_4(x) &= \frac{1}{8}[35x^4 - 30x^2 + 3] \\ P_6(x) &= \frac{1}{16}[231x^6 - 315x^4 + 105x^2 - 5] \end{aligned}$$

For a common two-photon process the anisotropy parameters are also known as $\beta = \beta_2^2$ and $\gamma = \beta_4^2$ [9, 10]. Also these anisotropy parameters obtain fixed maximum values for the pure parallel or perpendicular photon transitions. For two sequential pure parallel transitions the anisotropy parameters are β=20/7 and γ=8/7, two perpendicular transitions result in β=-10/7 and γ=3/7, and a parallel-perpendicular combination gives β=5/7 and γ=-12/7. The angular distributions in these three limiting cases are $\cos^4\theta$, $\sin^4\theta$ and $\cos^2\theta\sin^2\theta$, respectively.

Alignment

Another vector correlation can exist between the transition dipole moment vector $\vec{\mu}$, the light polarization vector $\vec{E}_0$ and the angular momentum vector of the photodissociation fragment $\vec{l}$ [2]. Again the polarization vector $\vec{E}_0$ is chosen to be in the z-direction of the laboratory frame. In section 1.3.2 it was shown that $\vec{\mu}$ is preferentially aligned parallel with $\vec{E}_0$ due to the probability relation of absorbing a photon which is proportional with $\cos^2\theta$, where θ is the angle between $\vec{E}_0$ and $\vec{\mu}$. The following correlation involves the direction of the total angular momentum vector $\vec{l}$ (ignoring nuclear spin) along the space fixed polarization vector $\vec{E}_0$ which is pointed in the z-direction. This projection of $\vec{l}$ on the z -axis is described with the *angular quantum number* l obtaining values 0,1,2 ... and with the *magnetic quantum number* m_l having values of $m_l = -l, -l+1, ..., l-1, l$. Suppose a number of fragments with each quantum number $l = 2$ is made, then the magnetic quantum number m_l can be different per fragment. The number of fragments for a certain magnetic quantum number gives the distribution $D(m_l)$ which is a measure of the average angle between $\vec{l}$ and $\vec{E}_0$. Normally, three different types of distributions $D(m_l)$ can exists corresponding to three types of distributions for the direction of $\vec{l}$:

- isotropy
- alignment
- orientation

In figure 1.2 examples for these three types are presented. If $D(m_l)$ is constant then the direction of $\vec{l}$ is isotropic. But if $D(m_l)$ is not constant and symmetrical with respect to $m_l = 0$ then the fragments are aligned and the net angular momentum averaged over all the fragments is zero. This is not the case for orientation. Here also the distribution $D(m_l)$ is not constant but it is also not symmetrical with respect to $m_l = 0$. So in this case all the fragments give an average non-zero net angular momentum. However, under normal conditions orientation does not occur in photodissociation processes. The isotropic distribution is common and sometimes alignment appears. When a diatomic system has to make a parallel transition (see section 1.3.2) in order to photodissociate, then molecules with their dipole moment $\vec{\mu}$ parallel to the polarization $\vec{E}_0$ are preferentially excited. Thus more molecules are excited with their internuclear axis parallel to the polarization vector $\vec{E}_0$. Now if the dissociation is much faster than the rotation of the diatom then the angular momentum $\vec{l}$ of the atom will be pointed perpendicular to the z-direction because the two atoms separate parallel to the polarization $\vec{E}_0$. This results in a distribution which has a maximum near $m_l \approx 0$.

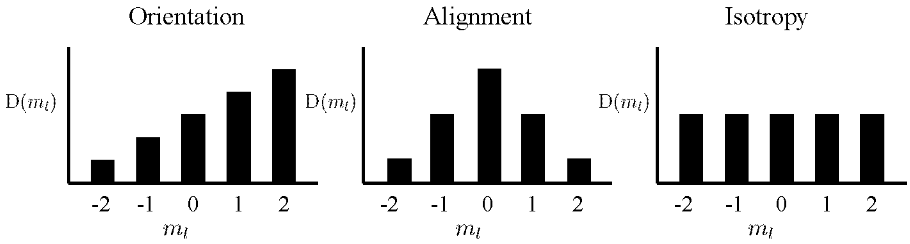

Figure 1.2: *Examples of the different types of distributions for l=2*

A different example of alignment is the proces where a multi-photon formed ion AB^+ is photodissociated. Due to photoselection in subsequent photon transitions the internuclear axis of AB^+ is more or less along $\vec{E}_0$. When the ion is one-photon dissociated is appears that the angular distribution can not be fitted with the one-photon expression (1.12) due to the already induced anisotropy and the higher order angular distribution formula (1.14) is needed. Examples of these effects are seen and described in Chapters 7 and 8.

1.4 Experimental methods

Several experimental techniques are available to characterize the processes involved in photodissociation. Some important observables in the photodissociation decay dynamics of the excited state are: the energy of the excited state, the lifetime τ of the excited state, the velocity of the fragments, the angular distribution of the fragments and the specific state of the formed fragments. All these observables can be measured using different experimental methods. This section will mention briefly some of these experimental techniques in order to get a broader view in experimental approaches of studying photodissociation dynamics of excited states. Also their connection with the used "velocity map imaging" method, treated in the next section, will be clarified when put into a broader perspective.

The *absortion spectroscopy* technique measures the wavelength of absorption in order to obtain the energy of the excited state [11]. The transition lines in the obtained spectrum can be broadened due to the short lifetime of this excited state. This effect can be used to measure the lifetime of the excited state. This behavior can also be examined by "other" types of absorption spectroscopy, like *cavity ring down spectroscopy* and *photoacoustic spectroscopy* [11].

If the excited state lives long enough to emit a photon, this photon can be collected. The fluorescence decay rate gives a measure for the lifetime of the excited state. This technique is named *laser induced fluoresence* (LIF) [11]. The produced fragments can also be probed by LIF, so that the type of fragments can be determined. The velocity of the fragments can be determined using *Doppler spectroscopy*, which detects the fragments via LIF [12]. The LIF detection transition ν is dependent on the velocity v of the fragments along the laser axis due to the Doppler effect ($\nu = \nu_0(1 \pm v/c)$). Measuring the LIF spectrum therefore gives information about the velocity and angular distribution of the formed particles. This technique is more sensitive when the fragments have higher velocities.

Another important type of spectroscopy that should be mentioned is *Multi Photon Ionization* (MPI) or, if the light is resonant with a intermediate state *Resonance Enhanced Multi Photon Ionization* (REMPI) [11]. The latter can also give the energy and lifetime of the excited state. The (RE)MPI technique can also be used to detect the formed fragments. When the ionized fragments drift towards a detector by an electric field the time between creation (determined by the REMPI laser light) and detection, is a measure for the charge to mass ratio and under some conditions it is also a measure for the initial velocity of the fragments. Therefore, this method is also known as *Time Of Flight* (TOF) [13]. With this method also angular information can be acquired by changing the photodissociation laserpolarization as a function of the TOF spectrum.

A superior resolution is achieved by using the *Rydberg tagging* technique [14]. This technique combines the TOF method with a different detection method. In this case the fragment is excited to a high lying, long living Rydberg state, that is ionized and collected at the detector. In this way the neutral fragments do not influence each other and the flight time is longer. This improves the resolution. A major drawback is that the detection is only possible thus far for H atoms and CO molecules, because these particles have high lying *and* long living Rydberg states.

The "velocity map imaging" technique used in this work can be explained as a 2D TOF technique using REMPI to ionize the fragments and a position sensitive detector for collecting the particles. This technique can determine velocity distributions and angular distributions simultaneously and with high resolution as will be explained in the next section.

1.5 The experiment

1.5.1 The velocity map imaging technique

The “velocity map imaging” technique is an dramatic improvement of the former “ion imaging” technique developed by Houston and Chandler [15, 16]. The “velocity map imaging” method, developed by Eppink and Parker [17], improves the kinetic energy resolution of the fragments by a factor 20 and is ideal for studying photodissociation processes [18]. The principles of the technique are shown in Figure 1.3. A molecular beam is pointed along a cylindrical symmetry axis and crossed with the photodissociation and detection laser beams. The polarization of the dissociation light is perpendicular to the symmetry axis and parallel to the detector plane. The polarization direction defines the velocity vector of the fragment in the lab as decribed in section 1.3.2. These neutral fragments are state selectively ionized via Resonance Enhanced Multi Photon Ionization (REMPI) by the detection laser. These ions are repelled by the electrostatic lens into the Time Of Flight (TOF) tube where heavier particles will arrive later at the detector. This effect is used to measure mass selectively by opening the detector at the right time as a certain mass arrives. The ionized fragments form in space at a certain time a sphere that evolves along the symmetry axis and subsequently is crushed onto the detector.

The crushed sphere with radius r onto the detector results in a “raw data image” showing a circle with radius r. From this crushed 2D image the original 3D distribution can be reconstructed via the Abel inversion algorithm. A slice through this 3D distribution is presented in 2D as a “Abel inverted image”. The radius of the ring in the image is a direct measure of the velocity of the fragments and this is shown in the next lines. Let L be the length between the interaction zone and the detector and let Δt be the time for the ions to travel this distance. The velocity along the symmetry axis and perpendicular to the detector (and ignoring the velocities of the parent molecule before the photodissociation) is given by: $\mathrm{v}_{\perp} = L/\Delta t$. The velocity of the fragments parallel to the detector is then given by: $\mathrm{v}_{||} = N \cdot r/\Delta t$, where N is a factor dependent on the used electrostatic lens (in this case N=1.30). This means that the radius of an image is a direct measure of the velocity of the fragment and together with formula (1.11) the ring can be ascribed to a certain photofragmentation process. The laser beams traverse the molecular beam at right angles making a line source of photodissociation fragments instead of a point source. In other words, a set of ion spheres along the x-axis is formed. In the former ion imaging technique this would result in different radii on the image. When using the electrostatic lens in velocity map imaging this process is diminished by deblurring resulting in a sharper image and better correspondence of r and $\mathrm{v}_{||}$ [17].

1.5.2 The setup

The setup consists of three major parts: the velocity map imaging setup, the detection laser and the dissociation laser and is presented in Figure 1.4. The *velocity map imaging setup* [17] is a vacuum system which is differentially pumped. The interaction region, existing of the nozzle, skimmer, electrostatic lenses, molecular beam and the two laser beams, is pumped by a 5200 ls^{-1} oil diffusion pump (*Balzers DIF 320*). Furthermore, a large liquid nitrogen trap is applied to further lower the pressure to a value of $8 \cdot 10^{-8}$ Torr. The detection region, being the TOF tube and the double Micro Channel Plates (MCP's), is pumped by a turbo pump (*Balzers TPH 240*), yielding a typical pressure of $1 \cdot 10^{-8}$ Torr. The nozzle is a pulsed valve (*General Valve*) with a 0.8 mm hole, which produces an expansion cooled molecular beam. This beam consists of a 10 – 20% mixture of the desired molecule with helium at a backing pressure of 2 bar. Furthermore, this beam is skimmed with a 1 mm skimmer mounted 40 mm downstream. This molecular beam crosses the laser beam between the repeller plate and the extractor plate of the electrostatic lens. The dissociation laser dissociates the diatoms and the detection laser ionizes the atoms via a REMPI process. These ions are extracted towards the detector using a electric field made by a electrostatic lens. The electrostatic lens consists of three plates; repeller, extractor and ground of respectively 4000 Volt, 2840 Volt and 0 Volt. The plates are separated by 15 mm and are 70 mm in diameter. The repeller electrode has a hole of 2 mm and the other two have each a hole of 20 mm. The valve, skimmer and electrostatic lens are mounted on a beam aligner to be able to adjust focusing in the middle of the detector. The ions first fly through a 36 cm TOF (Time

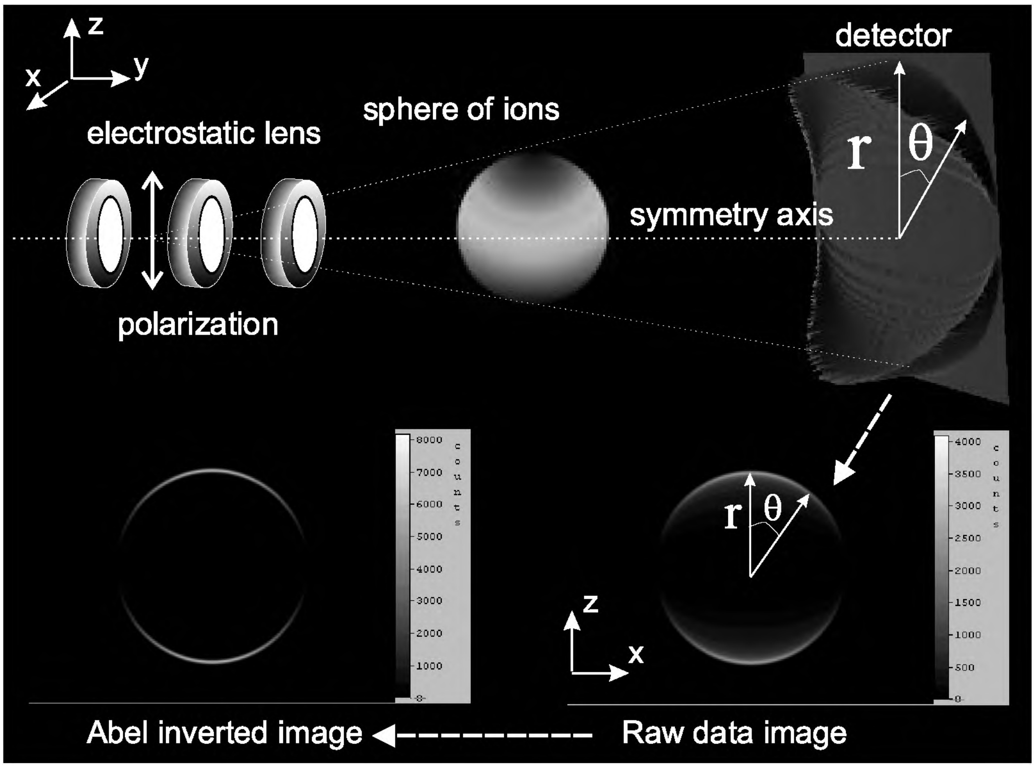

Figure 1.3: *Overview of the velocity map imaging technique. A sphere of ions created by laser light is crushed onto a position sensitive detector giving the intensity of ions per position. The two-dimensional represention is called an image, of which the intensity is presented by a grey scale shown on the right side of each image. The radius r of the ring is proportional with the velocity of the fragments. The intensity on a certain radius as function of θ results in the angular distribution. This information is obtained after an Abel inversion of the raw data image. This figure depicts a pure one-photon parallel photodissociation transition.*

Of Flight) tube before hitting the detector. The detector consist of two 40 mm diameter chevron Micro Channel Plates (MCP's) assembly and a P-20 phosphor screen (*Galileo 3040- FM*). Mass selective selection is achieved by time gating the front MCP with a timed high voltage pulse made by a High Voltage switch (*La Vision*). A Peltier cooled CCD camera (*La Vision*) of 384 × 286 pixels with a f = 25 mm objective (*Schneider*) records the 2D ion image of the phosphor screen. This image is stored in a PC where further data analysis is performed.

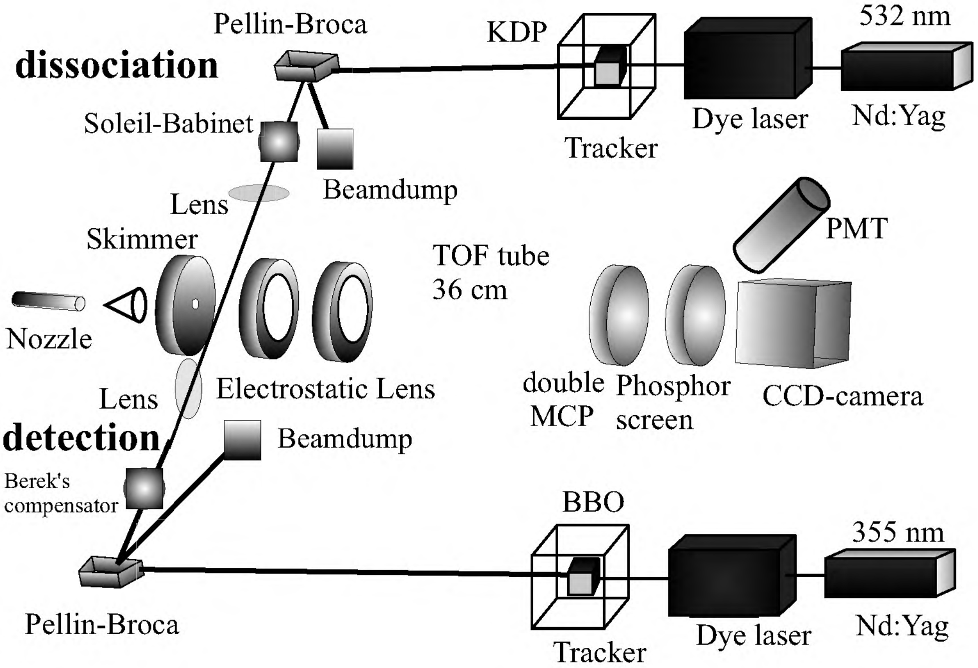

Figure 1.4: *Overview of the setup showing the velocity map imaging setup, the dissociation light source and the detection light source*

The *detection laser* consists of a Nd:Yag pumped dye laser and a frequency doubling unit. The dye laser (*Spectra Physics PDL-2*) is pumped with 355 nm radiation of a Nd:Yag (*Spectra Physics DCR-2a*). The fundamental light is frequency doubled in a BBO crystal that is also fixed in a tracker device to optimize the doubling process. After dissociation the fragments fly apart Doppler shifting the REMPI transition, so the probe laser has to scan over this Doppler width followed by the autotrack unit in order to give equal detection efficiency to all fragments. The fundamental wavelength and the frequency doubled one are dispersed by a Pellin-Broca prism so that the fundamental wavelength can be blocked. Furthermore, the doubled laser beam is flipped to vertical polarization using a Berek's compensator, which is a variable wave plate set as a $\lambda/2$ plate. This light, 0.5 mJ/5ns, is then focussed into the ion imaging apparatus with a 20 cm lens. The detection is fired 20 ns after the dissociation laser to avoid multiple photon excitation by the detection laser. The light of the detection laser ionizes atoms in a certain quantum state via a 2+1 Resonance Enhanced Multi Photon Ionization (REMPI) process. A specific atom state A^* is excited resonantly by two photons to a higher state A^{**} where a third subsequent photon ionizes that atom.

The *dissociation laser* consists also of a Nd:Yag pumped dye laser and a frequency doubling unit. The Nd:Yag laser (*Spectra Physics GCR-11*) pumps with 532 nm a dye laser (*Spectra Physics PDL-2*) in order to get a tunable light source. The output is frequency doubled in a KDP crystal that is mounted on another autotracker unit which adjusts the crystal angle for changes in frequency to get maximum output power. The frequency doubled light is separated from the fundamental light by a Pellin-Broca prism made vertically polarized by a Soleil-Babinet compensator and via 20 cm lens focussed onto the molecular beam. This dissociation source is used in Chapters 3 and 4.

A different dissociation source with the same setup is used in Chapters 5, 6 and 9. In that case the laser source is a line narrowed ($\Delta\nu \sim 0.5 cm^{-1}$) tunable ArF excimer laser delivering 193.3 nm light with ~25 mJ per 15 ns pulse. The laser beam passes some Brewster mirrors and is directed to the molecular beam by a series of dichroic mirrors resulting in a vertical polarization higher than 99% .

In the Chapters 7 and 8 a similar velocity map imaging setup in the FORTH institute in Heraklion, Crete, Greece is used with the use of a special laser setup. The laser is a short pulse KrF laser system that produces 248 nm photons with 500 fs or 5 ps pulsewidths.

1.6 Outline

This thesis consists of chapters dealing with the different types of fragmentation processes mentioned in Section 1.2 which the diatomic molecules undergo after being excited by various kinds of light. First, in **Chapter 2** the direct photodissociation of Cl_2 is investigated in the region between 310 nm and 470 nm. Also the alignment of produced photofragments is observed. In **Chapter 3** the sequential two-photon predissociation of NO via the $A^2\Sigma^+$ electronic state is treated, using one 226 nm photon and one 339 nm photon. The use of this photodissociation process as photolysis source in reaction dynamics is discussed. The next chapter (**Chapter 4**) presents results on the predissociation dynamics of Rydberg states of NO excited by a two-photon (2 times 275 nm) process. The β parameter and branching ratios for the different available dissociation limits are measured. **Chapter 5** presents results on (1+1) REMPI with 193 nm of $^{13}C^{16}O$ via the $a^3\Pi(v=2) \leftarrow X^1\Sigma^+(v=0)$ transition, where at the two-photon level the molecule (pre)dissociates. **Chapter 6** investigates some transitions in O_2 in the atmospherically relevant Schumann-Runge band using a tunable 193 nm source. Here the predissociation of the $B^3\Sigma_u^-(v=4)$ state in O_2 and the subsequent photophysics is investigated. On the two-photon level high Rydberg states autoionize and contribute to the ionization signal that is monitored by photodissociation of the formed O_2^+ ion. **Chapter 7** and **Chapter 8** describe results on the multiphoton dynamics of 0.5 ps and 5 ps pulses of 248 nm in O_2 and H_2, respectively. Because no detection laser is used the main process seen is (auto)ionization. Ions are formed in different vibrational states and subsequent photons photodissociate these states. For H_2 also dissociative ionization is observed. In O_2 another unusual process is seen: post-dissociative ionization. In **Chapter 9** the direct dissociative ionization of H_2 is described, where experimental results are compared with calculations. Also (auto)ionization is observed. The hydrogen molecule was excited via a (2+1) REMPI process via the E,F $^1\Sigma_g^+(v=6,J=0)$ state.

References

[1] G. Herzberg, *Molecular Spectra and Molecular Structure, I. Spectra of Diatomic molecules*, (Van Nostrand Reinhold Co, New York, 1950).
[2] R. Schinke, *Photodissociation Dynamics: Spectroscopy and Fragmentation of small polyatomic molecules*, (Cambridge University Press, Cambridge 1993).
[3] H. Lefebvre-Brion and R.W. Field, *Perturbations in the Spectra of Diatomic Molecules*, (Academic Press, Orlando, 1986).
[4] R.D. Levine and R.B. Bernstein, *Molecular reaction dynamics and chemical reactivity*, (Oxford University Press, Oxford, 1987).
[5] R.N. Zare, *Angular Momentum* (Wiley, New York 1988).
[6] R.N. Zare and D.R. Hershbach, *Proc. IEEE* **51**, 173 (1963).
[7] R.N. Zare, Mol. Photochem. **4**, 1-37 (1972).
[8] C. Jonah, J. Chem. Phys. **55**, 1915 (1971).
[9] K. Chen and E.S. Yeung, J. Chem. Phys. **72**, 4723 (1980).
[10] R.K. Sanders and K.R. Wilson, J. Chem. Phys. **63**, 4242 (1975).
[11] W. Demtröder, *Laser spectroscopy, Basic concepts and intrumentation*, (Springer-Verlag, Berlin, 1988).
[12] R. Schmiedl, H. Dugan, W. Meier and K.H. Welge, Z. Phys. A **304**, 137 (1982).
[13] M. Mons and I. Dimicoli, J. Chem. Phys. **80**, 4037 (1989).
[14] M.N.R. Ashfold, D.H. Mordaunt and S.H.S. Wilson, *Advances in Photochemistry* **21**, 217 (Wiley, New York, 1994).
[15] D.W. Chandler and P.L. Houston. J. Chem. Phys. **87**, 1445 (1987).
[16] A.J.R. Heck and D.W. Chandler, Annu. Rev. Phys. Chem. **46**, 335 (1995).
[17] A.T.J.B Eppink and D.H. Parker, Rev. Sci. Instrum. **68**, 3477 (1998).
[18] D.W. Chandler and D.H. Parker, Adv. Photochem. **25**, 56 (1999).

Chapter 2

Spin-orbit branching ratios for the Cl-atom photofragments following the excitation of Cl_2 from 310 to 470 nm

Abstract

Velocity distributions for the Cl($^2P_{3/2}$) and Cl($^2P_{1/2}$) photofragments produced by the photolysis of Cl_2 in the region between 310 and 470 nm, are measured using photofragment velocity mapping. Our results indicate that at short wavelengths the absorption spectrum is dominated by the $1_u(^1\Pi_u)$ excited electronic state which produces two ground state chlorine atoms. The $0_u^+(B^3\Pi_u)$ state which produces a spin-orbit excited and a ground state chlorine atom becomes significant at 350 nm and dominates the spectrum beyond 400 nm. Analysis of the photofragment angular distributions indicate that the Cl($^2P_{3/2}$) photofragments are aligned and the magnitude of the alignment is quantitatively determined. Non-adiabatic curve crossing between the $1_u(^1\Pi_u)$ and the $0_u^+(B^3\Pi_u)$ electronic states is observed and quantified below 370 nm. The measured non-adiabatic transition probability is modeled using the Landau-Zener formula and the position of the curve crossing is estimated at $\sim$3 eV above the zero-point of ground electronic state of Cl_2.

2.1 Introduction

The ultraviolet absorption spectrum of molecular chlorine between 250 and 450 nm is continuous with its maximum occurring at ~330 nm. The spectrum has been attributed to transitions between the Cl_2 0_g^+ $(X^1\Sigma_g)$ ground electronic state and the purely repulsive $1_u(^1\Pi_u)$ and $0_u^+(B^3\Pi_u)$ excited electronic states [1, 2, 3, 4, 5]. The photolysis of Cl_2 is a common source of chlorine atom reactants in modern Doppler-based chemical reaction studies [6] that are relevant to atmospheric chemistry. As in all halogen atoms, spin-orbit coupling causes the atomic ^2P_J ground state to split into a pair of states with J=1.5 and J=0.5. These $Cl(^2P_{3/2})$ and $Cl(^2P_{1/2})$ states will be denoted by Cl and Cl* respectively in the remaining manuscript. In the case of atomic chlorine, Cl and Cl* are separated by 881cm $^{-1}$, a splitting which although substantially smaller than that of Br (3685 cm^{-1}) and I (7603 cm^{-1}), could lead to variations in the chemical reactivity between ground and spin-orbit excited Cl atoms. It is thus of interest to decompose the absorption spectrum of Cl_2 in order to identify the wavelength dependence of the yields and angular distributions of Cl and Cl* atoms.

In our previous reports concerning the photolysis of Cl_2 our results indicated that the Cl*/Cl branching ratio at 360 nm is ~8% while at 308 nm this ratio drops to lower than 0.01%. The $1_u(^1\Pi_u)$ electronic state correlates adiabatically with Cl+Cl, while the $0_u^+(B^3\Pi_u)$ electronic state correlates with Cl*+Cl. At a fixed dissociation wavelength the latter channel will have less translational energy than the former one since Cl* contains internal energy. Consequently, the velocity distribution of the Cl photofragments should be bimodal, while the Cl* distribution should show a single peak. Unfortunately, the energy resolution of our spectrometer in the initial experiments was relatively poor ($\Delta E/E$=20%), and the two expected peaks in the Cl channel were not observed directly. However, the angular distributions $I(\theta)$ of the Cl photofragments from the two possible channels are expected to be completely orthogonal as the $1_u \leftarrow 0_g^+(X^1\Sigma_g)$ is a perpendicular transition where as the $0_u^+ \leftarrow 0_g^+(X^1\Sigma_g)$ constitutes a parallel transition [7, 8]. By fitting the experimentally measured differential cross section $I(\theta)$ to a functional form $A\cos^2\theta + \sin^2\theta$ we were able to extract the Cl*/Cl branching ratio. Implementing the velocity mapping method developed by Eppink and Parker [9] we have now been able to improve the resolution of our spectrometer thus resolving the contribution of each channel to the Cl translational energy distribution, which ultimately leads to a more accurate determination of the Cl*/Cl branching ratio. In this report we present our results concerning the velocity distributions of the Cl and Cl* photofragments following the photolysis of Cl_2 in the region between 310 and 470 nm, a wavelength regime that covers the major part of the Cl_2 absorption spectrum in the first continuum.

2.2 Experimental

The apparatus has been described in detail elsewhere [10]. Briefly, a gas sample containing 5% Cl_2 in He, is expanded into the source vacuum chamber via a home-built piezoelectrically-actuated pulsed-molecular beam operating at 20 Hz. After passing through a skimmer and collimator, the molecular beam is intersected at right angles by two counter propagating laser beams. The photolysis laser beam is generated by an excimer-pumped (Lambda Physik LPX 300, operating with XeCl) pulsed-dye laser (Lambda Physik FL3000, operating with DMQ, QUI, PBBO, POPOP, Coumarin 120, Coumarin 102). The probe laser beam is generated by frequency doubling the output of an excimer-pumped (Lumonics HyperX400, operating with XeCl) pulsed-dye laser (ELTO LT1233, operating with Coumarin 102), using a BBO crystal. The Cl atom photofragments are ionized using (2+1) REMPI and the ions produced are accelerated towards a home-built ion-imaging detector. Ions of different mass separate in their time-of-flight during their field-free trajectory on route to the detector. The length of this field free drift region is increased to 130 cm from our usual 45 cm for this experiment in order to maximize the size of the image on our detector. The detector gain is pulsed on at the proper arrival time for mass-selection. A significant modification to our detector is the replacement of the Microsphere plates (ElMul MSP-50, resolution $\sim$0.5 mm) with Microchannel plates (resolution $\sim 40 \mu$m). Images appearing on the detector anode are recorded using a CCD video camera. The adaptation of the *velocity mapping* technique mentioned above as a major modification in our experimental apparatus has improved our energy resolution from 20% to better than 5%. Cl* images for dissociation wavelengths between 310 and 350 nm are measured using the velocity mapping apparatus at the University of Nijmegen [9].

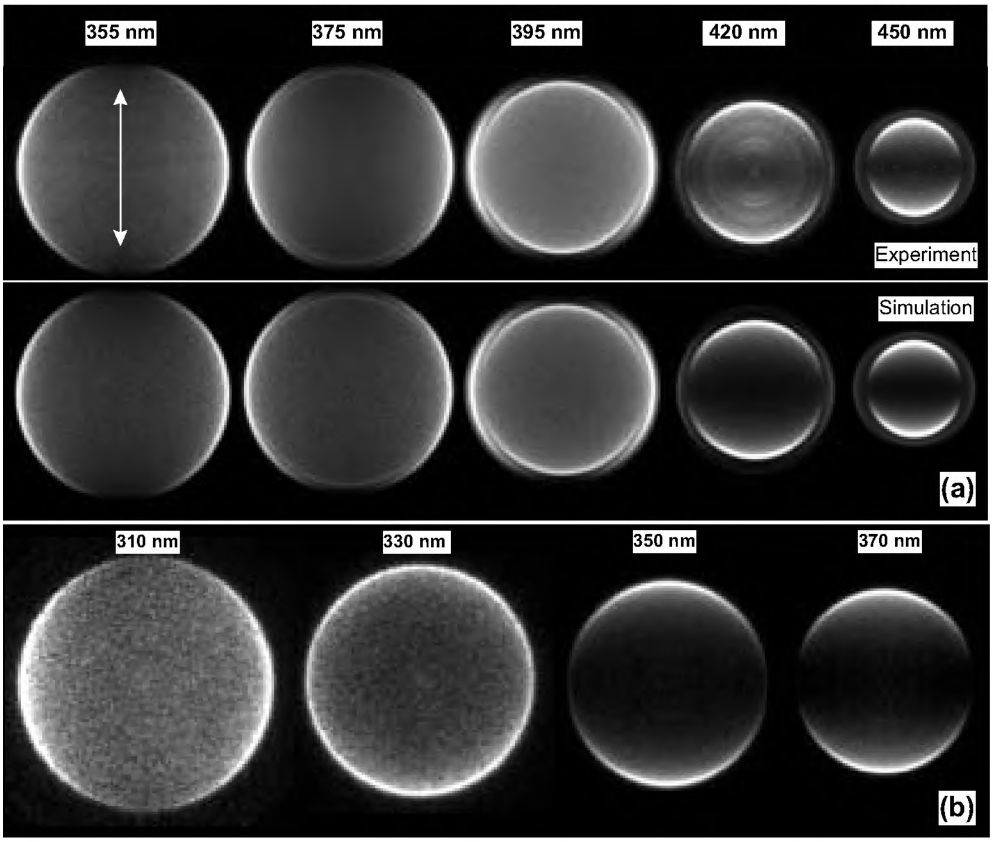

Figure 2.1: *(a) Photofragment images and Monte Carlo simulations of the Cl photofragment produced from the photodissociation of Cl_2 at various wavelengths. (b) Photofragment images of the Cl^* photofragment produced from the photodissociation of Cl_2 at various wavelengths. The vertical arrow ($\updownarrow$) indicates the polarization direction of the photolysis laser.*

2.3 Results

The Cl* and Cl photofragments are ionized using two-photon resonant transitions $4p(^4D_{5/2}) \leftarrow 3p^5(^2P_{1/2})$ at 240.19 nm and the $4p(^4P_{3/2}) \leftarrow 3p^5(^2P_{3/2})$ at 240.53 nm [11, 12, 13]. Photofragments images of ^{35}Cl* and ^{35}Cl are shown in Fig.'s 2.1(a) and 2.1(b), respectively. These are 2D projections of the 3D velocity distributions with the polarization direction of the photolysis laser maintained parallel to the detector's surface. In this geometry reconstruction of the cylindrically symmetric 3D distribution from its 2D projection can be achieved through an inverse Abel transform [14, 15]. These images shown in Fig. 2.1 have been averaged with respect to the laser polarization direction and with respect to an axis perpendicular to this direction (quadrant averaging). In addition to the Abel inversion method, a forward convolution of our data is performed using a Monte Carlo routine to simulate the data and the results are shown in the lower part of Fig. 2.1(a). This alternative method is especially useful for analyzing images where the Cl*/Cl branching ratio is less than 10%. Both methods yield similar results.

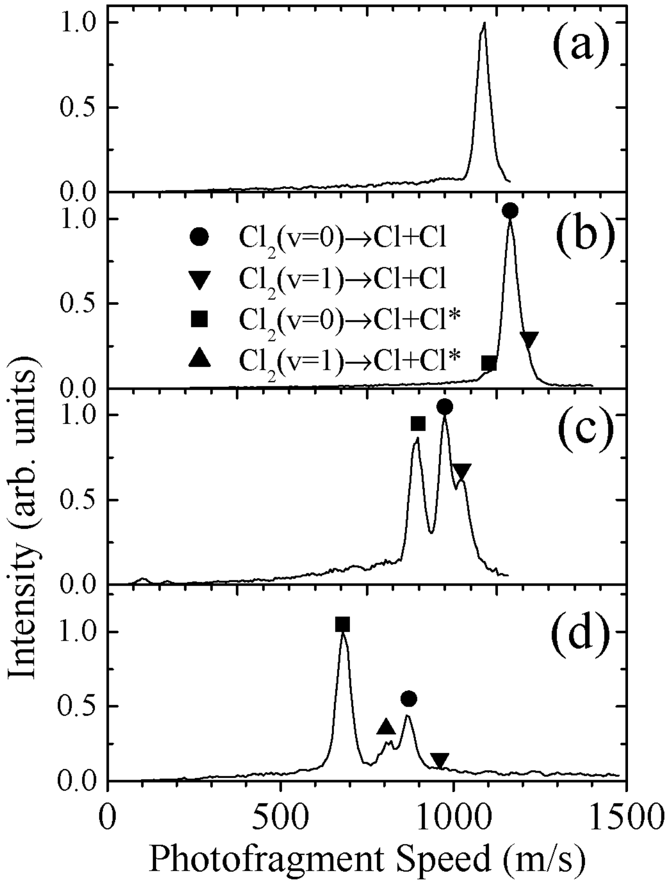

Figure 2.2: *Chlorine atom speed distributions for various photolysis wavelengths, determined from the inverse Abel transforms of the images.*

Sample speed and angular distributions for the Cl and Cl* photofragments determined from reconstructed [16, 17, 18] images are shown in Fig.'s 2.2 and 2.3. The Cl* speed distribution consists of a single peak while the speed distribution for Cl is at least bimodal and reveals additional peaks at certain wavelengths (e.g., 420 nm). The relative intensities of the peaks in the Cl speed distribution depend strongly on the photodissociation wavelength. The angular distribution for the Cl* channel is invariant for wavelengths greater than 370 nm and starts to change for photodissociation wavelengths shorter than 370 nm.

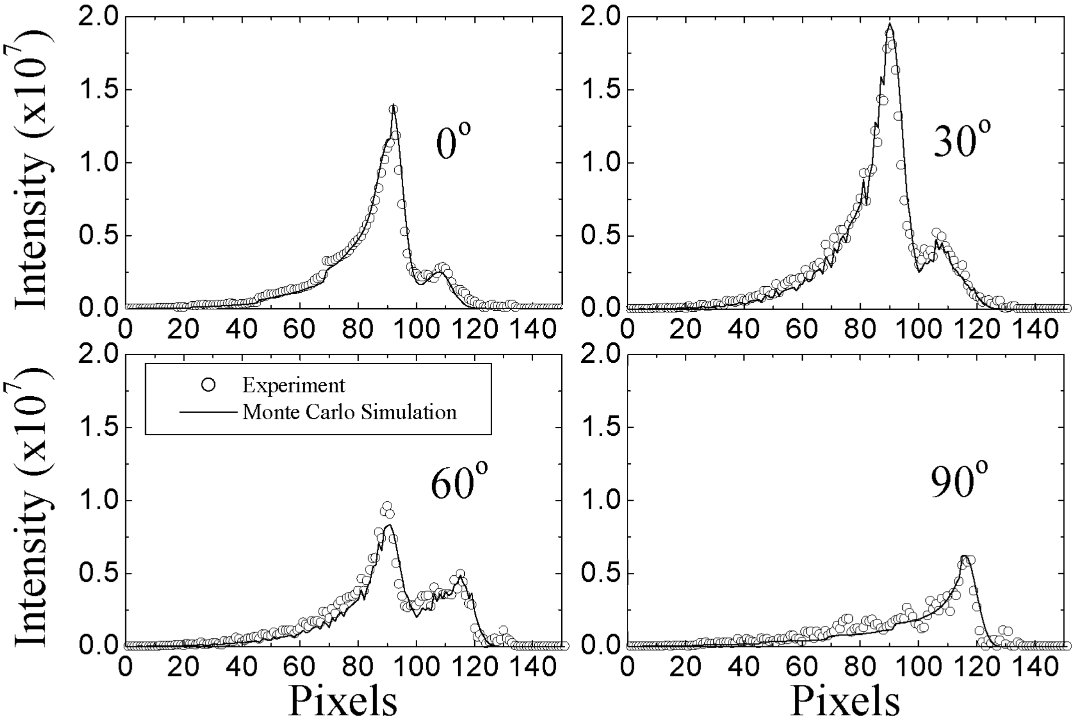

Figure 2.3: *Intensity distributions along 5° sector cuts of the data and simulated images at angles 0°, 30°, 60° and 90°, at a photodissociation wavelength of 450 nm.*

2.4 Discussion

2.4.1 Cl*/Cl branching ratio

The Cl photofragment images show multiple rings, whose relative intensities vary as a function of photolysis wavelength. Conservation of energy dictates that

$$E_T = \frac{m(Cl)}{m(Cl_2)}\left[E_{ph} - \Delta E_{S.O.} - D_o + E_v(Cl_2) + E_{rot}(Cl_2)\right] \tag{2.1}$$

where E_T is the translational energy of the photofragment, $E_{S.O.}=0.109$ eV is the spin orbit splitting, $D_o=2.474$ eV is the dissociation energy of $Cl_2(X^1\Sigma_g)$, and $E_v(Cl_2)$ and $E_{rot}(Cl_2)$ are the vibrational $\Delta E_{vib} \approx$ 600 cm^{-1}) and rotational excitation of the Cl_2 parent molecule. The two dominant rings in the speed distribution correspond to the two energetically allowed channels i.e.,

$$\begin{aligned} Cl_2(v=0) + h\nu &\rightarrow Cl + Cl \qquad \text{(I)} \\ Cl_2(v=0) + h\nu &\rightarrow Cl + Cl^* \qquad \text{(II)} \end{aligned}$$

with the inner ring corresponding to channel II as it produces slower Cl photofragments. In addition, the angular distributions of the photofragments for each ring are drastically different, supporting our assumption that channel I arises from a perpendicular transition while channel II results from a parallel excitation. At long wavelengths (e.g., 395 nm and 450 nm), the additional peaks in the spectrum which appear at the high kinetic energy side of the main peaks, correspond to “hot band“ dissociation of Cl_2(v=1).

Interestingly, at certain photodissociation wavelengths several additional ‘satellite’ peaks (extra rings on the image e.g., 420 nm) appear in the speed distribution at unexpected speeds. In order to elucidate the nature of these peaks we set the probe laser off-resonance and scanned the dissociation laser. In doing so we are able to map out a series of (1+1’) excitations of the Cl_2 parent molecules to the 0_g^-(v=25-30) excited electronic states. Such studies have been reported by Al-Kahali *et al.* [19] at lower excitation energies. The detected Cl^+ atoms are products of several more photoabsorption steps from the excited electronic state. Details on the exact nature (spectroscopy and dynamics) of these excitations will be presented in a forthcoming publication [20]. These accidental resonances are only present when probe and photolysis laser are temporally overlapped. A zero time-delay between the pump and probe lasers is important in the present experiment since the goal is to determine the branching Cl*/Cl ratio without allowing any escape of photofragments from the interaction volume. The contributions of the ‘satellite’ peaks to the images is readily distinguished from those of channels I and II, and hence their presence does not hinder our analysis.

For $\lambda > 370$ nm, the peaks for channels I and II are clearly resolved in the speed distribution spectra and from their relative areas we determine the propensity of each channel. However, as the excitation wavelength decreases, channel II remains visually distinguishable in the image, but the small branching ratio causes its corresponding speed distribution peak to get buried under the low energy side of the channel I peak. This hinders the extraction of accurate branching ratios from the speed distribution alone. In this case, we model our data using a forward convolution method, i.e., assume an angular and energy distribution (details in the next section) and generate an image using the Monte Carlo method. To examine the goodness of the simulation we compare the intensity distribution along 5^o sector cuts of the data and simulated images at angles 0^o, 30^o, 60^o and 90^o(Fig. 2.3(a)). In addition to the branching ratio between channels we are able to also determine the angular distribution per channel and the results are presented in Table 2.1.

Assuming gaussian shaped cross sections $\varepsilon(0_u^+)$ and $\varepsilon(1_u)$ we model the experimental branching ratios using the relationship

$$\frac{Cl^*}{Cl} = \frac{\varepsilon\left(0_u^+\right)}{2\varepsilon\left(1_u\right) + \varepsilon\left(0_u^+\right)} \tag{2.2}$$

Table 2.1: *Values for the anisotropy parameters β_2 and β_4 determined from the Monte Carlo simulation of the Cl images and assuming an angular distribution described by Eq. (2.7) (see text) for Cl or for Cl* channel and for different wavelengths λ.*

λ (nm)	β_2(Cl)†	β_4(Cl)†	β_2(Cl*)‡	β_4(Cl*)†	Cl*/Cl
350	-0.98	0.00			0.003±0.01
355	-0.98	0.00			0.006±0.01
360	-0.98	0.00	1.60	-0.21	0.010±0.01
365	-1.0	0.00	1.65	-0.22	0.020±0.01
370	-0.98	0.00	1.72	-0.23	0.048±0.01
375	-1.0	0.00	1.82	-0.24	0.056±0.01
380	-1.05	0.00	1.82	-0.24	0.091±0.02
385	-1.0	0.00	1.82	-0.24	0.115±0.02
390	-1.0	0.00	1.82	-0.24	0.213±0.02
395	-1.05	0.00	1.82	-0.24	0.281±0.02
400	-1.0	0.00	1.82	-0.24	0.429±0.02
420	-1.0	0.00	1.82	-0.24	0.648±0.03
430					0.725±0.03
440	-1.0	0.00			0.754±0.03
450	-1.0	0.00	1.82	-0.24	0.706±0.03
460					0.675±0.03
465					0.690±0.03
470					0.685±0.03

†error= ±0.05, ‡error= ±0.10

Table 2.2: *Parameters for the Gaussians used to model the partial absorption cross sections $\varepsilon(0_u^+)$ and $\varepsilon(1_u)$.*

$\frac{A}{w\sqrt{\frac{\pi}{2}}} exp\left(-2\left(\frac{\tilde{\nu}-\tilde{\nu}_0}{w}\right)^2\right)$	$\tilde{\nu}_0$ (cm^{-1})	w(cm^{-1})	A(cm^{-1})
$\varepsilon(1_u)$	30200±50	4115±80	5072±100
$\varepsilon(0_u^+)$	24100±150	3284±270	294±20

and the fit is shown in Fig. 2.4(a). The characteristics of the Gaussian curves that best model our data are listed in Table 2.2 and plots of the $\varepsilon(0_u^+)$ and $\varepsilon(1_u)$ are shown in Fig. 2.4(b).

$$\varepsilon_{tot} = \varepsilon(0_u^+) + \varepsilon(1_u) \tag{2.3}$$

As Figure 2.4(b) suggests that our experimentally determined cross section is in fair agreement with the total absolute cross section determined from absorption spectroscopy [21, 22, 23]. This two-state decomposition of the lowest absorption continuum of Cl_2 is not corrected for the effects of curve-crossing, which slightly enhances $\varepsilon(0_u^+)$. As we show in the next section, curve crossing, while readily apparent in the angular distributions, is a minor effect in the overall photoabsorption process.

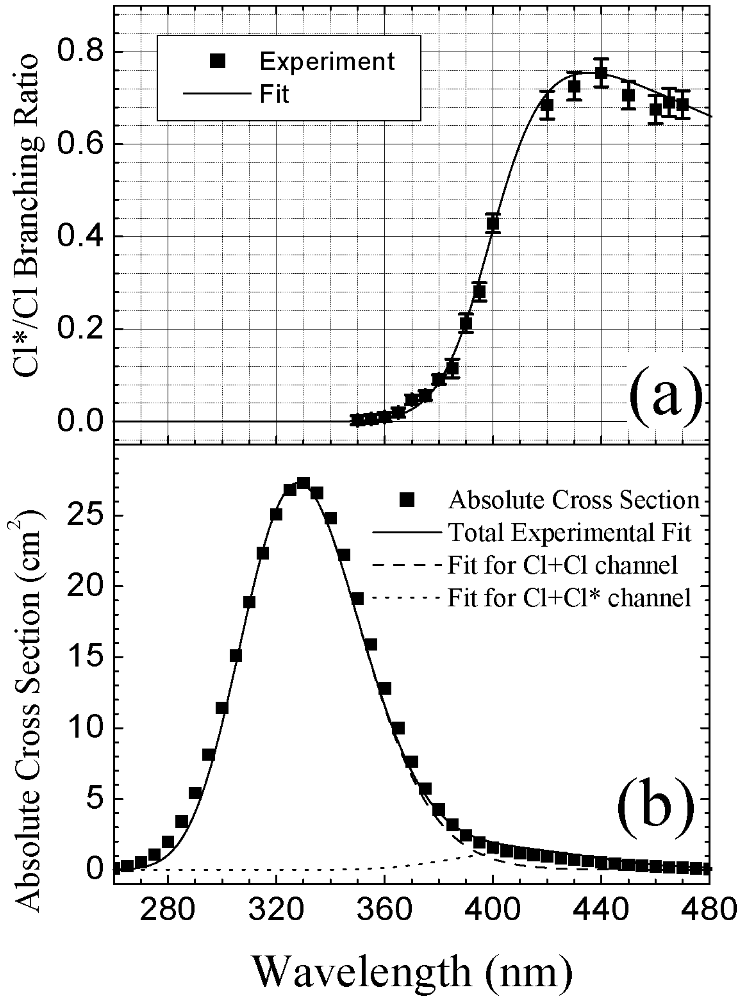

Figure 2.4: *(a) Experimental Cl*/Cl branching ratios and model fit. (b) Partial and total absorption cross sections for* Cl_2*. The absolute absorption cross sections is taken from ref. [21].*

2.4.2 Angular distributions and nonadiabatic curve crossings

Inspection of image 2.1(a) indicates that most of the Cl* photofragments are ejected along the polarization direction of the photolysis laser. We model the experimental angular distributions, an example of which is presented in Fig. 2.5(a) using the function

$$I(\theta) \propto 1 + \beta P_2(\cos(\theta) \qquad (2.4)$$

and the resulting values of β are shown in Fig. 2.5(b) and are listed in Table 2.3. For $\lambda > 370$ nm (Cl*)=2.00$\pm$0.08, it then decreases with λ, and finally approaches a limiting value of approximately -0.9 at 310 nm (Fig. 2.5(a)). The value β(Cl*)=2 is consistent with the expectations of a prompt dissociation following excitation through a parallel transition $0_u^+ \leftarrow 0_g^+$ ($X^1\Sigma_g$). The deviation from the ideal β=2 value can be attributed to nonadiabatic curve crossing between the $1_u(^1\Pi_u)$ and the $0_u^+(B^3\Pi_u)$ electronic states. In this case a sufficient amount of the Cl atoms produced by direct excitation to the 1_u state (perpendicular transition, $\Delta\Omega$=+1) is converted to Cl* by the nonadiabatic coupling, thus adding sufficient *perpendicular* character to the otherwise *parallel* type Cl* angular distribution.

Assuming that $I(\theta) \propto AI_\perp(\theta) + I_\parallel(\theta)$, where $I_\perp(\theta) = (4/3\pi)(1 - P_2(\cos\theta)) = 2\sin^2\theta/\pi$, $I_\parallel(\theta) = (2/3\pi)(1 + 2P_2(\cos\theta))$=$2\cos^2\theta/\pi$ are normalized angular distributions for $\beta = -1$ and 2 respectively, and using the effective beta parameter β_{eff} determined by fitting the Cl* distributions with functional form of Eq. (2.4), we find that

$$A = \frac{2 - \beta_{eff}}{2\left(1 + \beta_{eff}\right)} \tag{2.5}$$

The curve crossing probability P_{cc}, for Cl to be converted into a Cl* is given by the relationship

$$P_{cc} = \frac{A\varepsilon\left(0_u^+\right)}{2\varepsilon\left(1_u\right) + A\varepsilon\left(0_u^+\right)} \tag{2.6}$$

and the results are shown in Fig. 2.5(c). Clearly P_{cc} decreases with increasing photofragment velocity, in other words, the faster the Cl fragments, the more difficult it is to have a nonadiabatic transition, i.e., the fragment remains on the same *adiabatic* potential energy surface. This picture is consistent with the theory of Landau-Zener [24, 25] according to which the *nonadiabatic* curve crossing probability P_{cc} is proportional to $1 - exp(-c/\mathrm{v})$ where c is a constant related to the coupling strength between the states and the slope of the potential curves and v is the photofragment velocity at the curve crossing. Conservation of energy dictates that the speed v is related to the position of the curve crossing E_{cc} and the Cl* photofragment speed v_A (both quantities with respect to the Cl*+Cl asymptote) as follows

$$\frac{1}{2}m\mathrm{v}^2 = \frac{1}{2}m\mathrm{v}_A^2 - E_{cc} \tag{2.7}$$

Performing a Landau-Zener type fit our data using the function

$$P_{cc} = 1 - exp\left(-\frac{c}{\sqrt{\mathrm{v}_A^2 - 2E_{cc}/m}}\right) \tag{2.8}$$

we find 0.45 eV$\leq E_{cc} \leq$0.50 eV, with given $\Delta E_{S.O.}$=0.109 eV and D_o=2.474 eV predicts that the curve crossing is located at ~3eV above the zero-point energy of the ground electronic state of Cl_2. As is evident from Fig. 2.5(c), the Landau-Zener prediction agrees fairly well at high photofragment velocities and deviates strongly from the experiment as the velocity decreases. This failure of the model is expected and has been discussed by several authors [25, 26]. Never

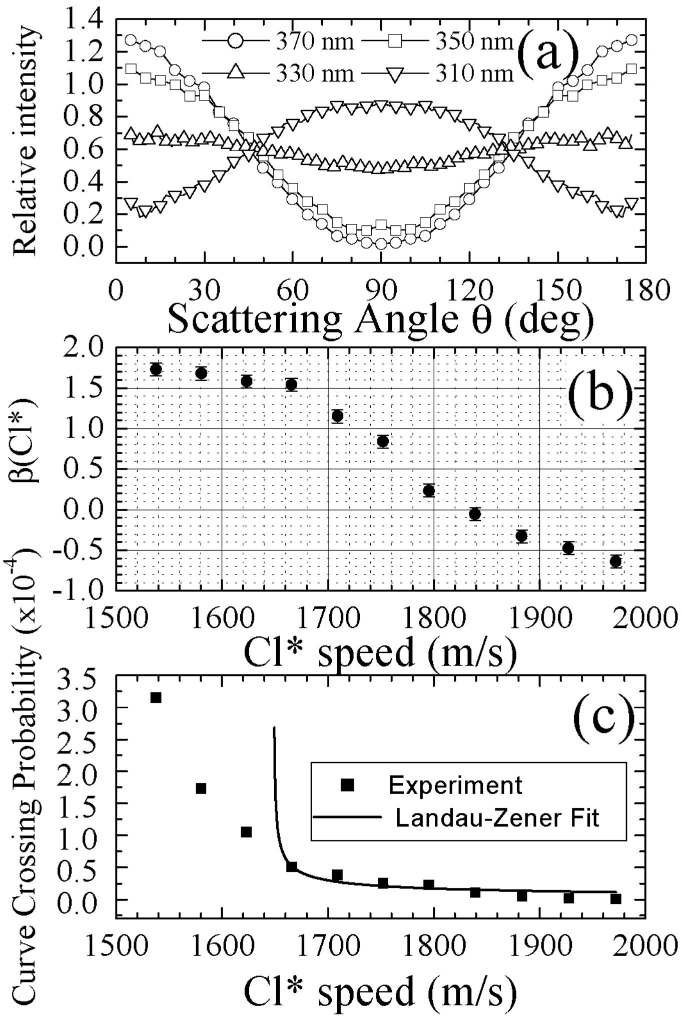

Figure 2.5: *(a) Angular distributions for the Cl* photofragment generated from the photodissociation of* Cl_2 *at various wavelengths. (b) Plot of the* $\beta(Cl^*)$ *as a function of Cl* speed. (c) Curve crossing probability as a function of Cl* speed.*

Table 2.3: *Values for the anisotropy parameter* $\beta_{eff}(Cl^*)$ *determined from inverse Abel transform of the Cl* images and the calculated curve crossing probability* P_{cc} *for differents wavelengths* λ.

λ (nm)	310	315	320	325	330	335	340	345	350	355	360	390
$\beta_{eff}(\pm 0.05)$	-0.64	-0.47	-0.33	-0.06	0.24	0.84	1.15	1.54	1.58	1.68	1.73	2.0
$P_{cc}(\times 10^{-4})$	0.01	0.02	0.05	0.11	0.23	0.25	0.38	0.51	1.05	1.73	3.16	-

the less, the fair agreement with the data does allow us to predict E_{cc} to a first order approximation.

Note that in Fig. 2.4(a) the Cl*/Cl branching ratio begins to increase significantly only above ~370 nm, while in Table 2.3 it is seen that above ~370 nm β_{eff} is only slightly less than 2.0, the value for a pure parallel transition. This means that the relative contribution of curve crossing to $\varepsilon(0_u^+)$ is quite small. At the longest dissociation wavelengths, the Cl*/Cl branching ratio appears to drop slightly, which may be interpreted as a small contribution from the lower-lying $A(1)^3\Pi_1$ state [1, 2, 3], which correlates with Cl+Cl. This state is reached via a perpendicular transition, which would lower the observed value of β_{eff}.

2.4.3 Product alignment

The Cl atoms from channel II are expected to show the same angular distribution as their Cl*-atom partners. In the wavelength region greater than 370 nm, attempts to fit the Cl channel II distribution using Eq. (2.4) yield β values around 1.60, in contradiction with the value of ~2.0 from the Cl* results. As the only difference between the two methods is the probe REMPI scheme, this deviation must be attributed to a different angular detection sensitivity in the case of Cl ($^2P_{3/2}$). Atomic alignment is only possible when the angular momentum is greater than 1/2. Therefore the Cl (J=3/2) atoms can show an aligned m_J-state distribution described by a quadrupole moment, $A_0^{(2)}$, whereas the Cl* (J=1/2) atoms cannot. Alignment of Cl atoms from the photodissociation of Cl_2 has been reported previously [27, 28]. The aligned m_J-state distribution can influence the ionization efficiency of the linearly polarized REMPI process, and since the alignment can be correlated with the recoil velocity this detection-sensitivity bias can appear in the detected angular direction of the photofragments. In the absence of alignment, the experimental angular distributions can be fit to Eq. (2.4). It is well known that product alignment can cause the detected angular distributions to be described by a larger expansion [29]. For $1 \leq J \leq 3/2$, the expansion is terminated at the fourth order Legendre polynomial:

$$I(\theta) \sim 1 + \beta_2 P_2(\cos\theta) + \beta_4 P_4(\cos\theta) \tag{2.9}$$

For a parallel geometry (i.e. the polarizations of the photolysis and probe lasers are parallel), the experimental angular distribution can be described by the product of the real angular distribution [Eq. (2.4)] and the alignment-dependent detection probability [30]:

$$I(\theta) \sim [1 + \beta P_2(\cos\theta)][1 + A_0^{(2)} P_2(\cos\theta)] \tag{2.10}$$

Equation (2.10) can be rewritten in the form of Eq. (2.9) so that coefficients β_2 and β_4 can be expressed in terms of the spatial anisotropy parameter, β and the laboratory-frame quadrupole alignment, $A_0^{(2)}$:

$$\beta_2 = \frac{\beta + A_0^{(2)}(1 + \frac{2}{7}\beta)}{1 + \frac{1}{5}\beta A_0^{(2)}}, \quad \beta_4 = \frac{\frac{18}{35}\beta A_0^{(2)}}{1 + \frac{1}{5}\beta A_0^{(2)}}, \tag{2.11}$$

The laboratory-frame $A_0^{(2)}$ parameter can be expressed in terms of the more physical molecular-frame polarization parameters:

$$A_0^{(2)} = G_c s_2 a_0^{(2)}(\|) \tag{2.12}$$

for a parallel transition, and

$$A_0^{(2)} = \frac{a_0^{(2)}(\perp) - \sqrt{\frac{2}{3}}a_2^{(2)}(\perp)}{\frac{1}{G_c s_2} + \sqrt{\frac{2}{3}}a_2^{(2)}(\perp)} \tag{2.13}$$

for a perpendicular transition, where the $a_q^{(k)}(||)$ and $a_q^{(k)}(\perp)$ are molecular-frame polarization parameters [30, 31]. The factor G_c is the long-time-limit hyperfine-depolarization coefficient and is equal to 0.27 for this study, [32] while s_2 is the relative detection sensitivity of the parameters with k=2 and has been empirically calibrated to be 1.1±0.1 for the $4p(^4P_{3/2})\leftarrow 3p5(^2P_{3/2})$ transition [33].

The experimental angular distribution for channel II is fit with Eq. (2.9) to give β_2=1.82 and β_4=-0.24, which are consistent, within experimental error, with the limiting values of $\beta(0_u^+)$=+2 and $a_0^{(2)}(||)$=-0.8 [see Eqs. (2.12) and (2.13)]. The negative maximal value of $a_0^{(2)}(||)$=-0.8 corresponds to population of only m_J=±1/2 with respect to the recoil direction of the Cl atoms [31]. The Cl* (J=1/2) atoms associated with the Cl atoms can only populate m_J=±1/2, and the $B(0_u^+)$ state possesses no net projection of the total angular momentum along the bond axis. Since m_J(Cl)+ m_J(Cl*)=0, the Cl atoms are constrained to be maximally aligned for this dissociation.

The experimental angular distribution for channel I is fit with Eq. (2.9) to give β_2=-1 and β_4=0, thus showing negligible alignment in the laboratory frame. However, examination of Eq.(2.13) shows that if the molecular-frame parameters $a_0^{(2)}(\perp)$ and $a_2^{(2)}(\perp)$ possess the same sign and similar magnitude, then a large molecular-frame alignment can nevertheless appear as a negligible laboratory-frame alignment, $A_0^{(2)}$, when the polarizations of the photolysis and probe lasers are parallel. Measurements elsewhere have indeed shown such molecular-frame alignments [28, 33]. Overall, we have shown the ability to decouple the measurements of and alignment effects from parallel-geometry imaging experiments using Eqs. (2.9) and (2.11).

2.5 Conclusion

The photodissociation of Cl_2 has been studied between 310 and 470 nm. From the speed distributions of the Cl photofragments we are able to determine the Cl*/Cl branching ratio as a function of photolysis wavelength and find it to increase as the wavelength increases, reaching a maximum around 430 nm. From the determined branching ratio we are able to model the absorption cross section for the 0_u^+ and 1_u excited electronic states of Cl_2 using two Gaussian functions. Analysis of the photofragment angular distributions indicate that the $Cl(^2P_{3/2})$ photofragments are aligned and the magnitude of this alignment is quantitatively determined. The dependence of angular distribution of the Cl* photofragment on the excitation energy, allows us to determine the nonadiabatic curve crossing probability between the 0_u^+ and 1_u electronic states. Our results agree reasonably to a Landau-Zener type behavior, particularly at the large photofragment velocities, and from this model we estimate the position of the curve crossing at ~3 eV above the ground electronic state of Cl_2.

Acknowledgments

A large part of this work is conducted at the Ultraviolet Laser Facility operating at FORTH-IESL (TMR, Access to Large Scale Facilities EU program, Contract No. CHGE-CT92-007) and is also supported by TMR Network *IMAGINE* ERB 4061 PL 97-0264). The work in Nijmegen is supported by the same TMR Network, and by the Stichting NWO-FOM. TNK greatly acknowledges the generosity of Photek Ltd, for providing us with the microchannel plates used in these experiments.

References

[1] R.S. Mulliken, Phys. Rev. **36**, 1440 (1930).
[2] G. Herzberg, *Molecular Spectra and Molecular Structure I, Spectra of Diatomic Molecules* (Van Nostrand Reihnhold, NY, 1950), p. 319-322.
[3] L. Li, R.J. Lipert, J. Lobue, W.A. Chupka, and S.D. Colson, Chem. Phys. Lett. **151**, 335 (1988).
[4] Y. Matsumi, K. Tonokura, and M. Kawasaki, J. Chem. Phys.**97**, 1065 (1992).
[5] Y. Matsumi, M. Kawasaki, T. Sato, T. Kinugawa, and T. Arikawa, Chem. Phys. Lett. **155**, 486 (1989).
[6] M. Brouad, S.P. Duxon, P.A. Enriquez and J.P. Simons, J. Chem. Phys. **97**, 7414 (1992).
[7] R.N. Zare, Mol. Photochem. **4**, 1 (1972).
[8] S. Yang and R. Bersohn, J. Chem. Phys. **61**, 4400 (1974).
[9] A.T.J.B. Eppink and D. H. Parker, *Rev. Sci. Instrum.* **68**, 3477 (1997).
[10] P.C. Samartzis, I. Sakellariou, T. Gougousi, and T.N. Kitsopoulos, *J. Chem. Phys.* **107**, 43 (1997).
[11] S. Arepalli, N. Presser, D. Robie, and R.J. Gordon, Chem. Phys. Lett. **118**, 88 (1985).
[12] C.E. Moore, *Atomic Energy Levels as derived from the analyses of optical spectra* (Washington, U.S. Dept. of Commerce, National Bureau of 1949).
[13] W.R. Simpson, T.P. Rakitzis, A.A. Kandel, J. Orr-Ewing, and R.N. Zare, *J. Chem. Phys.* **103**, 7313 (1995).
[14] R.N. Barcewell, Aust. J. of Phys. **9**, 198 (1956).
[15] D.W. Chandler, T.N. Kitsopoulos, M.A. Buntine, D.P. Baldwin, R.I. McKay, A.J.R. Heck, and R.N. Zare, *Gas-Phase Chemical Reaction Systems: Experiments and Models 100 Years after Max Bodenstein*, eds. J. Wolfrum, H.-R. Volpp, R. Rannacher, J. Warnatz (Springer Series in Chem. Phys. (Springer Berlin, Heidelberg 1996).
[16] D.W. Chandler and P.L. Houston, J. Chem. Phys. **87**, 1445 (1987).
[17] A.J.R. Heck and D.W. Chandler, Annu. Rev. Phys. Chem. **46**, 335 (1995).
[18] P.L. Houston, J. Phys. Chem. **100**, 12757 (1996).
[19] M.N. Al-Kahali, R.J. Donovan, K.P. Lawley, Z.Min, and T.Ridley, *Chem. Phys.* **208**, 165 (1996).
[20] B.L.G. Bakker, P.C. Samartzis, T.N. Kitsopoulos and D.H. Parker (in preparation).
[21] W.B. DeMore, S.P. Sander, D.M. Golden, R.F. Hampson, M.J. Kurylo, C.J. Howard, A.R. Ravishankara, C.E. Kolb, M.J. Molina, "*Chemical Kinetics and Photochemical Data for Use in Stratospheric Modeling*", Evaluation No. 11, JPL Publication 94-26, Jet Propulsion

Laboratory, Pasadena CA, 1994.
[22] K.P. Huber and G. Herzberg, *Constants of Diatomic Molecules* (Van Nostrand Reihnhold, NY, 1979), p. 146.
[23] G.E. Gibson, O.K. Rice, and N.S. Bayliss, Phys. Rev. **44**, 193 (1933).
[24] R.D. Levine and R.B. Bernstein, *Molecular Reaction Dynamics and Chemical Reactivity* (Oxford press, NY 1987), p. 377.
[25] E.E. Nikitin, *Theory of Elementary Atomic and Molecular Processes in Gases* (Oxford press, NY 1974), p. 107.
[26] M.S. Child, *Molecular Collision Theory* (Academic Press, New York 1974), p.164, and references therein.
[27] Y. Wang, H.P. Loock, J. Cao, C.X.W. Qian, *J Chem. Phys.* **102**, 808 (1995).
[28] A.S. Bracker, E.R. Wouters, A.G. Suits, Y.T. Lee, and O.S. Vasyutinskii, *Phys. Rev. Lett.* **80**, 1626 (1998).
[29] R.N. Dixon, *J. Chem. Phys.* **85**, 1866 (1986).
[30] T.P. Rakitzis and R.N. Zare, J. Chem. Phys. (submitted).
[31] L.D.A. Siebbeles, M. Glass-Maujaan, O.S. Gvayutinski, J.A. Beswick and O. Roncero, I *J.Chem. Phys.* **109**, 3610 (1994).
[32] T.P. Rakitzis, S.A. Kandel, and R.N. Zare *J.Chem. Phys.* **108**, 8291 (1998).
[33] T.P. Rakitzis, S.A. Kandel, and R.N. Zare, (unpublished results).
[34] T.P. Rakitzis, S.A. Kandel, A.J. Alexander, Z.H. Kim, and R.N. Zare, (unpublished).

Chapter 3

The sequential two-photon dissociation of NO as a source of aligned N(^{2}D), N(^{4}S) and O(^{3}P) atoms.

Abstract

Velocity map imaging is used to characterize the angular distributions of atoms which are formed from the sequential two photon excitation of NO via the $A^2\Sigma^+$ state. Molecules excited at 226 nm and dissociated at 339 nm from the same laser source yield two sets of products, ground state O(^{3}P) atoms in conjunction with N(^{2}D) and N(^{4}S). The angular distributions are found to be well described by β parameters. The use of this method as a source of monoenergetic aligned atoms for studies of reaction dynamics is discussed.

3.1 Introduction

One of the most significant developments in gas phase reaction dynamics over the past ten years has been in the use of laser prepared reagents to study the stereodynamics of chemical reactions. Polarized laser photolysis of a suitable precursor molecule forms a velocity aligned reagent (generally an atom), and measurements of the polarization of its reaction products probed by Laser Induced Fluorescence (LIF) or Resonance Enhanced Multiphoton Ionisation (REMPI) can give unprecedented detail about the quantum state resolved dynamics of the reaction [1, 2, 3]. When a diatomic molecule is used as the precursor, then photolysis produces an essentially monoenergetic reagent distribution, as for example in studies of the reactions of H and Cl atoms formed by photolysis of HI [4, 5], HBr [6] and Cl_2 [7]. In contrast, reactions of oxygen atoms have relied on the photolysis of the triatomic precursors N_2O [8, 9] and O_3 [10] for $O(^1D)$, and NO_2 [11, 12] for $O(^3P)$ and this necessarily complicates the interpretation of the measured polarizations, as the atomic reagent now has a range of kinetic energies and possibly a speed dependent anisotropy.

Here we describe a straightforward method of producing aligned nitrogen and oxygen atoms by the sequential two photon dissociation of NO via the $A^2\Sigma^+$ state. We form monochromatic $N(^2D)$ atoms in conjunction with ground state $O(^3P)$, and observe a second channel forming fast ground state O and N atoms. In this report we concentrate on the translational anisotropy of the $N(^2D) + O(^3P)$ channel measured by velocity map imaging of both fragments [13], and discuss the use of this method as a strategy to study the reactions of monoenergetic velocity aligned N and O atoms.

3.2 Experimental

The velocity mapping apparatus, a variant of ion imaging [14] has been described in detail before [13, 15], and is summarized here. A pulsed supersonic beam of 20% NO in He (1 bar) is directed down the axis of a time-of-flight (TOF) mass spectrometer, and crossed at right angles with the counterpropagating pulsed dye laser beams. The output of the first dye laser (678 nm) is both frequency doubled and tripled to produce radiation at 226 and 339 nm. These beams are separated and used first to excite NO to the $A^2\Sigma^+$ state near 226 nm ($\sim$0.4 mJ pulse^{-1}, irised to match the 1.2 mm diameter molecular beam), and then to dissociate by absorption at 339 nm ($\sim$2 mJ pulse^{-1} loosely focused to the same diameter).

Atomic products are ionized by REMPI (resonance enhanced multiple photon ionisation), using the output of a second dye laser focused tightly on the molecular beam with a 20 cm lens. Three detection schemes were successfully used, for $N(^2D)$ at 269 nm [16], $O(^3P)$ at 226 nm [17] and $N(^4S)$ at 211 nm [18]. Less than 1 mJ pulse of the radiation (produced by frequency doubling) was required. The detection laser pulse arrived $\sim$20 ns after the production pulse. In each case the detection laser wavelength was scanned repetitively across the transition's Doppler profile to ensure equal detectivity for all velocity groups.

Ions formed by REMPI were extracted from the ionisation region into the grounded time-of-flight tube and crushed onto a two-dimensional microchannel plate/phosphor screen detector read by a CCD camera. An electrostatic immersion lens [13] is used, which projects all ions with the same velocity to the same point on the 2D detector regardless of their position of origin in the ionisation volume, improving the velocity resolution compared to the use of grids in conventional ion imaging. Mass selectivity is achieved by pulsing the gain of the detector as the N^+ or O^+ ions arrive. Even without such pulsing, the residual gain is high enough to amplify the residual NO^+ signal, which is intense enough in some cases to appear in the middle of the image (no kinetic energy release) as a leakage signal. Typically 5000 laser shots were used to produce the final image, which was inverted (2D-3D) using a Hankel inversion program.

3.3 Results

The NO A-X transition lies in a convenient range for laser excitation (around 226 nm for the 0-0 band [19]) and a large volume of molecules can be excited with unfocused laser light. Dissociation of the excited molecules to form the aligned atoms should ideally be carried out with photons which are produced by the **same** laser but are normally unused. None of the pump YAG laser harmonics (532, 355 and 266 nm) were found to dissociate the NO A state to produce measurable atomic products. 452 nm radiation, available when producing the 226 nm light by frequency doubling was similarly unsuccessful. 339 nm radiation however, which comes ”free” when 226 nm light is formed by frequency tripling, was found to be particularly efficient in producing energetic atoms.

Sequential two step dissociation of NO using (226 + 339) nm photons and detection of $N(^2D_{3/2})$ atoms using 269 nm photons yields the raw image shown in Fig. 3.1. In these experiments the A-X laser is set at 44197.5 ± 2 cm^{-1} (226.19 nm) at the $Q_{11}+P_{21}$ bandhead, exciting predominantly the N”=1, 2 and 3 rotational states which form the majority of population in the cold molecular beam, and producing $A^2\Sigma^+$ molecules with the same values of N’ ($\Delta N=0$). The laser polarisations all lie parallel to the detector face, and thus along the vertical axis of Fig. 3.1. Under these conditions, transformation of the 2D image to the original 3D pattern using the Hankel inversion is possible, and yields the angle integrated kinetic energy distribution shown in Fig. 3.2(a). Calibration of the velocity and thus kinetic energy release of the atoms is based on the known properties of the inversion lens, which were checked against distributions previously measured for $O(^3P)$ detection from the photolysis of molecular oxygen [15].

Three features can be seen in Fig. 3.2(a). At low kinetic energies there is a leakage signal, present when both the 339 and 269 nm laser beams are blocked, and which arises from NO^+ formed in the 1+1 REMPI of NO at 226 nm. An outer ring, with 0.66 eV kinetic energy, is also seen in the absence of 339 nm radiation, and is caused by dissociation of A state molecules by absorption of the 269 nm REMPI detection radiation. The major peak at 0.14 eV is at precisely the position expected for the sequential 226+339 nm steps forming $N(^2D)$ together with ground state $O(^3P)$.

Figure 3.2(b) shows the angular distribution of the 0.14 eV peak. Maximum signal is seen at 90^0 to the laser beams’ polarisation axis (as can clearly be seen in the image of Fig. 3.1), and when fitted to the equation $I(\theta)=1+\beta P_2(\cos\theta)$, where $P_2(\cos\theta)$ is the second order Legendre polynomial, yielded a value of $\beta=-0.8\pm0.05$. The errors represent a 1σ deviation from the results of 7 separate experiments. In the A-X transition we are in principle forming aligned NO molecules, and thus the angular distribution of the dissociation products should not be described by this simple expression. In practice the alignment is likely to be small for the following reasons. Excitation to the A state is in both Q and P branch transitions which have opposite polarisations relative to the angular momentum vector **J** and similar line strengths at low N”, and the dissociation step is from A state molecules whose alignment is reduced by rotation. Hyperfine depolarisation will also reduce the alignment in these low N’ levels. These effects are expected to wash out any alignment in the A-X excitation, and this was experimentally confirmed by the invariance in the β value found when the polarisation vector of the 226 nm beam was rotated so that it was along the TOF axis. Incorporating a $P_4(\cos\theta)$ term in the angular distribution produced only marginally better fits. The detection step, 2+1 REMPI at 269 nm, can also be selective if atoms are formed with an anisotropic distribution of m_J states, and the absorption steps are polarisation dependent. This effect was shown to be insignificant by the invariance of the angular distributions on rotation of the 269 nm polarisation vector with respect to that of the dissociating 339 nm beam. Our results suggest that the angular distributions of $N(^2D)$ are well described by a single β parameter, but we note that we have been unable to find evidence that the m_J substates are aligned with respect to the atomic velocity vector. Experiments on the $N(^2D_{5/2})$ state produced the same images as for $N(^2D_{3/2})$.

Fig. 3.3 shows the raw image when $O(^3P_2)$ atoms were detected following 226+339 nm

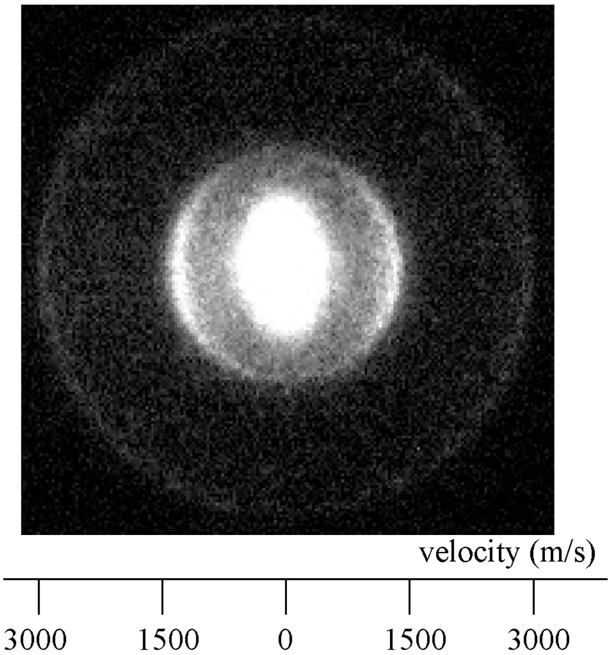

Figure 3.1: *Raw image of* N^+ *formed from* $N(^2D_{3/2})$ *by REMPI at 269 nm following the sequential two photon excitation of NO at 226 + 339 nm. The 339 nm beam polarisation vector is along the vertical axis of the Figure. The asymmetric inner feature is from* NO^+ *leakage signal caused by 1+1 REMPI of the molecule at 226 nm. The pronounced feature at a velocity of 1400* ms^{-1} *can be clearly seen as arising from fragments travelling perpendicular to the polarisation vector: in addition a weak outer ring is observed.*

dissociation, and the angle integrated kinetic energy distribution is shown in Fig. 3.4(a). The "inner ring" at 0.13 eV is at the position expected for the N(^{2}D) + O(^{3}P$_2$) channel, and the angular distribution, an example of which is shown in Fig. 3.4(b), yields a value of β=-0.71±0.17 from the analysis of 23 separate images, in agreement with the N(^{2}D) data. An outer ring at 1.23 eV is also seen, and corresponds to the formation of fast O(^{3}P$_2$) together with ground state N(^{4}S) atoms. Its polarisation is found to correspond to a parallel transition (β=1.0±0.27). The branching ratio for the channels [O(^{3}P$_2$) + N(^{4}S)]:[O(^{3}P$_2$) + N(^{2}D)] was found to be 0.3±0.1. In addition a NO$^+$ leakage signal (the central blob in Fig. 3.3) and an additional signal at 0.94 eV were seen in the absence of 339 nm light. Both signals are caused by the O(^{3}P$_2$) detection laser

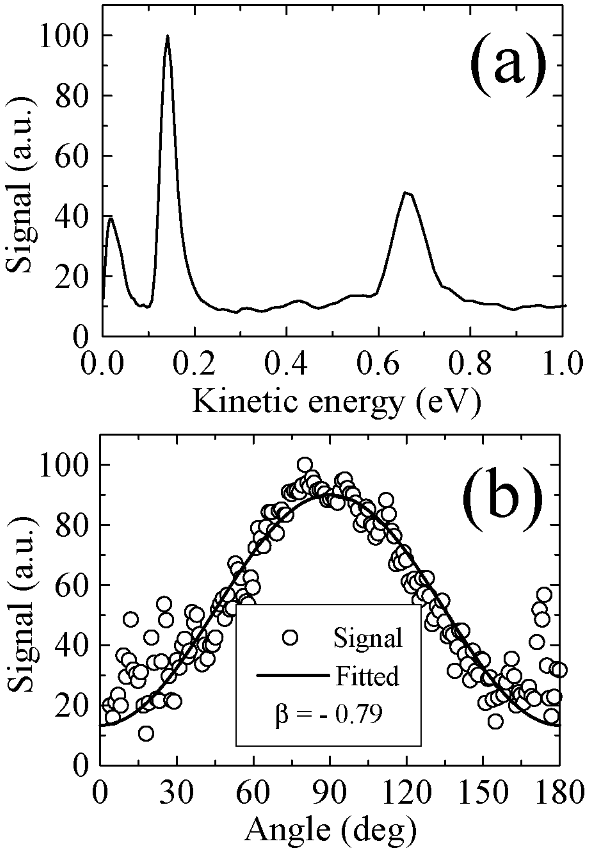

Figure 3.2: *(a) Upper panel: angle integrated kinetic energy distribution of the N(^{2}D$_{3/2}$) fragment taken from the data of Fig. 3.1. The inner leakage signal from NO$^+$ gives rise to the feature at low kintetic energy (0.03 eV), the major peak at 0.14 eV is from sequential 226 + 339 nm dissociation of NO to give N(^{2}D) + O(^{3}P), and the peak at 0.66 eV (the outer ring of Fig. 3.1) is from 226 + 269 nm absorption, the latter wavelength being that used to ionise N(^{2}D). (b) Lower panel): angular distribution of the 0.14 eV N(^{2}D$_{3/2}$) peak relative to the 339 nm laser polarisation vector. A perpendicular transition is seen, with the data fitted to yield a β parameter of -0.79 for this data set.*

set at 225.7 nm, which can either ionise the A state molecules or dissociate them to form the N(^{2}D) product. Both of these signals are unavoidable with O(^{3}P$_2$) detection, but would be absent in a photolysis experiment. The angular distributions of the signals caused by the detection laser, and the dynamics of the channel forming ground state products will be described in a future publication [20]. Detection of O(^{3}P$_1$) and O(^{3}P$_0$) requires wavelengths which are more closely resonant with NO A-X transitions in the molecular beam. The resultant high density of NO$^+$ ions (from 1+1 REMPI) yielded space charge effects which precluded taking meaningful images for these two states.

Detection of N(^{4}S) atoms by REMPI at 211 nm showed a strong feature corresponding to the N(^{4}S) + O(^{3}P) channel with a β value agreeing within experimental error with that found for the "outer ring" in Fig. 3.4. No evidence of a channel forming O(^{1}D) + N(^{4}S) was seen both in these experiments and in attempts to observe O(^{1}D) directly by REMPI.

3.4 Discussion

A schematic potential energy diagram of the relevant NO electronic states and their dissociation limits is shown in Fig. 3.5. The absorption of 339 nm light by A state NO brings the molecule to a total energy of 9.14 eV, which is below the ionisation potential, 0.26 eV above the N(^{2}D) + O(^{3}P) dissociation limit, 0.67 eV above the O(^{1}D) + N(^{4}S) limit and 2.64 eV above the N(^{4}S) +

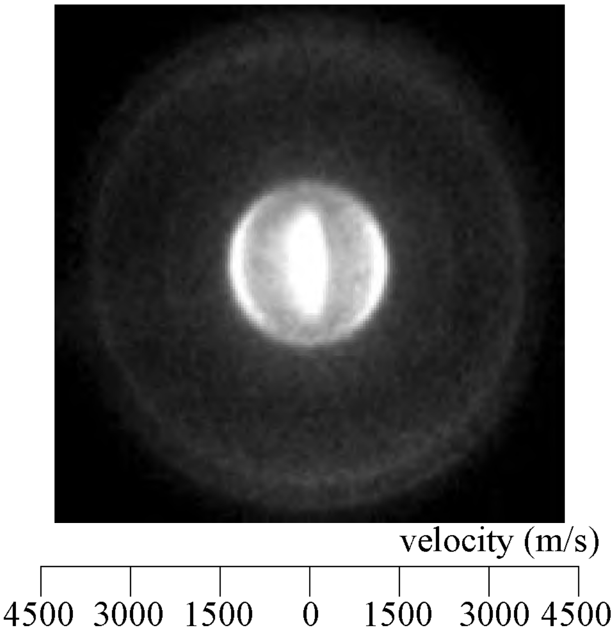

Figure 3.3: *Raw image of O$^+$ formed from O(^{3}P$_2$) by REMPI at 225.7 nm following irradiation of NO at 226 + 339 nm. As in Fig. 3.1, the inner "blob" is caused by leakage signal from NO$^+$. The perpendicular transition giving O atoms with a velocity of 1250 ms^{-1} is clearly seen, together with diffuse outer rings.*

O(^{3}P) limit. The (spin forbidden) O(^{1}D) + N(^{4}S) channel is found to be inactive. Conservation of momentum and energy predicts the production of N(^{2}D) atoms with 0.14 eV kinetic energy, and of O(^{3}P) atoms with 1.23 and 0.13 eV kinetic energy, in agreement with the observed values.

Photodissociation properties of NO excited below the ionisation potential have been reported in several studies. Slanger and co-workers [21] were the first to show that NO predissociates following simultaneous two-photon excitation around 270 nm to high vibrational levels of the ndπ Rydberg states, forming N(^{2}D) atoms. Umemoto and Matsumoto [22] showed that two photon excitation at 275.3 nm is an efficient method of forming N(^{2}D), and this has been used as a source of the atom in studies of the N(^{2}D) + H_2 reaction [23]. The main dissociation channel

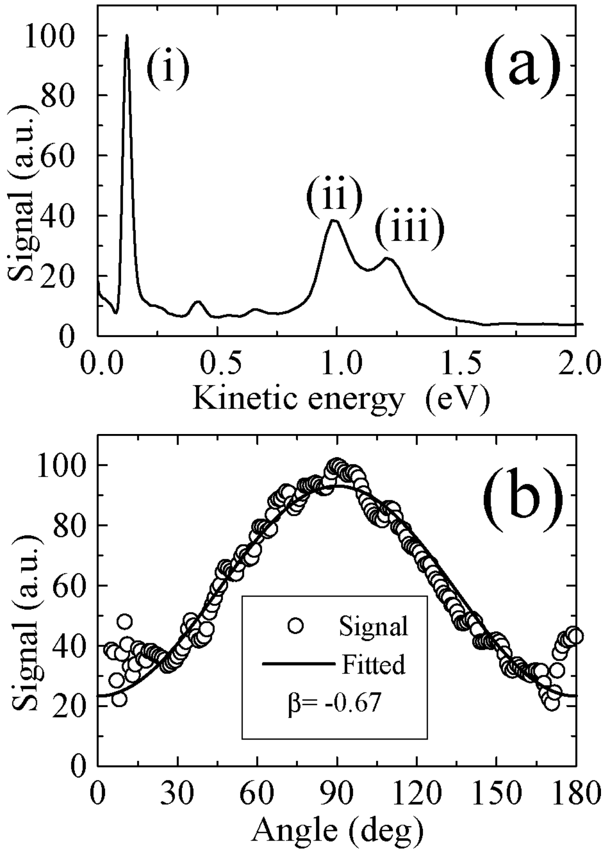

Figure 3.4: *(a) Upper panel): angle integrated kinetic energy distribution of the O($^3P_2$) fragment taken from the data of Fig. 3.3. Feature (i) is from 226 + 339 nm sequential dissociation of NO, and is the O atom counterpart of the 0.14 eV peak seen in Fig. 3.2(a). Feature (ii) at 0.94 eV is from 226 + 225.7 nm sequential two photon dissociation to give N(^{2}D) + O(^{3}P) products, the 225.7 nm radiation both exciting the A state NO molecules and ionising the O(^{3}P). The outer ring (iii) at 1.23 eV is from 226 + 339 nm dissociation forming ground state N(^{4}S) + O(^{3}P) atoms. (b) Lower panel: angular distribution of peak (i) in Fig. 3.4(a). A β value of -0.67 was returned for this data set.*

of the npπ Rydberg states appears to be predissociation via the repulsive wall of the bound L$^2\Pi$ valence state (see Fig. 3.5) [25]. Direct dissociation via repulsive valence states or via the repulsive wall of bound valence states has not been indicated in previous studies, and the present lack of signals at non-resonant wavelength agrees with this.

Photoexcitation of low rotational levels of the A$^2\Sigma^+$ (v=0) state by 335-345 nm photons has been reported by Fujii and Morita [25, 26, 27] and more recently by Geng *et al.* [28]. These studies, and the earlier work of Anezaki *et al.* [29] have shown that two Rydberg states, the 11p(v=0) and the 10f(v=0), lie in this region. In the present experiment the second photon is at 29465 cm^{-1}, and is near (but not exactly resonant with) transitions from N'=2 of the A state to the sublevels of the 11p complex which were observed by Geng *et al.* [28]. The photon energy however is resonant with an allowed (but apparently weak [28]) P branch transition from N'=3 in the A state to N=2 in the $^2\Pi^+$ component of the 11p Rydberg state, and we note that N'=3 is populated following absorption at 226.19 nm. The 11p $^2\Pi$ levels are known to be broadened by predissociation through coupling to the L valence state continuum [24, 28] or the repulsive part of the B valence state [28], both of which lead to N(^{2}D) + O(^{3}P) products. The excitation

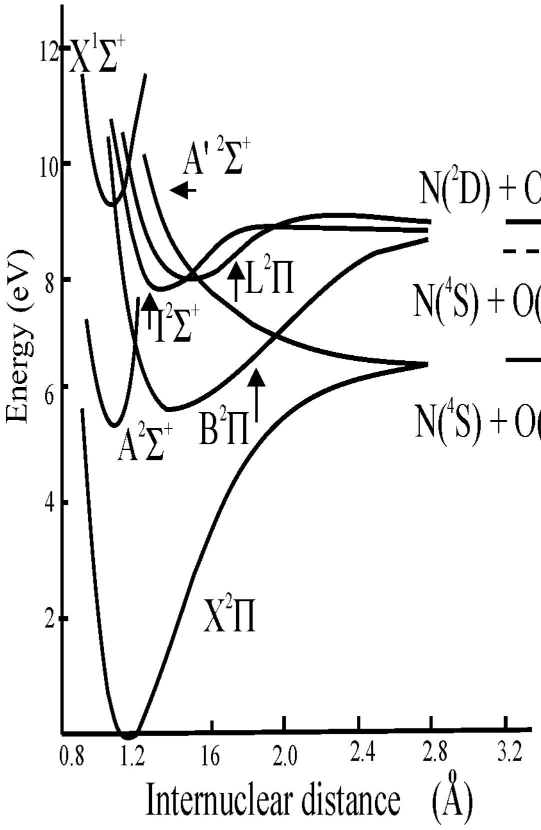

Figure 3.5: *Potential energy curves for NO, showing the positions of the dissociation limits and of the valence curves correlating with them.*

process is thus $11p^2\Pi \leftarrow A^2\Sigma^+$, and should give a perpendicular transition ($\beta < 0$), as observed. Furthermore, we can expect a reduction of the magnitude of the anisotropy parameter β from its limiting value because of the Rydberg state lifetime. A change of β from -1 to -0.75 (the average of the measurements on the N(^{2}D) and O(^{3}P) channels) would be consistent with the $^2\Pi^+$ N=2 rotational level having a lifetime of 6 ps, which would result in a 0.9 cm^{-1} linewidth. Geng *et al.* observed a linewidth of ~5 cm^{-1} for the N=3 level of this state [28] and Fujii *et al.* observed a linewidth of ~3 cm^{-1} for the 11p state [27] : we note that our estimate of the linewidth from the β value depends upon the rotational frequency used in the Rydberg level, and hence upon the value of N.

The predissociation mechanism for the channel forming N(^{4}S) + O(^{3}P) in a parallel transition is less straightforward, but may be accounted for by absorption to a $^2\Sigma$ component of either the 11p or 10f Rydberg states: current experiments in which the excitation wavelength and laser power near 339 nm will be independently varied are aimed to unravel the dissociation dynamics in this region.

3.5 A strategy for hot atom production

The cross section for excitation of the 11p Rydberg state from the NO A state has been estimated as 2.5 x 10^{-18} cm^2 [25], and thus with presently available laser powers a volume of aligned atoms similar to that formed in single photon dissociation processes can be produced. This should enable full vector correlations to be measured for reactions of highly aligned N(^{2}D) atoms: the method has an advantage over the two photon excitation process near 275 nm [22, 23] in that a focused laser beam must be used in the latter process, and that this step appears to produce essentially velocity unaligned N(^{2}D) atoms and also a substantial and very wavelength dependent contribution from the channel forming hot ground state atomic products [20]. For O(^{3}P) atoms the present method is not ideal, forming as it does two sets of monochromatic atoms with opposite values of β. It however points the way to a future strategy involving predissociation of other Rydberg states which lie below dissociation limits other than to ground state atoms, but which can only be reached if a separately tunable laser source is available. Highly translationally excited O(^{3}P) atoms can be formed, thus overcoming the energy barriers which are generally associated with this atomic reactant: an additional bonus is that fast N(^{4}S) can also be produced.

One potential problem in the method will be seen if LIF is used as a the probe for the reactions of such aligned atoms - strong emission from the NO A state will always be present as a background signal. However, if REMPI detection is used this problem disappears, and a further advantage is gained, in that co-expansion of NO precursor with the reagent will lead, as in the present study, to population in only a small number of rotational levels, and thus enable a high proportion of the ground state molecules to be excited. Such studies are currently underway in our laboratory.

Acknowledgments

The work in Nijmegen is part of the program of the Foundation Fundamental Research on Matter (FOM) and was made possible by financial support from The Netherlands Organisation of

Science (NWO). We are grateful to the British Council for a travel grant.

References

[1] A.J. Orr-Ewing and R.N. Zare, in *"Chemical Dynamics of Small Free Radicals"* eds. K. Liu and A.L. Wagner (World Scientific, Singapore, 1995).
[2] M. Brouard and J.P. Simons, in: *"Chemical Dynamics of Small Free Radicals"* eds. K. Liu and A.L. Wagner (World Scientific, Singapore, 1995).
[3] A.J. Orr-Ewing, J. Chem. Soc. Faraday Trans. **92**, 881 (1996).
[4] N.E. Shafer, H. Xu, R.P. Tuckett, M. Springer and R.N. Zare, J. Phys. Chem. **98**, 3369 (1994).
[5] R. Fei, X.S. Zheng and G.E. Hall, J. Phys. Chem. **101**, 2541 (1997).
[6] M. Brouard, H.M. Lambert, S.P. Rayner and J.P. Simons, Mol. Phys. **89**, 403 (1996).
[7] W.R. Simpson, A.J. Orr-Ewing and R.N. Zare, Chem. Phys. Lett. **212**, 163 (1993).
[8] M. Brouard, H.M. Lambert, J. Short and J.P. Simons, J. Phys. Chem. **99** , 13571 (1995).
[9] A.J. Alexander, M. Brouard, S.P. Rayner and J.P. Simons, Chem. Phys. **207**, 215 (1996).
[10] D.S. King, D.G. Sauder and M.P. Casassa, J. Chem. Phys. **97**, 8919 (1992).
[11] F. Green, G. Hancock and A.J. Orr-Ewing, Faraday Discuss. Chem. Soc. **91**, 79 (1991).
[12] M.L. Costen, G. Hancock, A.J. Orr-Ewing and D. Summerfield, J. Chem. Phys. **100**, 2754 (1994).
[13] A.T.J.B. Eppink and D.H. Parker, Rev. Sci. Instrum. **68**, 3477 (1997).
[14] A.J.R. Heck and D.W. Chandler, Annu. Rev. Phys. Chem. **46**, 335 (1995).
[15] D.H. Parker and A.T.J.B. Eppink, J. Chem. Phys. **107**, 2357 (1997).
[16] G. Black and L.E. Jusinski, Chem. Phys. Lett. **41**, 1339 (1987).
[17] D.J. Bamford, L.E. Jusinski and W.K. Bischel, Phys. Rev. A. **26**, 3497 (1987).
[18] C.P. Fell, J.I. Steinfeld and S.M. Miller, Spectrochem. Acta **46A**, 431 (1990).
[19] E. Meischer and F. Alberti, J. Phys. Chem. Ref. Data **5**, 309 (1976).
[20] B.L.G. Bakker, A.T.J.B. Eppink and D.H. Parker, to be published.
[21] L.E. Jusinski, G.E. Gadd, G. Black and T.G. Slanger, J. Chem. Phys. **90**, 4282 (1989).
[22] H. Umemoto and K. Matsumoto, J. Chem. Soc. Faraday Trans. **92**, 1315 (1996).
[23] H. Umemoto, T. Asai and Y. Kimura, J. Chem. Phys. **106**, 4985 (1997).
[24] A. Giusti-Suzor and Ch. Jungen, J. Chem. Phys. **80**, 986 (1984).
[25] A. Fujii and N. Morita, Chem. Phys. Lett. **182**, 304 (1991).
[26] A. Fujii and N. Morita, J. Chem. Phys. **97**, 327 (1992).
[27] A. Fujii and N. Morita, Laser Chem. **13**, 259 (1994).
[28] J. Geng, T. Kobayashi and M. Takami, Chem. Phys. Lett. **226**, 290 (1997).
[29] Y. Anezaki, T. Ebata, N. Mikami and M. Ito, Chem. Phys. **97**, 153 (1985).

Chapter 4

Two-photon dissociation of NO near 275 nm investigated by velocity map imaging

Abstract

The two photon dissociation of NO at wavelengths near 275 nm has been investigated by velocity map imaging of the O($^3P_2$) dissociation product. Two channels are seen, corresponding to formation of the co-product N atoms in their ground (^4S) and excited (^2D) states, and the relative yields and angular distributions measured. In their regions of maximum yield, the channel forming N(^2D) produces unaligned products, whereas that producing N(^4S) can be described by a β value of *ca.* 0.4. N(^2D)/N(^4S) ratios vary by a factor of 60 over a narrow range of excitation energies. The use of two photon excitation of NO as a source of aligned atoms for reaction stereodynamics is discussed.

4.1 Introduction

The dynamics of excited Rydberg states of NO has been the subject of considerable experimental and theoretical interest. At excitation energies between the first dissociation limit (leading to $N(^4S)$+$O(^3P)$ atoms) at 52472 cm^{-1} and the first ionisation limit at 74730 cm^{-1}, predissociation is the dominant fate of the species, with channels to give $N(^4S)$+$O(^1D)$ at 68340 cm^{-1} and $N(^2D)$+$O(^3P)$ at 71695 cm^{-1} being also energetically allowed. Information on the spectroscopy and dynamics in this region has been obtained through absorption experiments [1, 2], and by various multiphoton ionisation schemes [3, 4, 5, 6], but in only a few of these [4, 5, 6] have the products of the predissociation been detected, and there are few reported data on the angular distributions of the atomic fragments [7].

In this paper we present the results of velocity map imaging experiments [8] on the $O(^3P_2)$ product of the two photon dissociation of NO at excitation energies between 72807 and 72569 cm^{-1}. We observe markedly different wavelength dependences and angular distributions of the two channels which form $N(^4S)$ and $N(^2D)$ in conjunction with the observed $O(^3P_2)$ product. Our aim in these experiments was to exploit the two photon dissociation process as a strategy to form monoenergetic O and N atoms with known angular distributions for use in measurements of the stereodynamics of their chemical reactions [9, 10, 11]. We have already reported such measurements for the dissociation of NO by *sequential* excitation via the $A^2\Sigma^+$ state at an energy of 73663 cm^{-1} [7], but pointed out the difficulties of using this method when laser induced fluorescence (LIF) is used to detect the products of reaction. Umemoto *et al.* have successfully used the *coherent* two photon dissociation of NO near 72640 cm^{-1} to form $N(^2D)$ atoms and to study by LIF the scalar attributes of the NH product of their reaction with H_2 [12]. An extension of this technique to measurements of the vector correlations of the reaction requires a knowledge of the anisotropy of the dissociation process which we present here. We find largely unaligned $N(^2D)$ atoms near their region of maximum yield, 72643 cm^{-1}, but observe velocity aligned $N(^4S)$ atoms preferentially formed at excitation energies only 27 cm^{-1} below this, with the $N(^2D)/N(^4S)$ ratio varying by a factor of 60 over this narrow wavenumber range.

4.2 Experimental

The velocity mapping apparatus has been described in detail elsewhere [8], and only a brief summary is given here. A pulsed supersonic beam of 10% NO in He (1 bar) is directed down the axis of a time-of-flight (TOF) mass spectrometer and crossed at right angles by the counterpropagating photolysis and probe beams. The 275 nm radiation (2-8 mJ/pulse) was generated by the doubled output of a Nd:Yag pumped dye laser and focused on the molecular beam by a 20 cm focal length lens. The atomic product $O(^3P_2)$ was monitored by (2+1) REMPI at 226 nm, the radiation ($<$ 1mJ/pulse) produced from a second Nd:Yag pumped dye laser, delayed 20 ns from the photolysis pulse, and focused by a 20 cm focal length lens. In experiments in which the angular distributions were measured the detection laser wavelength was scanned repetitively across the transition's Doppler profile to ensure equal detectivity for all velocity groups. The ions produced by REMPI were extracted from the ionisation region into the grounded TOF tube and crushed onto a two dimensional microchannel plate/phosphor screen read by a CCD camera. Mass selectivity was achieved by pulsing the gain of the detector as the O^+ ions arrived. Typically 25,000 laser shots were used to produce the final image, which was processed using an inverse Abel transformation. Only O($^3P_2$) was studied, as the wavelengths required for ionisation of the other oxygen spin orbit components resulted in a high density of NO$^+$ from (1+1) REMPI.

4.3 Results

Images were taken at excitation energies between 72600 and 72800 cm^{-1} corresponding to irradiation wavelengths between 275.4 and 274.6 nm. In Figures 4.1(c) and 4.1(d) we present the Abel inverted images for two examples, excitation at 72643 and 72616 cm^{-1} respectively. In both cases a ring resulting from an O($^3P_2$) velocity of approximately 840 m/s can be seen, and corresponds to its formation in conjunction with N(^{2}D). Calibration of the velocity of the atoms is based on the known properties of the electrostatic immersion lens, which were checked against distributions measured for O($^3P_2$) formed from the photolysis of O_2 [8, 9, 10, 11, 12, 13]. For the photolysis at the longer wavelength an outer ring can be clearly seen at a velocity of 3760 m/s, that is expected for the formation of O($^3P_2$) together with ground state N(^{4}S) atoms. Figure 4.2 shows the velocity distribution in the two cases, indicating that a very weak outer ring is also produced at the shorter wavelength (but not visible in Figure 4.1(a)). The angular distributions for the two channels are also shown in Figure 4.2.

In Figures 4.3(a) and 4.3(b) the yields of the channels forming N(^{2}D) and N(^{4}S) are shown as a function of excitation wavenumber. In these experiments the REMPI laser was fixed at a single wavelength at the centre of the two photon transition in O($^3P_2$), thus preferentially detecting atoms with zero velocity along the laser propagation axis. In Figure 4.3(c) the true ratios of the two channels are shown at specific excitation wavenumbers for experiments in which all O($^3P_2$) velocity groups were sampled. These ratios are broadly consistent with the spectral variations shown in Figs 4.3(a) and 4.3(b), and indicate that the velocity selection in the latter does not distort the main features of the yield curves. The data shown in Figure 4.1 thus correspond to the peak of the N(^{2}D) yield curve at 72643 cm^{-1} and the nearby N(^{4}S) peak at 72616 cm^{-1}, and it can be seen that the ratios of N(^{2}D)/N(^{4}S) change from 25 to 0.4 over this small wavenumber range. The angular distributions I(θ), where θ is the angle between the fragment velocity and the polarization vector of the dissociating radiation were fitted to the expression $I(\theta) = 1 + \beta P_2(\cos\theta)$ where $P_2(\cos\theta$ is the second order Legendre polynomial, and the resultant values of β are displayed for the two channels as a function of wavelength in Figure 4.3(d). Figure 4.1 shows data from one particular experiment: the data of Figs 4.3(c) and 4.3(d) are averaged over at least five images and typical error bars 1σ are shown in Fig. 4.3(d).

The N(^{4}S) channel is always accompanied by a background signal, which spreads out over the full image and adds to the baseline in the inversion (see Fig. 4.2). The background requires the presence of both lasers and the molecular beam, and its origin is unknown. It has not been subtracted in the calculation of the β values, as its magnitude at the position corresponding to the N(^{4}S) velocity cannot be directly determined. If its behavior is the same as the background just to the sides of the N(^{4}S) peak in Fig. 4.2 then subtraction would lead to an increase in the β value of $\sim$10%, within the error bars of our measurements.

4.4 Discussion

We first look at the spectral features of Figures 4.3(a) and 4.3(b), and note that in the two photon spectroscopy of NO we expect an enhancement of the nd Rydberg series because of the resemblance of its HOMO (Highest Occupied Molecular Orbital) to a $3d\pi$ orbital in the united atom [3]. In the $N(^2D)$ spectrum the two major features peaking near 72750 and 72640 cm^{-1} have been observed before in two photon dissociation studies in which the $N(^2D)$ fragment was monitored. Gadd *et al.* [4] assigned these as transitions to the $5d\pi^-$ (v=1) and $4d\pi^-$ (v=2) states, both accessed in two photon transitions from the ground $^2\Pi_{1/2}$ (v=0) state of NO, and in the positions expected for these transitions as tabulated from the optical-optical double resonance measurements of Pratt *et al.* [3]. Umemoto and Matsumoto [6] observed similar spectra, but assigned the 72640 cm^{-1} band to the $5d\pi^-$ (v=1) $\leftarrow\leftarrow$ $^2\Pi_{3/2}$ (v=0) transition, on the grounds that the separation of the bands observed at room temperature and with rotational resolution was

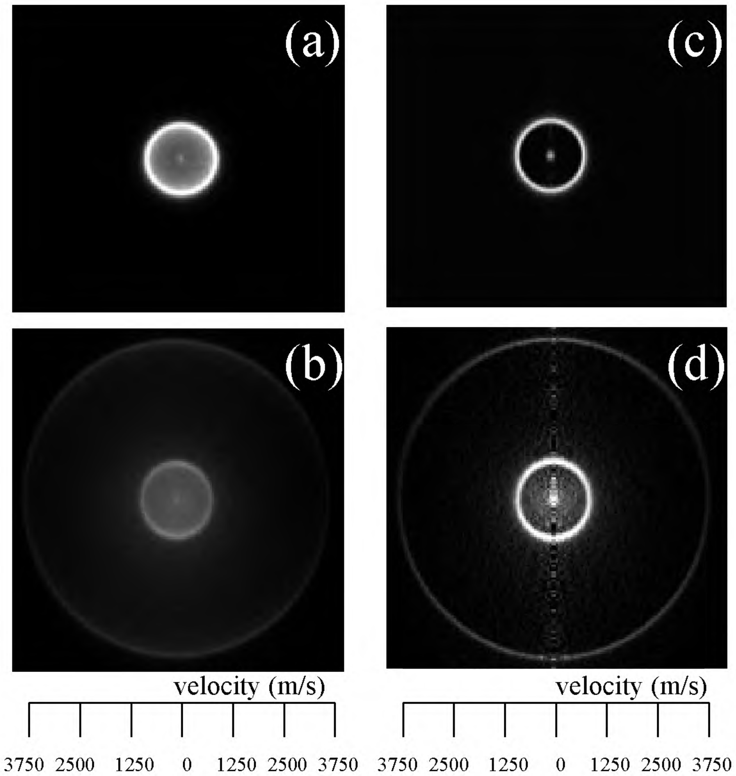

Figure 4.1: *Raw data images (a),(b) and Abel inverted images (c),(d) of* $O(^3P_2)$ *formed from the two photon dissociation of jet cooled NO. (a),(c) upper panel, shows the image for excitation at 72643* cm^{-1}*, showing an almost symmetric inner ring at a speed of 840 m/s, corresponding to formation of* $N(^2D)$ *as a co-product. (b),(d) lower panel, is for excitation at 72616* cm^{-1}*, and what can be seen in addition is an asymmetric ring peaking in the direction of the excitation laser polarization (vertical in the Figure) at a speed of 3760 m/s, and corresponding to formation of* $N(^4S)$*.*

that expected from the separation of the two spin orbit states in $^2\Pi$ NO. In our case we concur with the assignment of Gadd *et al.* [4], as under the present expansion conditions very little NO is retained in the upper $^2\Pi_{3/2}$ state as evidenced from a 1 + 1 multiphoton ionisation spectrum of NO near 226 nm. Both previous studies were able to achieve rotational resolved structure on the observed bands. In the present case it appears that the high laser intensity needed for the efficient production of fragment atoms causes marked broadening of the transitions (which, owing to the cooling in the expansion, can only arise from low J).

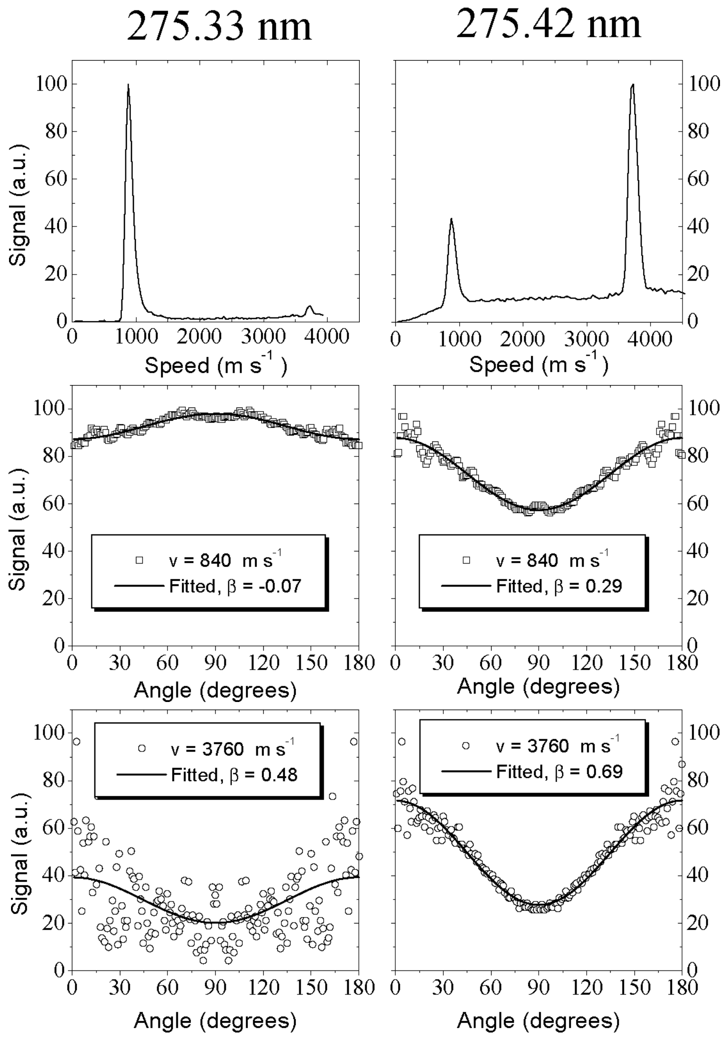

Figure 4.2: *Angle integrated speed distributions (upper panel) and angular distributions (middle and lower panels) for the images shown in Figures 4.1(c) and 4.1(d) (left and right hand boxes respectively). Angular distributions are fitted to the expression* $I(\theta) = 1 + \beta P_2(\cos\theta)$, *and are shown for the slow and fast fragments associated with* $N(^2D)$ *and* $N(^4S)$ *in the centre and lower panels respectively.*

One of the noticeable features of the previous studies of both the N(^{2}D) dissociation yields [4, 6] and the REMPI spectra [3] in this wavenumber region has been the failure to observe the ndπ^+ components of the Rydberg states, expected to mix with the corresponding ndσ component and to lie some 10-20 cm^{-1} lower in energy than the ndπ^- state [5, 6]. Predissociation of the ndπ^+ states is expected to take place at rates faster than those for the ndπ^- states [3], and it has been suggested that the dissociation products could be the previously unobserved channel

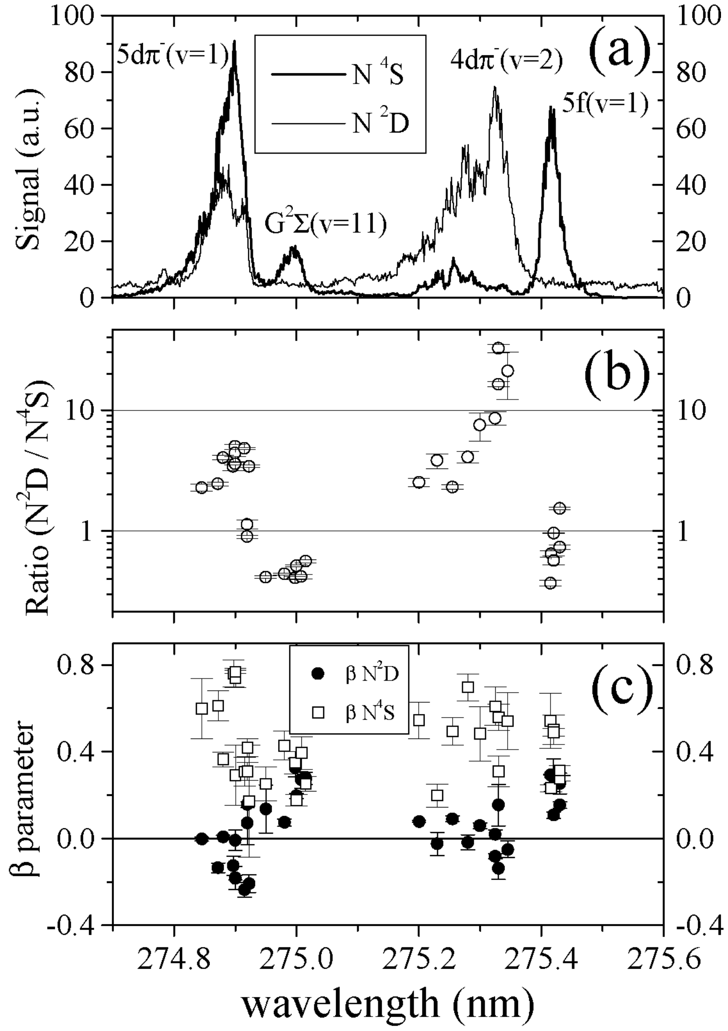

Figure 4.3: *(a) Excitation spectra of the N(^{2}D) and N(^{4}S) b) channels of the two photon dissociation of NO. The REMPI laser was fixed in wavelength at the maximum of the O($^3P_2$) two photon transition, thus preferentially ionizing those fragments with zero velocity components along the laser propagation axis. In (b) the ratio of N(^{2}D)/N(^{4}S) is plotted at discrete wavelengths in experiments in which the full range of product velocities was sampled, and the corresponding β values are plotted in (c).*

forming N(^{4}S) [4, 6]. Our observations of a marked N(^{4}S) peak at 72616 cm^{-1} some 20-30 cm^{-1} to the red of the 4dπ^- (v=2) peak would be consistent with this assignment, but to assign the corresponding N(^{4}S) feature at 72750 cm^{-1} as the corresponding 5dπ^+ (v=1) component would require either the nπ^- - nπ^+ splitting to have a stronger dependence than the n^{-3} variation theoretically expected [3] or for there to be perturbations in this spectrally congested region. We note that in this region transitions are expected to the G$^2\Sigma$ (v=11) valence state [2, 4], whose high wavenumber onset is at the small peak seen in the N(^{4}S) spectrum at 72730 cm^{-1}, and that transitions to the 5f(v=1) Rydberg state are expected to lie near 72660 cm^{-1} [2].

We now turn to the angular distributions. For a two photon process we expect that I(θ) should contain both $P_2(\cos\theta)$ and $P_4(\cos\theta)$ terms, but find to within our S/N ratio that the data are described satisfactorily by omitting the P_4 term and fitting to a produce a single β value. The gross conclusion from Figure 4.3(d) is that the N(^{2}D) is largely unaligned when its dissociation yield is high (i.e. on the peaks assigned to the 5dπ^- and 4dπ^- levels), and that the N(^{4}S) is more aligned at its peak values with β *ca.* 0.4. The differences in the β values for the two spectrally overlapping channels at wavenumbers above 72750 cm^{-1} would not be expected if dissociation took place from the same upper state crossed by two purely repulsive curves leading to N(^{4}S) and N(^{2}D), with β controlled by the lifetime of the common upper state. Instead it appears that distinct but overlapped states are excited in this region, each with a characteristic β parameter and dissociation channel propensity.

Simulations of the expected angular distributions were carried out for two photon Π-Π transitions with different proportions of Σ and Π intermediate states. Pratt *et al.* [3] have argued that the C$^2\Pi$ and D$^2\Sigma^+$ intermediate states should make approximately equal contributions to transitions to both π^- and π^+ components. We find that we can fit our data with single β parameters by appropriate choices of upper state lifetimes and relative contributions of the intermediate state. For example, for equal contributions of the C and D states and a lifetime of 8 ps (which would be appropriate for the structured transition to the 5dπ^- component) the simulation would be fitted well by β=0.4. Longer lifetimes or larger D$^2\Sigma^+$ contributions tend to smear the distributions more towards isotropy, and we also note that power broadening will do the same thing (we were unable to explore the effect of laser intensity because of the marked effect that it had on the signal magnitude). The observation of isotropy on the N(^{2}D) channel suggests that one or more of these factors has a dominant influence. We note that the mechanisms which lead to the N(^{2}D)+O(^{3}P$_2$) and N(^{4}S)+O(^{3}P$_2$) channels have been previously suggested as via the crossing of the nπ^- state by the B'$^2\Delta$ and of the nπ^+ state by the A'$^2\Sigma^+$ respectively [6]. Faster predissociation of the nπ^+ states therefore implies that interaction of these levels with the A'$^2\Sigma^+$ must take place efficiently despite the states being of different symmetries in the homonuclear limit [6].

What is clear from the data of Figure 4.3 is that the total yields of N(^{2}D) and N(^{4}S) integrated over the bands near 72643 and 72616 cm^{-1} are not equal, with N(^{2}D) dominating. If the initially populated states are the 4dπ^- and 4dπ^+ components respectively, and if we do not invoke any spin forbidden dissociation to give the unobserved N(^{4}S)+O(^{1}D) channel, then we can only conclude that the two photon excitation cross sections for the formation of the states which lead to the observed products are different. The observed products contain only the lowest but statistically most important spin orbit state of O(^{3}P), and differences in the partitioning of spin orbit excitation cannot be ruled out.

We finally describe the use of these monoenergetic fragments in studies of reaction stereodynamics. The major correlations that are measured in such studies are between pairs of the vectors **k** (the reactant relative velocity), **k'** (the product relative velocity) and **J'** (the product angular momentum, generally of a diatomic species). Under the conditions of laser intensity used by Umemoto *et al.* in the $N(^2D) + H_2$ reaction [12] (which were very similar to those used here) the atomic fragment will be essentially unaligned (ie, **k** is single valued in magnitude but isotropic in direction). However, vector correlations are measured in the laboratory frame, and for a diatomic co-reactant there is a direct mapping of the measured lab. frame velocity into the centre-of-mass scattering angle [14]. This will allow **(k,k')**, the differential cross section, to be determined (although for a bulk sample of H_2 its fast velocity will smear such information). The **(k',J')** correlation is independent of the alignment of the atomic reagent, and thus can also be found. Such measurements are currently underway in our laboratory.

Acknowledgments

The work in Nijmegen is part of the program of the Foundation Fundamental Research on Matter (FOM) and was made possible by financial support from The Netherlands Organization of Science (NWO). We are grateful to the British Council for a travel grant.

References

[1] E. Miescher, K.P. Huber, Int. Rev. Sci. Phys. Che. Ser. **3** , 37 (1976).
[2] E. Miescher, F. Alberti, J. Phys. Chem. Ref. Data **5**, 309 (1976).
[3] S.T. Pratt, Ch. Jungen, E. Meischer, J. Chem. Phys. **90**, 5971 (1989).
[4] G.E. Gadd, L.E. Jusinski, T.G. Slanger, J. Chem. Phys. **91**, 3378 (1989).
[5] D. Gauyacq, A.L. Roche, M. Seaver, S.D. Colson, W.A. Chupka, Mol. Phys. **71**, 1311 (1990).
[6] H. Umemoto and K. Matsumoto, J. Chem. Soc. Faraday Trans. **92**, 1315 (1996).
[7] B.L.G. Bakker, A.T.J.B. Eppink, D.H. Parker,M.L. Costen, G. Hancock, G.A.D. Ritchie, Chem. Phys. Lett. **283**, 319 (1998).
[8] A.T.J.B. Eppink, D.H. Parker, Rev. Sci. Instrum. **68** , 3477 (1997).
[9] A.J. Orr-Ewing and R.N. Zare, in *Chemical Dynamics of Small Free Radicals* eds. K. Liu and A.L. Wagner (World Scientific, Singapore, 1995).
[10] M. Brouard and J.P. Simons, in: *Chemical Dynamics of Small Free Radicals* eds. K. Liu and A.L. Wagner (World Scientific, Singapore, 1995).
[11] A.J. Orr-Ewing, J. Chem. Soc. Faraday Trans. **92** , 881 (1996).
[12] H. Umemoto, T. Asai and Y. Kimura, J. Chem. Phys. **106**, 4985 (1997).
[13] D.H. Parker and A.T.J.B. Eppink, J. Chem. Phys. **107**, 2357 (1997).
[14] N.E. Schafer, A.J. Orr-Ewing, W.R. Simpson, H. Xu, R.N. Zare, Chem. Phys. Lett. **212** , 155 (1993).

Chapter 5

Photodissociation dynamics of $^{13}C^{16}O$ excited by 193 nm light

Abstract

The two-photon dissociation dynamics of $^{13}C^{16}O$ is studied using a tunable ArF excimer laser and the velocity map imaging technique. C(^{1}D) atoms formed are detected via (1+1) REMPI (Resonance Enhanced Multi Photon Ionization). The measured C(^{1}D) yield spectrum is assigned to the $a^3\Pi(v=2)\leftarrow X\ ^1\Sigma^+(v=0)$ transition. Images containing velocity and angular distribution information are measured for the Q(1), R(0) and R(1) lines. The dissociation energy of $^{13}C^{16}O$ is confirmed to be 11.09±0.02 eV. Dissociation takes place after one-photon excitation of the $a^3\Pi_1(v=2)$ state via a $\Delta\Omega=0$ (parallel) transition. A suggested dissociation process is the predissociation of a $^3\Pi_1$ Rydberg state on a 16±5 ps time scale.

5.1 Introduction

Carbon monoxide is, after H_2, the most abundant molecule in the universe. Because H_2 is not directly observable, many astrophysical studies monitor CO to map molecular abundance in interstellar space. CO, however, has a complex photolysis wavelength dependence on exposure to ultraviolet light that needs to be better understood. The photodissociation dynamics of CO has been the subject of extensive theoretical [1, 2, 3, 4, 5] and experimental [5, 6, 7, 8, 9, 10, 11, 12, 13, 14, 15, 16, 17, 18] research. Most investigations deal with the photoexcitation of CO to highly excited Rydberg states that subsequently decay via predissociation [5, 6, 7, 8, 9, 10, 11, 12, 13]. Only a few studies have recorded the photofragments of the dissociating CO. Most experimental studies, including the present study, employed an ArF excimer laser, because the spin forbidden $a^3\Pi(v=2) \leftarrow X^1\Sigma^+(v=0)$ transition known as the Cameron band [19] is resonant within the 193 laser wavelength. The dissociation limits of CO, $C(^3P)+O(^3P)$ at 11.09 eV and $C(^1D)+O(^3P)$ at 12.35 eV are shown in Fig. 5.1. Both limits are exceeded by two 193 nm photons of 6.4 eV each. Because the ionization potential of CO is 14.01 eV, the photodynamics at the two-photon level is determined only by dissociation; via a singlet channel towards the $C(^3P)+O(^3P)$ limit, or via a triplet channel into the $C(^1D)+O(^3P)$ limit. By coincidence, the strong C atom ($2p3s\ ^1P) \leftarrow (2p^2\ ^1D$) transition is also resonant with the 193 nm light [20]. Through this path $C(^1D)$ can be ionized, the $C(^3P)$ and $O(^3P)$ neutral atoms will be undetected.

Hill *et al.* [14] measured the kinetic energy of C atoms after the two-photon dissociation of CO with 193 nm produced by a tunable ArF excimer laser. Forch and Merrow [15, 16] observed LIF from $O(^3P_J)$ using a broadband ArF laser. Both groups could not determine from what specific quantum state the dissociation occurred, but concluded the dissociation was a two-photon process.

Ebata and co-workers [17, 18] prepared Rydberg states between the second dissociation limit and the ionization potential. They excited CO from $(3s\sigma)B^1\Sigma^+(v=0)$, which was populated via two-photon pumping from the $X^1\Sigma^+(v=0)$. A third laser probed the fragments via REMPI, observing only $C(^3P)$ fragments in the first [17] study and $C(^3P)$, $C(^1D)$ and $O(^3P)$ fragments in the second [18] study, where the photofragment yield spectrum was measured for predissociation processes of the $(3d\pi)L'^1\Pi(v=1)$ and $(4p\pi)L^1\Pi(v=0)$ Rydberg states of CO lying at approximately 12.93 eV. This is in the same energy region as two ArF laser photons ($\approx$12.8 eV). Ebata and co-workers concluded that the singlet and triplet channels compete with each other with a similar decay rate. However, they could not distinguish whether the upper dissociative state had Π or Σ character.

In the present work, a combination of a line-narrowed tunable ArF excimer laser and the technique velocity map imaging [21, 22] is used. The mixture of narrow-band tunable output and broad-band background of the tunable ArF laser allows for both the preparation of the initial quantum state and the REMPI detection of $C(^1D)$ atoms. The velocity map imaging technique measures the kinetic energy and angular distributions of the fragments simultaneously. Similar studies of the decay dynamics of Rydberg states of NO [23, 24] have been reported previously.

The N-photon dissociation angular distribution $I(\theta)$ is given by [25, 26]:

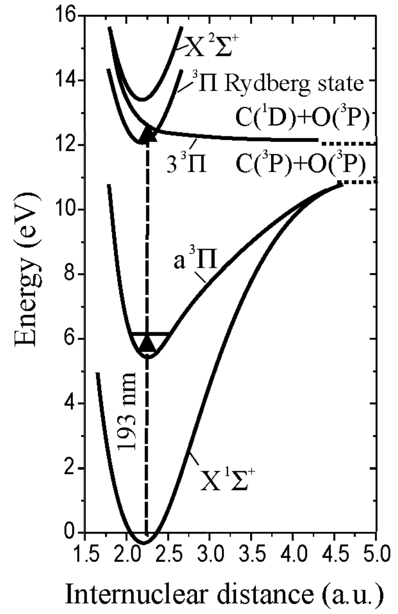

Figure 5.1: *Schematic potential energy curves of CO of interest in this study.*

$$I(\theta) \propto 1 + \sum_{n=2,4,..}^{n=N} \beta_n^N \cdot P_n(\cos\theta) \tag{5.1}$$

where $P_n(\theta)$ are n^{th} order Legendre polynomials ,β_n^N are the anisotropy parameters and where θ is the angle between the laser polarization and the particle velocity vector. Different pure photon transitions results in different extreme values of β_n^N. For a two-step process two parallel transitions result in β_2^2=20/7 and β_4^2=8/7, two perpendicular transitions gives β_2^2=-10/7 and β_4^2=3/7, and a parallel-perpendicular combination can be described by β_2^2=5/7 and β_4^2=-12/7.

For a one-photon transition, the limiting values of β_2^1 in (5.1)are -1 or 2, corresponding to a purely perpendicular or parallel transition, respectively. A possible reason for a non-extreme anisotropy parameter $-1< \beta_2^1 <2$ is the overlap of a parallel and perpendicular transition. Another possible reason is the diminishment of anisotropy due to rotation. If, in the case of a one-photon transition, the lifetime τ of the excited state is similar to the parent molecule angular rotational period T and the according rotational angular frequency ω=1/T of that state, the anisotropy parameter is given by the formula [27]:

$$\beta_2^1(\tau) = \beta_{max} \cdot \frac{\omega^2\tau^2 + 1}{4\omega^2\tau^2 + 1} \tag{5.2}$$

where β_{max} is -1 or 2, corresponding to an initially pure perpendicular or parallel transition, respectively. Measurement of β_n^N for each channel thus provides information on the symmetry of the electronic states involved in the absorption process or their lifetimes with respect to rotation.

5.2 Experiment

A detailed description of the velocity mapping apparatus has been reported elsewhere [21] so only a brief summary of the experimental details will be given here. A 10% CO/He mixture is passed through a pulsed nozzle and skimmer, forming a molecular beam that is directed down the axis of a time-of-flight (TOF) mass spectrometer and crossed at right angles by the line-narrowed ($\Delta\nu \sim 0.5$ cm^{-1}) ArF excimer laser. The 193 nm light (15 ns pulse width, 25 mJ per pulse, $\sim 5 \times 10^{16}$ photons) was focused with a 35 cm lens on to the molecular beam resulting in an intensity of $\sim 5\text{x}10^{10}$W/cm^2. The line-narrowed scanning range is 51600-51800 cm^{-1} and under the best conditions, a broad-band component with integrated intensity at least equal to that of the line-narrowed accompanies the narrow-band output. The laser scanning is performed by tuning the grating mechanically, providing a wavelength accuracy of ~ 0.5 cm^{-1}.

A series of dichroic mirrors used to direct the 193 nm beam serve also to attenuate the horizontal component of the initially unpolarized light. This results in >99% vertical polarization at the interaction zone. The formed ions were extracted from the ionization region through a grounded time-of-flight tube and crushed onto a two-dimensional microchannel plate / phosphor screen detector read by a CCD camera. Mass selectivity was achieved by pulsing on the gain of the detector as the ions arrive. Typically, 25,000 laser shots were used to produce the final raw image that was then inverted using an inverse (2D-3D) Abel transformation. The laser wavelength and the velocity of the product atoms were calibrated using the properties of the193 nm photodissociation process of O_2 [28].

The broadband background light of the ArF laser ionizes nascent C(^{1}D) atoms via the strong (2p3s)^{1}P$\leftarrow$(2p^2)^{1}D transition at 51789.2 cm^{-1} as reported by Versluis and Meijer [20]. This process results in a huge apparatus background of ^{12}C ions due to the dissociation of diffusion pump oil. The fragmentation signal of CO is a two-photon process, but the background is a one-photon process. The background ^{12}C signal saturates the detector and causes space-charge problems. However, on the mass of the isotope ^{13}C, which has a 1,1 % natural abundance, the signal to background ratio is acceptable. The narrow-band component is tuned to the ^{13}CO transition and the broadband component is used to ionize product ^{13}C(^{1}D) atoms. The spatial information of the detector is integrated for all ^{13}C events in an ion yield spectrum.

5.3 Results and discussion

5.3.1 Spectral behavior

A ^{13}C ion yield spectrum is shown in Fig. 5.2 along with the ^{13}CO a$^3\Pi$(v=2) $\leftarrow$ X $^1\Sigma^+$(v=0) transition assignments. The excimer laser was scanned over the total ArF gain profile, but only this small tuning region showed ^{13}C ions. The spin-forbidden a$^3\Pi$(v=2)$\leftarrow$X$^1\Sigma^+$(v=0) transition becomes weakly allowed due to mixing of the a$^3\Pi$ state with the A$^1\Pi$ state, making the transition similar to the one-photon allowed $^1\Pi \leftarrow ^1\Sigma$ transition. Only transitions to the Ω=1 component of the Ω=0,1,2 triplet are allowed for low J. The a$^3\Pi$(v=2)$\leftarrow$X$^1\Sigma^+$(v=0) transition is well known for ^{12}CO as the Cameron band [19], but for ^{13}CO the P, Q and R lines have not been tabulated. However, they can easily be calculated using the known molecular constants [29] of ^{12}CO after being calculated with the known isotope scaling expression [29]. A similar method was used by Berden *et al.* [30] for the $k^3\Pi$ state of ^{12}CO and ^{13}CO. Calculated P, Q and R branches are presented in Fig. 5.2 and show good agreement with the measured branches. The spectrum shows a stronger Q branch and weak P and R branches. This is similar behavior as seen in the $C(^1D)$ yield spectra of Okazaki *et al.* [18].

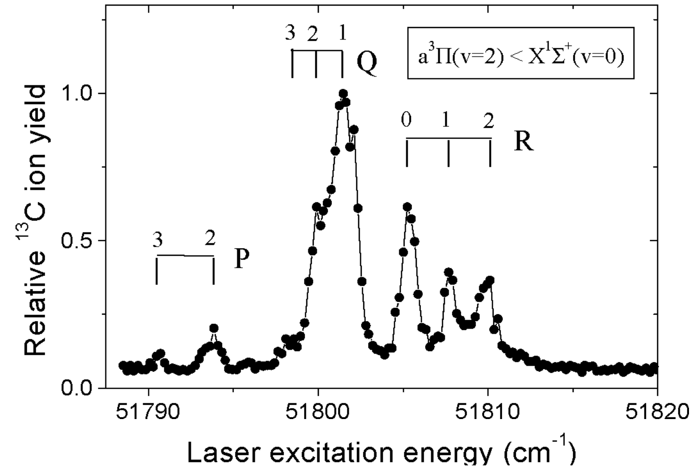

Figure 5.2: *Yield spectrum of $^{13}C^+$ taken with a tunable ArF excimer laser. The lines are assigned to the different rotational branches of the $a^3\Pi(v=2)\leftarrow X^1\Sigma^+(v=0)$ transitions in $^{13}C^{16}O$.*

5.3.2 Kinetic behavior

Images obtained when setting the laser on the lines Q(1), R(0) and R(1) all look similar, therefore only the Q(1) image is presented in Fig. 5.3. The image shows only one ring. The raw data image is presented in fig. 5.3(a) and the Abel-inverted image is shown in fig. 5.3(b), and the corresponding kinetic energy distribution is presented in Fig. 5.4. The kinetic energy release of 0.27 eV corresponds to the two-photon dissociation of ^{13}CO towards the second dissociation limit. This agrees well with the work of Hill *et al.* [14] who saw a peak at approx. 0.2 eV for ^{12}CO. They ascribed this signal to two-photon dissociation to the $C(^1D)$ limit. The known dissociation limit of ^{12}CO is D_0=11.09 eV [29] and the energy difference between $C(^3P)$ and $C(^1D)$ is 1.26 eV [31]. The dissociation energy for ^{13}CO is of course similar and calculating this value from the experimental data in Fig. 5.4 gives an experimental value of 11.09±0.02 eV.

The observed peak could also arise from a three-photon dissociation towards the excited dissociation limit of electronically excited $C(2p3s\ ^1P^0)+O(^3P)$, resulting in a kinetic energy of 0.27 eV. Electronically excited C atoms should be easily photoionized to C^+ ions, which are not observed in the experiment. The other possible excited state dissociation limit $C(2p3s\ ^3P^0)+O(^3P)$ at 0.38 eV could also be expected, because dissociation of a highly excited state tends to produce all excited fragments possible, as seen in other experiments [32]. This would result in an image with two rings, but in this experiment only one ring is seen, so dissociation of CO at a two-photon level is more probable. The CO^+ signal was also checked but revealed no wavelength dependent

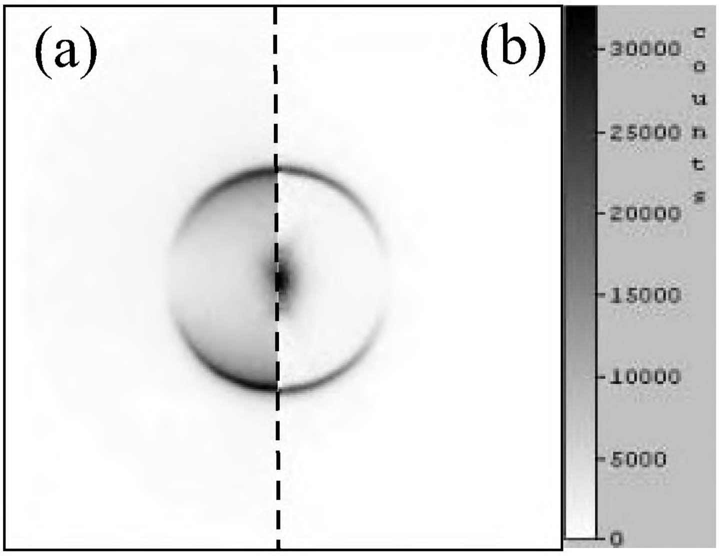

Figure 5.3: *Images of $^{13}C(^1D)$ products after two-photon dissociation of $^{13}C^{16}O$ via the Q(1) line of the $a^3\Pi(v=2)\leftarrow X^1\Sigma^+(v=0)$ transition (a) Raw image (b) Abel inverted image. The dotted line shows the direction of the laser polarization.*

signal, confirming the observation by Hill *et al.* [14]. They concluded that three-photon excitation did not occur. Our results supports the conclusions made by Hill *et al.* [14] and Forch and Merrow [15, 16] that the dissociation process is a two-photon one.

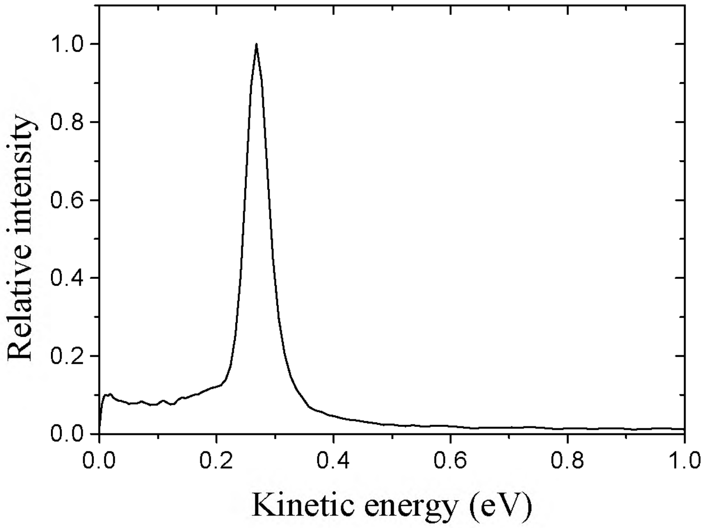

Figure 5.4: *Kinetic energy distribution of ^{13}C atoms taken from image in Fig. 5.3.*

5.3.3 Angular distributions

The angular distributions following excitation of the Q(1), R(0) and R(1) branches are shown in Fig. 5.5(a), 5.5(b) and 5.5(c), respectively. The measured angular distributions are fitted to expression (5.1) giving averaged β and γ values presented in Fig. 5.5 . These values indicate that the two-photon process consists of nearly zero perpendicular character and major parallel character. However, the value of β exceeds the maximum value of 5/7 and γ is nearly 0 so the measured angular distribution can also be described by a one-photon expression using only the β in formula ((5.1). Indeed, when fit using formula ((5.1) with and without γ the value of β only differs within 0.005. The first photon transition, $a^3\Pi(v=2)\leftarrow X^1\Sigma^+(v=0)$, is perpendicular ($\Delta\Omega=1$), but the $a^3\Pi(v=2)$ lifetime is $\approx$3.6 ms [33] and the rotational period T of the main occupied rotational state J=1 is T$\approx$60 ps. A long-lived state produced by a bound-bound transition is in general not likely to introduce significant alignment effects [24]. This means that only the photon transition starting from the $a^3\Pi(v=2)$ state determines the angular distributions of the fragments. Note also that population of the $a^3\Pi$ state via a Q or R transition does not change the final anisotropy parameters within the uncertainty of the experiment. Considering the uncertainty in the measured anisotropy values, no significance is assigned to the difference in them for the various rotational branches.

Several explanations are possible for the observed non-maximal β value. It should be noted that the wide-band component of the excimer laser can excite any bound-bound transition within the $\Delta E\sim 200\text{cm}^{-1}$ gain profile. A mixture of perpendicular and parallel character could result. Saturation due to the high laser flux could also lower the anisotropy. Within the limited dynamic range of the signal no changes in β were observed when lowering the laser flux.

One proposed explanation for the non-extreme measured β is the diminishing of anisotropy due to rotation of the excited state. This has been seen before in similar experiments [23, 24]. For CO these excited states are triplet Rydberg states that lie in the energy region of the two-photon absorption at $\nu_0\approx 103600\ \text{cm}^{-1}$. Starting in the Hund's case (a) state $a^3\Pi_1$ the measured β=1.8 would imply a parallel transition ($\Delta\Omega=0$) ending in a $^3\Pi_1$ or $^3\Sigma_1$ state. This means the excited state has mainly $\Omega=1$ character and the Σ or Π property is less sure. At the two-photon energy level only $^3\Pi$ Rydberg states are known [34]. These states can predissociate via the $3^3\Pi$ and $4^3\Pi$ repulsive states [1] as denoted in Fig. 5.1. Eidelsberg and Rostas [7] identified the H' $3s\sigma^3\Pi(v=3)$ state at $\nu_0\approx 103988\ \text{cm}^{-1}$ and the W'$3s\sigma^3\Pi(v=2)$ state at ν_0=102210 cm^{-1}. These are^{13}CO $^3\Pi$ Rydberg states that converge to the ionic state $A^2\Pi$ (v). Using the molecular constants for the $c^3\Pi$ state measured by Wan *et al.* [35] and the isotope scaling expression [29], the transition energies for $c^3\Pi(v=5)$ are $\nu_0\approx 102222\ \text{cm}^{-1}$ and for $c^3\Pi(v=6)$, $\nu_0\approx 104083\ \text{cm}^{-1}$. The closest-lying state is H' and it has a estimated lifetime of 3$\pm$10 ps and a rotational constant B$\approx$1.3 cm^{-1} so using the main rotational occupied state J=1 and formula ((5.2) plus the measured averaged β=1.793, this results in an experimental lifetime τ of 16$\pm$5 ps. The angular distribution derived lifetime determined in this experiment τ=16$\pm$5 ps agree well with the one estimated by Eidelsberg *et al.* [7] τ=3$\pm$10 ps . Hill *et al.* [14] calculated an approximate photoionization lifetime of 10 ps. They saw no $^{12}CO^+$ and therefore concluded that the predissociation lifetime should be at least on a ps time scale and this is also seen in this experiment.

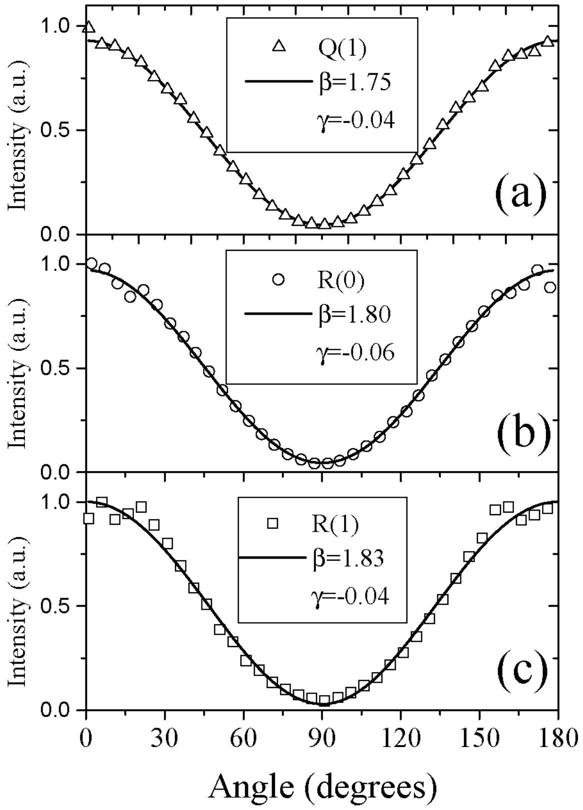

Figure 5.5: *Angular distributions and fitted curves corresponding to different lines of the* $a^3\Pi(v=2)\leftarrow X^1\Sigma^+(v=0)$ *transitions in* $^{13}C^{16}O$. *The angular parameters* β *and* γ *have a* 1σ *error of 0.1. (a) Q(1). (b) R(0). (c) R(1).*

5.4 Conclusions

The two-photon dissociation dynamics of $^{13}C^{16}O$ is measured using a tunable ArF excimer laser. The measured $^{13}C(^1D)$ yield spectrum is assigned to the $a^3\Pi(v=2)\leftarrow X^1\Sigma^+(v=0)$ transition. The C^+ angular distribution shows that a $\Delta\Omega=0$ transition takes place from the intermediate state. We suggest the following scheme: the second 193 photon excites the molecule towards an $^3\Pi_1$ Rydberg states that predissociate via the $3^3\Pi$ or $4^3\Pi$ state in an estimated time of 16±5 ps.

Acknowledgments

This work is part of a research program supported by FOM and NWO. The authors thank M.C. van Beek, N.J. Dam and J.J. ter Meulen for help and use of the tunable excimer laser and also R. Bethlem and G. Berden for help on the $^{13}C^{16}O$ spectrum. The authors also thank C. Sikkens and C. Timmer for technical support.

References

[1] S.V. O'Neil and H.F. Schaefer III, J. Chem. Phys. **53**, 3994 (1970).
[2] D.M. Cooper and S.R. Langhoff, J. Chem. Phys. **74**, 1200 (1981).
[3] D.L. Cooper and K. Kirby, Chem. Phys. Lett. **152**, 393 (1988).
[4] W. -ÜL. Tchang-Brillet, P.S. Julienne, J.M. Robbe, C. Letzelter and F. Rostas, J. Chem. Phys. **96** 6735 (1992).
[5] C. Letzelter, M. Eidelsberg, F. Rostas, J. Breton and B. Thieblemont, Chem. Phys. **114** 273 (1987).
[6] M. Eidelsberg, J.J. Benayoun, Y. Viala and F. Rostas, Astron. Astrophys. , Suppl. Ser. **90**, 231 (1991).
[7] M. Eidelsberg and F. Rostas, Astron. Astrophys. **235** 472 (1990).
[8] M. Drabbels, J. Heinze, J.J. ter Meulen and W.L. Meerts, J. Chem. Phys. **99** 5701 (1993).
[9] W. Ubachs, K.S.E. Eikema, P.F. Levelt, W. Hogervorst, M. Drabbels, W.L. Meerts and J. J. ter Meulen, Astrophys. J. **427**, L55 (1994).
[10] K.S.E. Eikema, W. Hogervorst and W. Ubachs, Chem. Phys. **181**, 217 (1994).
[11] M. Komatsu, T. Ebata and N. Mikami, J. Chem. Phys. **99**, 9350 (1993).
[12] M. Komatsu, T. Ebata, T. Maeyama and N. Mikami, J. Chem. Phys. **103**, 2420 (1995).
[13] A. Mellinger, C.R. Vidal and C. Jungen, J. Chem. Phys. **104**, 8913 (1996).
[14] W.T. Hill III, B.P. Turner, H. Lefebvre-Brion, S. Yang and J. Zhu, J. Chem. Phys. **92**, 4272 (1990).
[15] C.N. Merrow and B.E. Forch, J. Chem. Phys. **93**, 4791 (1990).
[16] B.E. Forch and C.N. Merrow, J. Chem. Phys. **95**, 3252 (1991).
[17] T. Ebata, T. Sutani and N. Mikami, Chem. Phys. Lett. **240**, 357 (1995) .
[18] A. Okazaki, T. Ebata, T. Sutani and N. Mikami, J. Chem. Phys. **108** 1765 (1998).
[19] R.W. Field, S.G. Tilford, R.A. Howard and J.D. Simmons, J. Mol. Spectrosc. **44**, 347 (1972).
[20] M. Versluis and G. Meijer, J. Chem. Phys. **96**, 3350 (1992) .
[21] A.T.J.B Eppink and D.H. Parker, Rev. Sci. Instrum. **68**, 3477 (1998).
[22] D. W. Chandler and D. H. Parker, Adv. Photochem. **25**, 56 (1999).
[23] B.L.G. Bakker, A.T.J.B. Eppink, D.H. Parker, M.L. Costen, G. Hancock, G.A.D. Ritchie, Chem. Phys. Lett. **283**, 319 (1998).
[24] B.L.G. Bakker, D.H. Parker, G. Hancock, G.A.D. Ritchie, Chem. Phys. Lett. **294**, 565 (1998).
[25] R.N. Zare, Mol. Photochem. **4**, 1 (1972).
[26] K. Chen and E.S. Yeung, J. Chem. Phys. **72**, 4723 (1980).
[27] C. Jonah, J. Chem. Phys. **55**, 1915 (1971).
[28] B.L.G. Bakker and D.H. Parker, J. Chem. Phys. **112**, 4037 (2000).
[29] G. Herzberg, *Molecular Spectra and Molecular Structure, Vol. 1: Spectra of Diatomic Molecules*, (Van Nostrand, New York, 1950).
[30] G. Berden, R.T. Jongma, D. van der Zande and G. Meijer, J. Chem. Phys. **107**, 8303(1997).
[31] C.E. Moore, *Atomic energy levels Vol. I*, (Circular of the National Bureau of Standards 467, Washington, 1949).
[32] D.H. Parker and A.T.J.B. Eppink, J. Chem. Phys. **107**, 2357 (1997).
[33] R.T. Jongma, G. Berden and G. Meijer, J. Chem. Phys. **107**, 7034 (1997).

[34] J. Baker, J.L. Lemaire, S. Couris, A. Vient, D. Malmasson and F. Rostas, Chem. Phys. **178**, 569 (1993).
[35] R.N. Wan and H. Langhoff, Z. Phys. D **21**, 245 (1991) .

Chapter 6

Photophysics of O_2 excited by tunable laser radiation around 193 nm

Abstract

The photodissociation/ionization dynamics of O_2 around 193 nm have been studied using a narrow-band tunable ArF excimer laser and the velocity map imaging technique. Angular and kinetic energy distributions of the product O^+ ions and $O(^3P_2)$ atoms are recorded and analyzed. The production of $O(^3P_2)$ atoms is resonance enhanced on the one-photon level by the $B^3\Sigma_u^-(v=4)$ state, which is part of the $B^3\Sigma_u^- \leftarrow X^3\Sigma_g^-$ Schumann-Runge bands. Angular distribution measurements for individual rotational levels of the B state yield values for the anisotropy parameter, β_{SR}, which are in good agreement with the values predicted by independent measurements of predissociation lifetimes from spectral linewidths. An average value of $\beta=0.48$ is found for the underlying Herzberg continuum at 193 nm. O_2^+ production is enhanced on the two-photon level via members of the $ns\sigma_g(n-1)d\pi_g\ ^1\Sigma_g^+$ Rydberg series terminating at higher vibrational levels of the ion. The high Rydberg states autoionize into the O_2^+ $X^2\Pi_g$ ground state or absorb one more photon and then autoionize into the $A^2\Pi_u$ and $b^4\Sigma_u^-$ states of O_2^+, which subsequently fluoresce. Production of O^+ from one and two-photon dissociation of the O_2^+ formed after two-photon absorption is also observed and characterized.

6.1 Introduction

Molecular oxygen plays a central role in many research fields including atmospheric physics, combustion analysis, and in fundamental studies of the quantum mechanics of small molecules. In this article we describe the photophysics of molecular oxygen excited by tunable radiation around 193 nm, a wavelength falling within the Schumann-Runge bands [1], the dominant photoabsorption system in the Earth's atmosphere. Molecular oxygen dissociates on absorbing this vacuum ultraviolet radiation. The speed and angular distribution of the atomic products are determined here by the velocity map imaging technique [2]. Predissociation lifetimes of the $B^3\Sigma_u^-$ excited electronic state and those of the underlying Herzberg continuum [3] can be determined from the angular distribution anisotropy. These values are compared with previously measured rates from spectroscopic linewidths [4].

A narrow-band tunable ArF laser generates the radiation used in this study. When this type of laser is focused it is easily capable of driving not only one-photon absorption but also higher order multiphoton absorption and ionization processes. Neutral and ionic products are formed, their analysis yields information on the high-energy states of O_2 and O_2^+. A rich array of interesting and unexpected photodissociation / ionization steps are found to take place following multiphoton excitation, many of which provide new insight into the basic photophysics of molecular oxygen. Furthermore, these newly identified mechanisms can be of practical importance because tunable ArF lasers are very often employed in diagnostics of combustion processes [5] under conditions where the same multi-photon events can take place.

Competition between dissociation and ionization during multiphoton absorption is a topic of basic interest in itself in laser ionization studies. Most relevant to this work, Hill and coworkers [6] have studied the competition between the ionization and fragmentation channels in O_2 following excitation by a focused, broad-band ArF laser using relatively low-resolution time-of-flight detection of O^+. Our higher resolution velocity mapping technique, supplemented by detection of nascent $O(^3P_2)$ atoms, leads us to a different interpretation of molecular oxygen photophysics in this wavelength region. These interpretations become much more straightforward when using tunable narrowband instead of broadband radiation.

Velocity map imaging has proven to be a powerful method for investigation of photo-dynamical processes in molecules [2]. The technique is ideally suited for simple diatomic molecules such as O_2 because the large vibrational spacing and limited number of possible atomic product states results in a unique kinetic energy release (KER) for each final quantum state channel. Besides providing the product quantum state distributions from the kinetic energy distribution, the angular distributions of the fragments are also measured, allowing in many cases an enhanced discrimination between the different decay channels. For a rapid one-photon dissociation the product angular distributions $I(\theta)$ is given by the expression [7]:

$$I(\theta) \propto 1 + \beta P_2(\cos\theta) \tag{6.1}$$

where θ is the angle between the laser polarization and the velocity vector of the particles and P_2 is the second-order Legendre polynomial. The anisotropy parameter β ranges from limiting values -1 to 2, corresponding to a perpendicular ($\Pi \leftrightarrow \Sigma$) and parallel ($\Sigma \leftrightarrow \Sigma$) transition, respectively. If the lifetime τ of the excited state is similar to the parent molecule angular rotational period T of that state, the anisotropy parameter is given by the formula [8]:

$$\beta_{\|}(\tau) = 2 \cdot \frac{(\tau/T)^2+1}{4(\tau/T)^2+1} \tag{6.2}$$

for a parallel transition and

$$\beta_{\perp}(\tau) = -1 \cdot \frac{(\tau/T)^2+1}{4(\tau/T)^2+1} \tag{6.3}$$

for a perpendicular transition. The slow dissociation limiting values for these anisotropy parameters are $\beta_{\|} = 0.5$ and $\beta\perp = -0.25$. Measurement of β for each channel thus provides information on the symmetry of the electronic states involved in the absorption process and their lifetimes with respect to rotation.

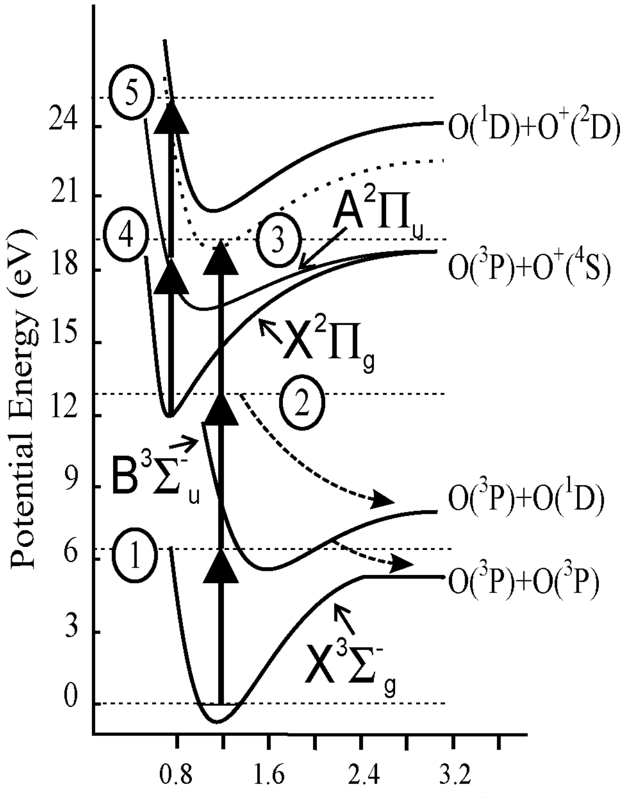

Figure 6.1: *Schematic potential energy curves for O_2 and O_2^+.*

Shown schematically in Figure 6.1 are the O_2 potential energy curves most relevant to this study. The bond energy of the ground electronic state, $X^3\Sigma_g^-$, is 5.115 eV and corresponds to the asymptotic limit of two $O(^3P)$ atoms. In the ultraviolet region of the O_2 spectrum extremely weak and sharp absorption from the $X^3\Sigma_g^+$ ground electronic state to the three electronically excited Herzberg states ($A^3\Sigma_u^+$, $A'^3\Delta_g$, and $c^1\Sigma_u^-$) take place which change over at 242 nm to the Herzberg continuum (242 - 180 nm) [3]. Although optically forbidden, photoabsorption / dissociation of O_2 due to the Herzberg continuum is the primary source of O(^{3}P) atoms in the stratosphere [9]. Deeper into the UV region the strong but pre-dissociated bands of the Schumann-Runge system (205 -130 nm) arise from the optically allowed $B^3\Sigma_u^- \leftarrow X^3\Sigma_g^+$ transition. They change over to a continuum below 175 nm corresponding to the second dissociation limit, O(^{3}P)+O(^{1}D) at 7.08 eV. Predissociation of bound levels of the $B^3\Sigma_u^-$ state, primarily by the $^5\Pi$ state, takes place resulting in the production of two O(^{3}P) atoms.

At higher energies in the O_2 spectrum a series of optically-allowed mixed valence-Rydberg *ungerade* states converging on the O_2^+ $X^2\Pi_u$ ground state (Ionization Potential = I.P. = 12.08 eV) are observed [10]. Several *gerade* Rydberg series [11] converging on the ground state of O_2^+ have been characterized using two-photon resonance enhanced multiphoton ionization, (2+1) REMPI. Mixing of those molecular Rydberg states with repulsive valence states can lead to rapid predissociation. The possible dissociation limits O(^{3}P)+O(^{3}P), O(^{1}D)+O(^{3}P), O(^{1}D)+O(^{1}D), and O(^{1}S)+O(^{3}P) fragments all lie within the energy sum of two ArF laser photons. Because this energy sum also exceeds the ionization potential of O_2, two-photon absorption can lead via direct ionization to the formation of ground state $X^2\Pi_u$ O_2^+(v^+=0,1,2,3). The ion has a dissociation energy of 6.66 eV, slightly higher than the 6.4 eV photon energy, thus all vibrational levels of O_2^+ $X^2\Pi_g$ higher than v^+=0 can be photodissociated, leading to $O^+(^4S)$+O(^{3}P) products (18.733 eV limit). Absorption of two ArF laser photons by O_2^+ can also take place as shown in this study, exciting the $X^2\Pi_u$ v^+=0 level to 24.90 eV which lies above the first five (O^++ O) dissociation limits (18.733, 20.700, 22.937, 23.057, 24.025 eV). One possibility, dissociation to the $O^+(^2P)$+O(^{1}D) limit at 24.025 eV, is shown in Figure 6.1. In summary, O^+ production mechanisms shown in Figure 6.1 include one and two-photon dissociation of O_2^+, while O(^{3}P) atoms can be formed after the absorption of one or more photons. Numerous other mechanisms could lead to O^+ formation including ion-pair formation, or non-resonant three-photon ionization of O atoms as suggested by Yang *et al.* [6] These are not observed, however, as shown in this study.

6.2 Experiment

A detailed description of the velocity mapping apparatus has been reported elsewhere [2] thus only a brief summary of the experimental details will be given here. A pulsed and skimmed supersonic beam of pure O_2 is directed down the axis of a time-of-flight (TOF) mass spectrometer and crossed at right angles by the line-narrowed ($\Delta\nu \sim 0.5$ cm^{-1}) ArF excimer laser. The 193 nm light (15 ns pulse width, 25 mJ per pulse, $\sim 5\times10^{16}$ photons) was focused with a 35 cm lens on to the molecular beam resulting in an intensity of $\sim$ 5x10^{10} W/cm^2. The line-narrowed scanning range is 51,600-51,800 cm^{-1} and under the best conditions, a broad-band component with integrated intensity at least equal to that of the line-narrowed accompanies the narrow-band output. The laser can also be operated fully broadband ($\Delta\nu \sim 200$ cm^{-1}) by blocking the oscillator grating.

A series of dichroic mirrors used to direct the beam serve also to attenuate the horizontal component of the initially unpolarized beam and result in >99% vertical polarization at the interaction zone. The atomic products of predissociation were monitored by two-photon resonance enhanced multiphoton ionization ((2+1) REMPI) of $O(^3P_2)$ using the 226 nm output of a counter-propagating second Nd:YAG pumped frequency-doubled dye laser operating with Coumarin 47. The probe laser beam was focussed on to the molecular beam using a 20 cm focal length lens and had a typical energy of less than 1 mJ per pulse. The detection laser pulse arrived ~20 ns after the photolysis pulse. To ensure equal detectivity for all velocity groups the detection laser wavelength was scanned repetitively across the Doppler profile of the (2+1) REMPI transition. The formed ions were extracted from the ionization region through a grounded time-of-flight tube and crushed onto a two-dimensional microchannel plate / phosphor screen detector read by a CCD camera. Mass selectivity was achieved by pulsing on the gain of the detector as the O^+ ions arrive. Typically, 25,000 laser shots were used to produce the final raw image which was then inverted using an inverse (2D-3D) Abel transformation.

The overall quality of the images obtained using the excimer laser, particularly those taken in combination with the additional $O(^3P_2)$ detection laser, were not as high as images obtained using Nd:YAG pumped dye lasers. This could partially arise from insufficient time-focusing (‘pancaking’ of the 3-D image before it hits the detector) due to the longer pulselength of the excimer (15 ns in comparison to ~3 ns from doubled-dye lasers pumped by a Nd:YAG laser). More likely, the problem arises from the rectangular beam geometry (3 by 1 cm) of the excimer laser. The laser is focused with a simple plano-convex lens on to the molecular beam, with the longer laser beam axis lying parallel to the time-of-flight axis. Because the laser beam spatial pattern shows shot-to-shot fluctuations, the position of the ion origin will be spread along the TOF axis. Velocity mapping magnifies the image by slightly different factors dependent on this position, which will thus lower the sharpness of the image. Shot-to-shot fluctuations in the focal position are particularly disturbing for the two-laser experiments for obvious reasons. Overall, the energy resolution of the excimer-laser-produced images is estimated to be ~60 meV at 1 eV kinetic energy release, compared to ~30 meV for images produced by a Nd:YAG pumped dye laser [12].

6.3 Results

Typical images obtained with the 193 nm light alone and along with the $O(^3P_2)$ detection laser are shown in Figure 6.2. Raw half-images are presented on the left-hand sides of Figure 6.2(a) for the one-laser result and and 6.2(c) for the two-laser result, while the Abel-inverted half-image is shown on the right sides of Figures 6.2(b) and 6.2(d). The images show a series of sharp concentric rings whose velocity are directly calibrated using the known [3] $O(^3P_2)$ atom signals from the detection laser alone, which also produces $O(^3P_2)$ atoms from the photodissociation of O_2via one- and two-photon absorption. The radius of the ring is proportional to the velocity of the products, so after calibration the kinetic energy release corresponding to all other rings is determined. Accuracy is high enough that the number of photons absorbed can be distinguished in the photodissociation processes. Distributions of the total kinetic energy release (i.e., twice the atom kinetic energy) extracted from the raw images Fig. 6.2(a) and 6.2(b) are shown in Figures 6.3(a) and 6.3(b), respectively. These are obtained from the inverted image by integrating over the full angular distribution.

As seen in Figure 6.2, each dissociation channel produces some signal along the vertical

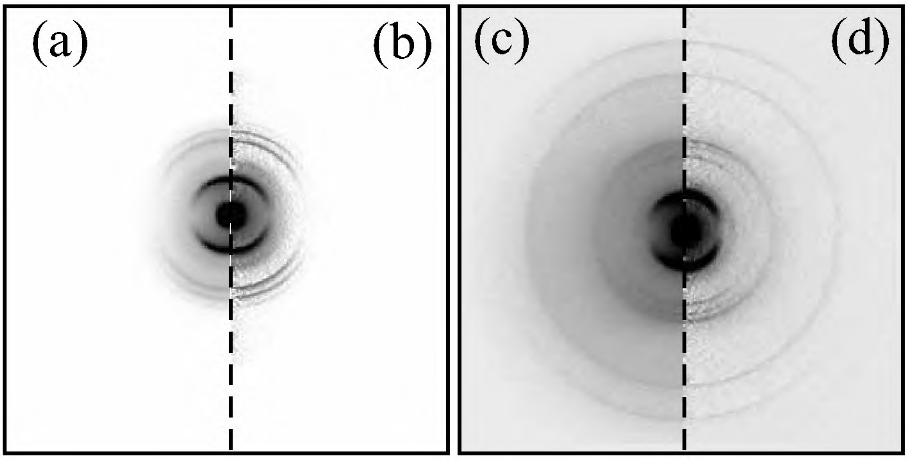

Figure 6.2: *Raw (left side) and Abel-inverted (right side) O^+ images: (a) and (b) for 193 nm laserexcitation of O_2;(c) and (d) for 193 nm excitation of O_2 with $O(^3P_2)$ detection.*

axis. The spectral behavior of the kinetic energy distribution can be investigated by fixing the detection laser on the top of the $O(^3P_2)$ 2+1 REMPI wavelength, so that atoms flying along the direction of the laser polarization (no Doppler shift) are detected. The image processing software is then set to average a vertical slice of the image approximately 10 pixels wide. The computer software compresses and stores this slice as an array 1 pixel wide (averaging the approximate 10 pixels) by 286 pixels high. For each following array the dissociation laser wavelength is stepped. The top and bottom halves (upward and downward traveling ions) of the 2-D array of velocity distribution versus dissociation laser frequency are then averaged. The top half of such an array for O^+ (and $O(^3P_2)$) detection from O_2 is shown in Figure 6.4.

The analysis of the different dissociation channels as a function of laser bandwidth and frequency will be discussed for each channel separately. First, the general features of the images will be summarized. With the 193 nm laser working in the broadband mode features are seen in the 0-0.40 eV and 0.80 -1.50 eV range along with very weak features in the 2.70-3.50 eV range, as seen in Figure 6.3(a). These results are in qualitative agreement with the time-of-flight results of Yang *et al.* [6] using also a broadband laser, except their TOF resolution was too low to resolve the individual peaks seen in Fig. 6.3(a). The weaker signals around 3 eV were not reported. When the ArF laser is operated in the narrowband mode (regardless of wavelength), essentially the same image is observed, but the signals in the 0.80-1.50 eV and 2.70-3.50 eV range are around five times weaker.

On adding the $O(^3P_2)$ detection laser several new rings appear in the image, mainly at higher energies than the (193 nm)-laser-only signals. Two peaks, labeled in Figure 6.3, are due to the 226 nm detection laser only and correspond to one-photon dissociation (creating $O(^3P_2)+O(^3P)$

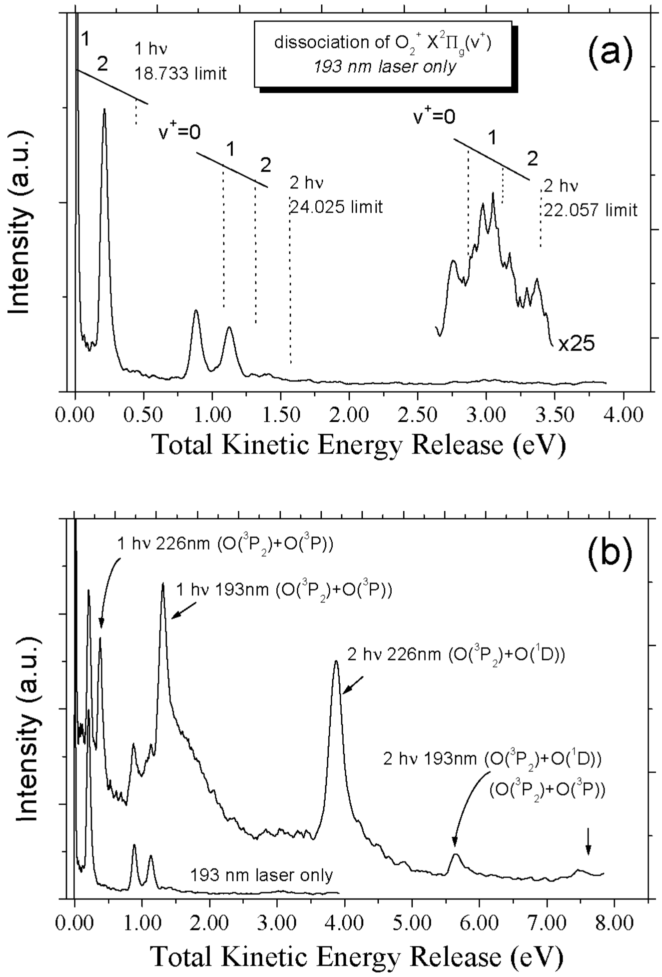

Figure 6.3: *Kinetic energy distributions for the images shown in Figure 6.2.*

products) and two-photon dissociation (creating $O(^3P_2)+O(^1D)$ products) of O_2. Three other rings correspond to dissociation at 193 nm by one-photon absorption (creating $O(^3P_2)+O(^3P)$ products, 1.29 eV total KER) and by two-photon absorption (creating $O(^3P_2)+O(^1D)$, 5.65 eV; and $O(^3P_2)+O(^3P)$ products, 7.62 eV). A broad shoulder to higher energy accompanying the 193 nm one-photon dissociation signal grows in strength relative to the main peak at 1.29 eV total KER when the laser is operated narrow-band and resonant with a Schumann-Runge (SR) transition. This is probably due to space-charge effects in the focus of the 226 nm detection laser. Note that with the 193 nm laser alone (broadband or narrow-band), no signal appears at 1.29 eV, indicating that non-resonant three-photon ionization of $O(^3P)$ atoms by the excimer laser does not take place to any significant extent.

6.4 Discussion

In the following sections the photophysical process observed is discussed according to how many photons have been absorbed by either O_2 or O_2^+. These different stages are labeled in Figure 6.1 as (1), one-photon absorption, (2), two-photon absorption, and (3) three-photon absorption by O_2, and (4), one-photon absorption and (5), two-photon absorption by O_2^+.

6.4.1 One-photon absorption at 193 nm by O_2

The photodissociation and photoionization of molecular oxygen in the vacuum ultraviolet, especially predissociation and direct dissociation via the strong Schumann-Runge (SR) bands and continuum, is an important process in our atmosphere and has accordingly received much attention in the literature. Recent studies on the photodissociation of O_2 via the Schumann-Runge bands have been reported by Lin *et al.* [13] Huang and Huang *et al.* [14] and by Eppink *et al.* [12] for the SR continuum, and by Leahy *et al.* [16] , Gibson *et al.* [17] , and Matsumi *et al.* [18] for the SR bands. Tonokura *et al.* [19] and Buijsse *et al.* [3] have reported similar studies for the lower lying Herzberg continuum. Information on one-photon dissociation is obtained from velocity map imaging by examining the KER = 1.29 eV peak labeled in Fig. 6.3(b). Most relevant to this study, Lewis *et al.* [4] have examined predissociation mechanisms in the SR bands and extracted the lifetime broadened linewidths from the absorption spectrum. In the 193 nm region the SR bands are weak due to poor Franck-Condon overlap (σ for excitation of N = 15-19 to B(v=4) $\sim$2x10^{-20}cm^{-2}) but the underlying, optically forbidden, Herzberg continuum (HC) is a factor of $\sim$3000 weaker (σ $\sim$7x10^{-24}cm^{-2}) than the SR resonances [20, 21]. With the ArF laser tuned on resonance, the narrow-band component will thus strongly favor the SR band, but the always-present broadband component of the laser radiation still makes a significant contribution. All molecules can absorb the broadband component via the HC, while only the small fraction of the resonant high N states can contribute to the SR signal.

The tunable ArF laser can excite only the higher rotational levels (N = 15, 17, 19, 21, 23) of ground state O_2 to the v=4 level of the $B^3\Sigma_u^-$ state. Despite the use of a supersonic pulsed expansion, sufficient population remains in these higher J levels to observe an enhanced $O(^3P_2)$ signal on scanning through the resonances, as shown in the 3000 m/s region of Figure 6.4. Independent measurements [12] of the pulsed valve expansion indicate that the vast majority of rotational population in the beam after the expansion is in the N = 1, 3, and to a much less extent the N = 5 state. At room temperature the populations of N = 15, 17, 19, and 21 is 8%, 6%, 4%, and 2%, respectively, and after the expansion these fractional populations are reduced significantly by an unknown amount.

Figure 6.5 shows the angular distributions for the one-photon dissociation signal at 1.29 eV when using broadband radiation and narrow-band radiation resonant with a SR band, in this case the P(17) line at 51,736 cm^{-1}. Fitting to Eq. (6.1) yields β_{on}=0.69 ± 0.05 for the narrow-band, on-resonance laser and β_{BB}=0.54 ± 0.05 for the broad band radiation. Not shown in Fig. 6.5 is β_{off}=0.51 ± 0.05 for narrow-band, off-resonance laser excitation. Table 6.1 lists β_{on} values measured for the P(15), P(17), and P(19) transitions corresponding to the final state rotational quantum numbers N'=14, N'=16 and N'=18, respectively. Also presented in Table 6.1 are the corresponding calculated rotational period T and lifetime τ from spectral linewidth measurements

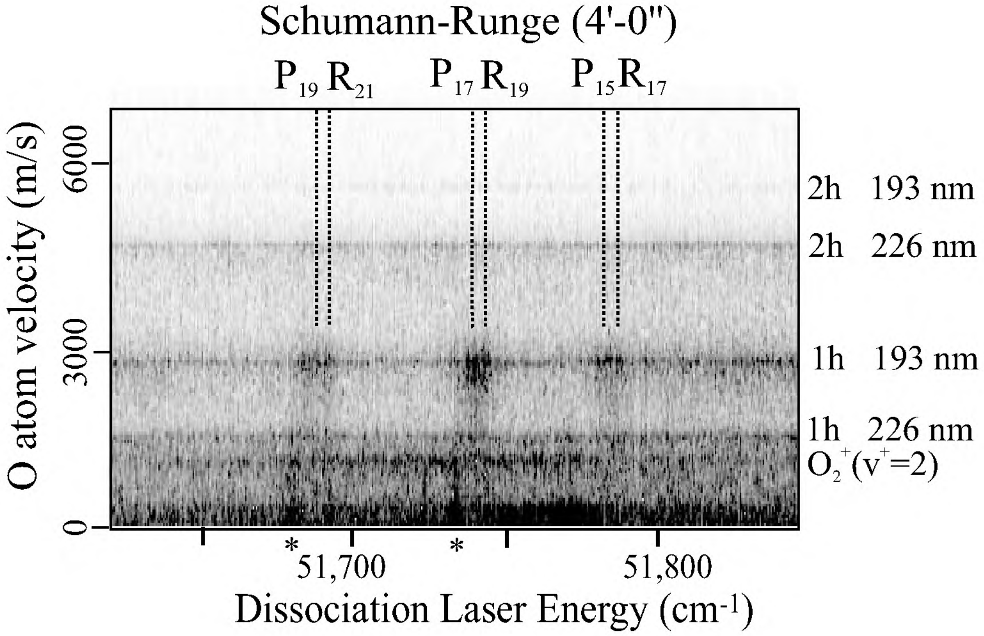

Figure 6.4: *Velocity distribution spectrum of O_2. O atom velocity versus dissociation laser wavelength. Vertical lines indicate the Schumann-Runge (4'-0") P and R branches, the * indicates the two-photon Rydberg states.*

of Lewis *et al.* [4] . Filling the values of T and τ into formula (6.2) gives the calculated classical value of the anisotropy parameter β_{calc}. It should be noted that the P(N'-1) branches are only ~ 6 cm^{-1} separated from the R(N'+1) transitions, where N' is the rotational quantum number of the $B^3\Sigma_u^-$ state, while the natural linewidths of these transitions are ~4 cm^{-1}. It is thus not possible to excite a single N' state and therefore some mixing of the state 4 quanta higher than the value listed in Table 6.1 will take place.

The measured beta values β_{on} show a different value in Table 6.1 than the expected β_{calc}. This can be explained by the fact that the ArF laser has a underlying broad band component when used in narrow band mode. Correction of the measured β_{on} values for the broad band component of the laser beam can be done very qualitatively in the following manner. The broad band (BB) β value, which results from the combination of SR and HC contributions, is β_{BB}=0.54± 0.05. A measured narrow-band β value is assumed to result from $\frac{1}{2}$ narrow-band excitation and $\frac{1}{2}$ broadband excitation. The corrected beta value for the HC, β_{HC}, can be determined using the corresponding expression $\beta_{off} = \frac{1}{2}\beta_{HC} + \frac{1}{2}\beta_{BB}$. The measured value β_{off}= 0.51± 0.05 implies that the average value of beta for the Herzberg Continuum is β_{HC} = 0.48± 0.10. Off-resonance, the β_{HC} value appears to be raised by the broad-band component while on-resonance, the experimental β_{on}value is lowered by the broad-band component. Because of the large error bars these values are extremely qualitative. The same method is used to derive the beta value for the SR transitions when the laser is set on-resonance. Now the expression $\beta_{on} = \frac{1}{2}\beta_{SR} + \frac{1}{2}\beta_{BB}$ is used. As seen in Table 6.1 , good agreement is found between the corrected β_{SR} values from

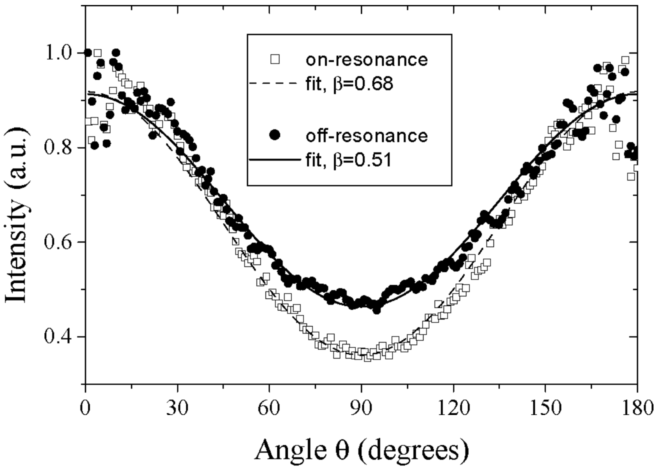

Figure 6.5: *Angular distributions for 193 nm one-photon dissociation of* O_2.

the angular distributions and those from the linewidth measurements β_{calc}. Leahy *et al.* [16] also found good agreement between their measured beta parameter and beta predicted from the corresponding linewidth measurement, for the $B^3\Sigma_u^-$ (v=7, N'=4) state.

Table 6.1: *Measured* (β_{on}), *predicted* (β_{calc}) *and corrected* (β_{SR}) *anisotropy parameters for selected rotational levels N' of the* $B^3\Sigma_u^-$ *(v=4) states. T is the N' state rotational period and* τ *the state lifetime obtained from the linewidth* $\delta\nu$ *measurements of Lewis et al. [4].*

N'	β_{on}	$\delta\nu$ (cm^{-1})	τ (10^{-12} s)	T (10^{-12} s)	β_{calc}	β_{SR}
14	0.62±0.05	3.68	1.44	1.53	0.83	0.70
16	0.68±0.05	3.81	1.39	1.34	0.78	0.82
18	0.63±0.05	3.79	1.40	1.20	0.73	0.72

The fractional population of the N = 15, 17, and 19 states can be estimated by combining the values for $\beta_{HC} = 0.48$, the average β value for SR $\langle\beta_{SR}\rangle = 0.75$ and the relative absorption strengths. Linewidths of the 6 (P & R) SR bands are $\sim$ 4 cm^{-1} FWHM each, thus the SR components can absorb $\sim$12% of the laser light, but with 3000 times more absorption strength than the HC component. Assuming that $\beta_{BB} = \langle\beta_{SR}\rangle(0.12)3000(1\text{-}f) + \beta_{HC}(0.88)(1)(f)$ where f is the fractional population of the N<15 states yields a value of f = 99.96. A fractional population in the high N levels of only 0.04% is thus sufficient to account for the observed SR contributions. Alternatively, it is only because of the very strong cooling of the high N states in the supersonic expansion that an estimate of β_{HC} is possible.

Beta values for $O(^3P_2)$ atoms produced from dissociation of O_2 via the Herzberg continuum for dissociation at 226 and 204 nm of β_{HC} = 0.64 and 0.87, respectively, have been reported previously [3]. The value reported here for beta at 193 nm of β_{HC} = 0.48 fits in well with theoretical analysis of the Herzberg continuum given in ref. [3]. Of the three components active in the HC, the $A^3\Sigma_u^+ \leftarrow X^3\Sigma_g^-$ transition is dominant, especially at shorter wavelengths because the $A'^3\Delta_u \leftarrow X^3\Sigma_g^-$ and $c^1\Sigma_u^- \leftarrow X^3\Sigma_g^-$ transitions reach their maximum at longer wavelengths than the $A^3\Sigma_u^+ \leftarrow X^3\Sigma_g^-$. With progressively shorter wavelengths it is expected that the dissociation will approach the sudden-recoil limit [3], in which case the j=2 atoms should tend towards a more perpendicular angular distribution. While a prediction for β in the sudden recoil limit has not been made for 193 nm dissociation, the present value fits well in the suggested trends, and with preliminary results from an extensive theoretical analysis by Groenenboom and coworkers [22] giving β values for 204 nm of β=0.73 in semiclassical calculations and β=0.53 for the diabatic model. A more complete study including β values for the j=1 and j=0 states is desirable. Matsumi and Kawasaki [18] have reported branching ratios for j=2:1:0 for broadband ArF laser radiation of 0.47:0.31:0.22.

6.4.2 Two-photon absorption by O_2

Two-photon excitation by the tunable ArF laser covers 103,200-103,600 cm^{-1} while the ionization energy [23] lies at 97,347 cm^{-1}. In this energy range two processes can thus occur, dissociation to neutral, ground-state atoms or (auto)ionization to form O_2^+. Ionization producing O_2^+ in the v^+=0-3 vibrational levels occurs either by direct two-photon absorption or by two-photon excitation to autoionizing Rydberg states converging on either the ground state or excited electronic states of the ion. Photodissociation by two ArF laser photons exceeds the dissociation limits of ($O(^3P)+O(^3P)$, 5.115 eV), ($O(^1D)+O(^3P)$, 7.08 eV), ($O(^1D)+O(^1D)$, 9.05 eV) (and $O(^1S)+O(^3P)$, 9.26 eV).

Dissociation to neutral ground state atoms by two-photon absorption will first be discussed. This process is probed in this study by detection of $O(^3P_2)$ atoms, which gives information on all but the $O(^1D)+O(^1D)$ dissociation channel. Results are shown in Figure 6.3 where two-photon dissociation to form $O(^3P)+O(^1D)$(5.74 KER) and $O(^3P)+O(^3P)$(7.71 eV KER) are indicated. This is a two-laser experiment with a separate detection laser which is always much less efficient than a one-laser experiment. Despite this, the two-photon dissociation channel to $O(^3P)+O(^1D)$ is one of the strongest signals suggesting that this is the most probable event following two-photon absorption. This corroborates the finding of van der Zande *et al.* [24] who found that the large majority of O_2 molecules excited to an energy above v^+=2 of the ion dissociate instead of ionize. In their experiments O atoms from charge exchange collisions of O_2^+ $a^4\Pi_u$ ions with Cs were measured and evidence was found for the production and predissociation of lower vibrational levels of the $H^3\Pi_u(3s\sigma_g)$ Rydberg state which lie in the same energy region as probed in this study. In the O atom KER curves the $O(^1D)+O(^3P)$ channel was strongest but evidence was found for activity in all accessible dissociation channels. In the present work which prepares levels of overall *gerade* symmetry the $O(^1D)+O(^3P)$ channel is again strongest. No signal is seen in Figure 6.3 at 3.57 eV for activity in the accessible $O(^1S)+O(^3P)$ channel.

While the formation of $O_2^+$was not directly monitored in this study the O^+ images shown in Figure 6.2(a) reveal information on which O_2^+ (v^+) states are formed. The O_2^+ dissociation data (next section) indicate that mainly v^+= 0, 1, and 2 vibrational levels of ground electronic state O_2^+ are produced, although v^+=3 production is energetically allowed. Inspection of Fig. 6.4 for these dissociation channels show that there is no striking wavelength dependence for production of the specific v^+=0, 1 and 2 states of O_2^+ $X^2\Pi_g(v^+)$. There is, however, structure in Fig. 6.4 in the region of zero velocity, which is due mainly to leakage of O_2^+ signal through the front channelplate in the 2-D detector, whose gain has been gated to select the O^+ mass. Peaks seen at 51,678 cm^{-1}, and 51,730 cm^{-1} (marked with a * in Fig. 6.4 are assigned to the 6s-5d $^3\Sigma_g^-$(v=5, Ω=1/2) and 9s-8d $^3\Sigma_g^-$ (v=4,Ω=3/2) Rydberg levels converging to the v^+=5 and v^+=4 levels of the X state of the ion, respectively. Pratt *et al.* [25] characterized the lower states of this same s-d complex previously. A more complete assignment of these and weaker states observed in the ArF tuning window will be discussed in a separate publication [26]. These levels serve as stable platforms for absorption of a third ArF laser photon, as discussed in the next subsection.

6.4.3 Three-photon absorption by O_2

Three-photon absorption by O_2 takes place when the laser is resonant with the ns-(n-1)d $^3\Sigma_g^-$ two-photon allowed Rydberg states. This leads to enhanced production of O_2^+ ions, as seen in the zero velocity region of Fig. 6.4. Previous studies have shown the same states are detectable by four-wave mixing [27] and by laser induced fluorescence [28] which must arise from electronically excited O_2^+ ions. These electronically excited O_2^+ ions are reachable only by three-photon absorption by neutral O_2. A fraction of the O_2^+ ions must be formed in the $A^2\Pi_u$ excited electronic states that subsequently fluoresce in the UV. Visible fluorescence presumably due to $a^4\Pi$–$b^4\Sigma^-$ transitions has also been observed [28]. Laser induced fluorescence following excitation of these states has been previously observed in ArF laser based diagnostics studies [5] but the states are assigned here for the first time. Unfortunately, a velocity map image was not obtained with the tunable ArF laser resonant on one of the two listed bands. Images obtained for states of the same series with slightly lower energies indeed show the production of O_2^+ in higher vibrational levels of the A state [29] following three-photon absorption.

6.4.4 Photodissociation of O_2^+

Molecular oxygen ions are created in the X (v^+=0, 1, 2, 3) states following two-photon, and to a smaller extent, three-photon absorption by O_2. Considering the rather long pulselength of the ArF laser (15ns), further absorption by O_2^+ will lead to photodissociation of the molecular ion and creation of the detected O^+ products. Table 6.2 lists the lowest dissociation limits of O_2^+ and their dissociation products along with their molecular states [30].

One-photon dissociation of O_2^+

Because the ionic dissociation energy is 6.62 eV, all vibrational states except v^+=0 can be photodissociated with one ArF laser photon of 6.4 eV. The low kinetic energy signal in Figure 6.3 is assigned to one-photon dissociation of $X^2\Pi_g$ (v^+=1,2) to the $O^+(^4S)$ + $O(^3P)$ dissociation limit, which correlates with $^{2,4,6}(\Sigma^+,\Pi)_{g,u}$ states. Since the ionic ground state symmetry is $X^2\Pi_g$, the one-photon allowed states are the A $^2\Pi_u$ and $^2\Sigma_u^+$, the latter of which is predicted [31] to be weakly bound and correlates with the first dissociation limit. There are no known doublet Σ,Π ungerade bound states in the energy region near the first dissociation limit [32] so the oxygen ion

Table 6.2: *Dissociation limits of O_2^+ and the correlating molecular state*

Dissociation products	Energy (eV)	Molecular states
$O^+(^4S) + O(^3P)$	18.733	$^{2,4,6}(\Sigma^+,\Pi)_{g,u}$
$O^+(^4S) + O(^1D)$	20.700	$^4(\Sigma^-,\Pi,\Delta)_{g,u}$
$O^+(^2D) + O(^3P)$	22.057	$^{2,4}(\Sigma^+,\Sigma^-,\Pi,\Delta,\Phi)_{g,u}$
$O^+(^4S) + O(^1S)$	22.923	$^4(\Sigma^-)_{g,u}$
$O^+(^2P) + O(^3P)$	23.750	$^{2,4}(\Sigma^+,\Sigma^-,\Pi,\Delta)_{g,u}$
$O^+(^2D) + O(^1D)$	24.025	$^2(\Sigma^+,\Sigma^-,\Pi,\Delta,\Phi,\Gamma)_{g,u}$

can only photodissociate on the repulsive walls of the A $^2\Pi_u$ and $^2\Sigma_u^+$ states. This results in a mixture of a parallel and perpendicular transition that should be reflected in the angular distribution of the products. The measured β parameters for the one-photon dissociation of the $X^2\Pi_g(v^+=1)$ and $X^2\Pi_g(v^+=2)$ are 0.43±0.11 and 1.81±0.07 respectively. These β values, which are similar to the ones Parker and Eppink [33] measured, indicate a contribution from the $^2\Sigma_u^+$ state in a direct dissociation process. These values were obtained in the one-color experiment and no difference could be observed in β when the excimer laser was used in small-band or broad-band mode.

Two-photon absorption by O_2^+

The set of peaks in the 0.8-1.50 eV and 2.5-3.5 eV region of Fig. 6.2 are found to be weaker relative to the one-photon peaks in the 0-0.3 eV region when using broad-band light compared to narrow-band light, which suggests that they arise from a two-photon excitation process. Two photon excitation of the $X^2\Pi_g$ $(v^+=0,1,2)$ states brings the total energy between 24.9 and 25.6 eV. At these energies all the dissociation limits listed in Table 6.2 are energetically accessible. Yet, the closest lying limit, $O^+(^2D) + O(^1D)$ (24.025 eV) is assigned in Fig. 6.2 as the major one in the kinetic energy spectrum and a small yield in the $O^+(^2D) + O(^3P)$ (22.057 eV) channel can also be seen. A two-photon step starting in the $X^2\Pi_g$state has the A $^2\Pi_u$ or $^2\Sigma_u^+$ as intermediate state and would therefore end according to selection rules in a $^2\Pi_g$, $^2\Delta_g$or $^2\Sigma_g^-$ state. Predissociation or direct dissociation from these molecular states could be responsible for the observed signals, or curve crossing to repulsive states could also take place. Dissociation dynamics in this energy region for oxygen have been studied using one-XUV-photon dissociation from the neutral ground state of oxygen $X^3\Sigma_g^-$by Erman *et al.* [34]. Their technique probes one-photon allowed transitions to states that have Franck-Condon overlap with the O_2 ground state. Erman *et al.* [34] measured the energy distributions of O^+ after XUV photodissociation and found that the maximum KER is less than 2 eV, and the distribution looks similar for the full 24-34 eV energy region. They concluded that the dominant pathway is curve crossing to any dissociative state with good Franck-Condon overlap that correlates with the dissociation limit lying closest to the excitation energy. The present results support this observation.

Beebe *et al.* [30] have calculated some states in this region: the $^2\Sigma_g^-$ (2) at 23.42 eV, the

$^2\Sigma_g^-$ (3) 23.68 eV and the $^2\Sigma_g^-$ (4) at 24.89 eV. These states have the proper symmetry $^2\Sigma_g^-$ for two-step excitation, so the probability of these pathways should be reasonably high. The $^2\Sigma_g^-$ (4) state lies in the excitation energy region but can not directly dissociate since it correlates with a higher (25.72 eV) limit. This state can couple with other $^2\Sigma_g^-$ states in order to dissociate. The available $^2\Sigma_g^-$ states are: the $^2\Sigma_g^-$ (3) that correlates towards the observed $O^+(^2D)$ + $O(^1D)$ limit, the $^2\Sigma_g^-$ (2) that correlates towards $O^+(^2P)$ + $O(^3P)$ (not seen) and the $^2\Sigma_g^-$ that has the $O^+(^2D)$ + $O(^3P)$ as limit (weakly seen). According to Erman *et al.* [27] the closest lying limit is the most probable pathway and therefore the major one seen is the $O^+(^2D)$ + $O(^1D)$ limit.

The results of the anisotropy parameters for the two-photon dissociation channels could be fitted well with a one-photon angular distribution, i.e., the use of only β as a fitting parameter was sufficient. This resulting β values were 1.83±0.39 and 1.74±0.26 for the two-photon dissociation of the $X^2\Pi_g$ (v^+=0) and $X^2\Pi_g$ (v^+=1) state, respectively. Qualitatively, these high values suggest a parallel transition for the first and second step and it was noted before that the one-photon transition is also nearly parallel. This suggests the intermediate state should have a Π_u character, like the ground state, but then the final state would be a Π_g state and not $^2\Sigma_g^-$. Several Π_g correlate to the observed dissociation limits including the closest-lying $O^+(^2D)$ + $O(^1D)$ limit. It should be mentioned, however, that other effects such as axis alignment due to photoselection, rotation during dissociation, and coherent versus step-wise two-photon excitation could also play a role in the observed angular distribution anisotropy.

6.5 Conclusion

The angular and kinetic energy distributions of O^+ atom fragments after O_2 photodissociation with a narrow-band tunable ArF were measured and analyzed using the velocity map imaging technique. Product $O(^3P_2)$ atoms were also detected via (2+1) REMPI with a second laser system. The main $O(^3P_2)$ signals are from two-photon dissociation, one-photon dissociation via the Herzberg continuum, and predissociation following the $B^3\Sigma_u^-$ (v=4)← $X^3\Sigma_g^-$ (v=0) transitions. The Herzberg continuum gives an average value of β=0.48 and the measured β values for the Schumann-Runge bands were in good agreement with previous lifetime measurements of the $B^3\Sigma_u^-$(v=4) state. O_2^+ $X^2\Pi_g$ (v^+=0,1,2) is formed at the two-photon level at all wavelengths and at several specific wavelengths in the laser tuning range O_2^+ resonances due to (2+1) REMPI via the $ns\sigma_g(n\text{-}1)d\pi_g\,^1\Sigma_g^+$ Rydberg states are also observed. The product O_2^+ $X^2\Pi_g$ vibrational states are photodissociated via a one- or two-photon process.

Acknowledgments

This work was part of the research program of the “Stichting voor Fundamenteel Onderzoek der Materie (FOM)” and is financially supported by the “Nederlandse Organisatie voor Wetenschappelijk Onderzoek (NWO)”. The authors thank M.C. van Beek, N.J. Dam and J.J. ter Meulen for help and use of the tunable excimer laser. The authors also thank C. Sikkens and C. Timmer for technical support.

References

[1] J.F. Noxon and A.E. Johanson, Planet. Space. Sci. **20**, 2125 (1972).

[2] A.T.J.B. Eppink and D.H. Parker, Rev. Sci. Instr. **68**, 3477 (1997).

[3] B. Buijsse, W.J. van der Zande, A.T.J.B. Eppink, D.H. Parker, B.R. Lewis, and S.T. Gibson, J. Chem. Phys. **108**, 7229 (1998).

[4] B.R. Lewis, S.T. Gibson, and P.M. Dooley, J. Chem. Phys. **100**, 7012 (1994).

[5] E.W. Rothe and P. Andresen, Appl. Opt. **36**, 3971 (1997).

[6] S. Yang, W.T. Hill and S.N. Dixit, J. Chem. Phys. **100,** 6434 (1994).

[7] R.N. Zare, *Angular Momentum* (Wiley, New York, (1988).

[8] C. Jonah, J. Chem. Phys. **55**, 1915 (1971).

[9] M. Nicolet and R. Kennes, Planet. Space Sci. **34**, 1043 (1986).

[10] J.P. England, B.R. Lewis, and M.L. Ginter, J. Chem. Phys. **105**, 1754 (1996).

[11] H. Park, P.J. Miller, W.A. Chupka and S.D. Colson, J. Chem. Phys. **89**, 3919 (1988), *ibid*, **89**, 6676 (1988).

[12] A.T.J.B. Eppink, B.L.G. Bakker, and D.H. Parker. *SPIE* **3271**, 177 (1998).

[13] J.L. Lin, D.W. Hwang, Y.T. Lee and X. Yang, J.Chem. Phys. **109**, 1758 (1998).

[14] Y. Huang and R.J. Gordon, J. Chem. Phys. **94**, 2460 (1991).

[15] A.T.J.B. Eppink, B. Buijsse, M.H.M. Janssen, W. J. van der Zande, and D.H. Parker, J. Chem. Phys. **108**, 1305 (1998).

[16] D.J. Leahy, D.L. Osborne, D.R. Cyr, and D.M. Neumark, J. Chem. Phys. **103**, 2495 (1995).

[17] S.T. Gibson, B.R. Lewis, K.G.H. Baldwin, and J.H. Carver, J. Chem. Phys. **94**, 1060 (1991).

[18] Y. Matsumi and M. Kawasaki, J. Chem. Phys. **93**, 2481 (1990).

[19] K. Tonokura, N. Shafer, Y. Matsumi, and M. Kawasaki, J. Chem. Phys. **95**, 3394 (1991).

[20] M. Nicolet and R. Kennes, Planet. Space Sci. **34**, 1043 (1986).

[21] M. Nicolet and R. Kennes, Planet. Space Sci. **37**, 459 (1988).

[22] G.C. Groenenboom and M.C.G.N. van Vroonhoven , submitted to J. Chem. Phys.

[23] W. Kong and J.W. Hepburn, Can. J. Phys. **72**, 1284 (1994).

[24] W.J. van der Zande, W. Koot, J.R. Peterson and J. Los, Chem. Phys. **126**, 169 (1988).

[25] S.T. Pratt, J.L. Dehmer and P.M. Dehmer, J. Chem. Phys. **93**, 3072 (1990).

[26] B.L.G. Bakker, G. Meijer and D.H. Parker, work in progress.

[27] M. Versluis, G. Meijer and D.W. Chandler, Appl. Opt. **33**, 3289 (1994).

[28] M. Versluis, *Ph. D. dissertation*, (University of Nijmegen, Nijmegen, The Netherlands, 1992) ; G. Laufer and R. L McKenzie, *AIAA/NASA/AFWAL Conference on Sensors and Measerements for Aeronautical Applications*, (Atlanta, September 7-9, 1988).

[29] B.L.G. Bakker, A.T.J.B. Eppink and D.H. Parker, work in progress.

[30] N.H.F. Beebe, E.W. Thulstrup and A. Andersen, J. Chem. Phys. **64**, 2080 (1976).

[31] C.M. Marian, R. Marian, S.D. Peyerimhoff, B.A. Hess, R.J. Buenker, G. Seger, Mol. Phys. **46**, 779 (1982).

[32] T. Tanaka, H. Yoshii, Y. Morioka, T. Hayaishi, K, Ito, R.I. Hall, J. Chem. Phys. **108**, 6240 (1998).

[33] D.H. Parker and A.T.J.B. Eppink, J. Chem. Phys. **107,** 2357 (1997).

[34] P. Erman, A. Karawajcyk, E. Rachlew-Kallne, M. Stankiewicz and K. Yoshiki Franzen, J. Phys. B **29**, 5785 (1996).

Chapter 7

Non-resonant photofragmentation / ionization dynamics of O_2 using picosecond and femtosecond laser pulses at 248 nm

Abstract

Photodissociation / ionization of molecular oxygen in a cold molecular beam is studied using a short-pulse laser beam at 248 nm and velocity map imaging. Both photoelectron and O^+ images are recorded for laser pulsewidths of 5 and 0.5 ps. Most of the observed ionization dynamics takes place after absorption of four laser photons, equivalent to 20 eV excitation energy, in an above threshold ionization process. Two main channels are identified: post-dissociative ionization creating $O(^3P)$ + O**3s"$(^1P,^3P)$ atoms where O** is an electronically excited autoionizing atom, and molecular (auto)ionization to create a range of highly vibrationally excited ground electronic state O_2^+ ions. The observed O^+ signals then arise from resonance-enhanced two-photon dissociation of O_2^+ or autoionization of O** atoms, while the electron signals arise from ionization of O_2 or autoionization of O**. The latter channel can be used to directly scale the photoelectron and O^+ signal strengths. The O^+images show strong differences for 0.5 psec and 5 psec pulse which could arise from AC Stark shifting of levels involved in the $A^2\Pi_u \leftarrow X^2\Pi_g$ transition of O_2^+. With resonance enhancement, two-photon dissociation of O_2^+ is the dominant process producing O^+ ions. The O^+ angular distributions show an anisotropy that is more extreme than a simple two-step dissociation, which is attributed to alignment effects.

7.1 Introduction

In the field of photo-dissociation and ionization dynamics molecular oxygen is one of the most thoroughly studied of all diatomic molecules, not only because it provides a test of fundamental quantum theory, but also because of its dominant role in atmospheric physics.

On probing O_2 with intense pulsed lasers higher order interactions of laser fields with small molecules can also be investigated. The photodissociation of O_2 at 248 nm is a good system for studying multiphoton processes especially since O_2 does not show any significant resonant absorption at the one- or two-photon levels. Walker *et al.* [1] have also reported non-resonant multiphoton excitation of O_2, using nanosecond and 50 psec pulses around 532 nm and 355 nm. On a practical side, short-pulse lasers have been used as a universal detector of nascent molecules, where it is assumed that non-resonant detection takes place for all quantum states. We have previously reported non-resonant 248 nm detection of CH_3 radicals for example, following dissociation of CH_3Br [2] and CH_3I [3]. A KrF excimer laser [4] is used to generate intense pulses of 248 nm light. This is a common photolysis wavelength, and is especially attractive for the study of ozone photolysis [5]. In this case it is important to know how O_2, a photolysis product, interacts with 248-nm radiation.

In this study O^+ ions and photoelectrons created by focusing a short-pulse 248 nm laser beam onto a cold molecular beam of O_2 are measured using velocity map imaging [6], which records the speed and angular distributions of the fragments. When using photons of 4.987 eV, a minimum of three photons are needed to photoionize O_2, (IP O_2 = 12.08 eV) while at least four photons are needed to create O^+ via photodissociation ($O_2 \rightarrow O^+(^4S)+O(^3P)$ 18.733 eV) or ion pair formation ($O_2 \rightarrow O^+(^4S)+O^-(^2P^0)$ 17.272 eV). As shown in this study, ionization takes place not at the three-photon level where it is first energetically allowed, but predominately at the four-photon level. Photoelectrons with kinetic energies higher than the photon energy are created, which can be considered above threshold ionization (ATI). Unlike in the seminal atomic ATI studies by Agostini *et al.* [7] involving free-free transitions, in molecules this process involves a bound-free transition from a super-excited state at the third photon level. Autoionization also creates a wide range of vibrationally excited X $^2\Pi_g$ $O_2^+(v^+)$ species that are immediately dissociated by the intense UV light field, forming the detected O^+ ions.

Several other four- and higher-photon absorption processes lead to O^+ and electron production. Each multiphoton ionization / dissociation process creates these partner species with a unique speed or kinetic energy release. Velocity map imaging is an excellent means for studying these processes, and is shown in this study to provide sufficient energy resolution to identify the dissociation channel regardless of the number of photons absorbed. Furthermore, the angular distribution of the fragments provides useful information on the symmetry of the electronic states involved in the initial absorption steps. The angular distribution $I(\theta)$ is dependent on the angle θ between the laser polarization direction and the velocity of the fragments. For a stepwise two-photon dissociation this can be given by [8, 9, 10]:

$$I(\theta) \propto 1 + \beta P_2(\theta) + \gamma P_4(\theta) \tag{7.1}$$

where $P_n(\theta)$ are n^{th} order Legendre polynomials. In the high rotational (classical) limit for a rapid one-photon transition only the β parameter is incorporated. In this case β has a limiting value of 2, corresponding to a $\cos^2\theta$ distribution for a parallel transition ($\Pi \leftrightarrow \Pi$, $\Sigma \leftrightarrow \Sigma$). For a perpendicular transition ($\Pi \leftrightarrow \Sigma$) this value of β is -1 and the angular distribution resembles a $\sin^2\theta$ function. For the two-step process two parallel transitions would yield β=20/7 and γ=8/7, two perpendicular transitions yield β=-10/7 and γ=3/7, and a parallel-perpendicular combination yields β=5/7 and γ=-12/7. The angular distributions in these three limiting cases are respectively $\cos^4\theta$, $\sin^4\theta$ and $\cos^2\theta\sin^2\theta$. These limits in β and γ are used as qualitative indicators of transition symmetry in this study.

7.2 Experiment

The velocity map imaging apparatus has been described in detail elsewhere [11] so only a brief overview will be given here. A home-built piezoelectric nozzle produces a pulsed supersonic beam of pure O_2 that is skimmed and collimated then directed down the axis of a time-of-flight (TOF) mass spectrometer. The ionization / dissociation laser is focussed with a 20 cm lens onto the molecular beam and ions are extracted toward a pulsed MCP with phosphor screen detector read by a CCD camera. The 248 nm laser[4] produces a switchable pulsewidth of 5 or 0.5 ps. The laser intensity is estimated to be $\sim$5x10^{11}W/cm^2 for the 5 ps laser pulse and a factor of ten higher for the 0.5 ps laser. Obtained 2D images were inverted to 3D with an inverse Abel transformation from which the velocity and angular distributions were extracted. The kinetic energy release was calibrated by images from a study [12] of photodissociation of H_2 under the same experimental conditions, using the proportionality [13] of image size to the square root of kinetic energy, which is independent of the particle charge/mass ratio. The maximum kinetic energy release detectable is $\sim$7 eV, which is limited by the combination of the ion flight path of 45 cm and breakdown at repeller plate for voltages above 7000V. Its should be noted that the apparatus sensitivity and resolution for electron and cation imaging are identical, as has been shown in previous studies [2, 3]. The generally weak images seen for photoelectrons in this study are indicative of a lack of strong signals for electrons with less than 7 eV kinetic energy.

7.3 Results

Velocity map images of O^+ and photoelectrons produced by 248 nm irradiation of O_2 are shown in Fig. 7.1 for laser pulselengths of 5 and 0.5 psec. The concentric rings seen in the raw images are projections of 3-D Newton spheres onto the 2-D detector surface. The center part of the image, corresponding to zero-velocity fragments is especially bright and has been masked off in the displayed images. This signal is probably due to dissociative ionization and will be discussed later. The corresponding kinetic energy release (KER) distributions obtained from the Abel-inversions of the images are shown in Fig. 7.2. A number of peaks are seen in these KER distributions with spacing on the same order of magnitude as the vibrational spacing in O_2, which is $\sim$ 0.20 eV. Angular distribution parameters extracted for the stronger peaks seen in the O^+ images are listed in Table 7.1.

Assignments of the observed peaks are indicated in Figure 7.2 and will be discussed in detail in the following section. Three main channels are identified: a) Four-photon excitation followed by post-dissociative ionization (PDI). This involves the formation of $O^{**}(3s(^3P,^1P))$ atoms which autoionize, producing equal amounts of O^+ and electrons. These equal signals are used (quali-

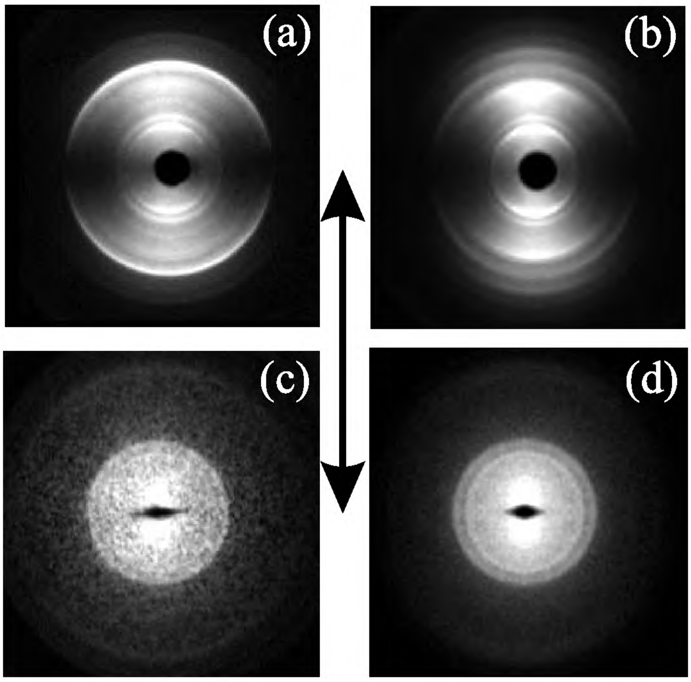

Figure 7.1: *Velocity map images of O^+ ions and electrons from O_2 photodissociation at 248 nm with laser pulselengths of 5 ps and 0.5 ps: (a) O^+ at 5 ps (b) O^+ at 0.5 ps (c) e^- at 5 ps (d) e^- at 0.5 ps. These are gray-scale images where signal strength increases from black to white. The arrow indicates the direction of the laser polarization vector. Off-scale signals with near-zero kinetic energy have been masked off.*

tatively) to scale the relative signal levels in Figure 7.2 for the ions generated by the 5 ps laser pulselength. b) Ionization following three-photon absorption, producing mainly $O_2^+(v^+=0\text{-}2)$ and the corresponding photoelectrons indicated in the electron image. c) One- and two-photon dissociation of O_2^+ $X^2\Pi_g(v^+)$ ions to the 18.733 and 20.700 eV limits, respectively, producing the main signals seen in the O^+ image. It should be noted that large amounts of O_2^+ in higher vibrational levels ($v^+=6$, for example) must be produced in order to observe the O^+ fragments from two-photon dissociation in Figure 7.2(a). These $O_2^+(v^+)$ levels cannot be the result of three-photon absorption since the corresponding photoelectron signals from the previously scaled electron KER distribution are too small. Instead, they are produced following four-photon absorption, creating photoelectrons with kinetic energies too large (> 6 eV) to fit on the detector under the present experimental conditions.

7.4 Discussion

An overview of the possible ionization / dissociation pathways when molecular oxygen is excited with intense 248 nm light is given in Figure 7.3. Potential energy curves for the electronic states of O_2 (solid lines) and O_2^+(dashed lines) are shown schematically.

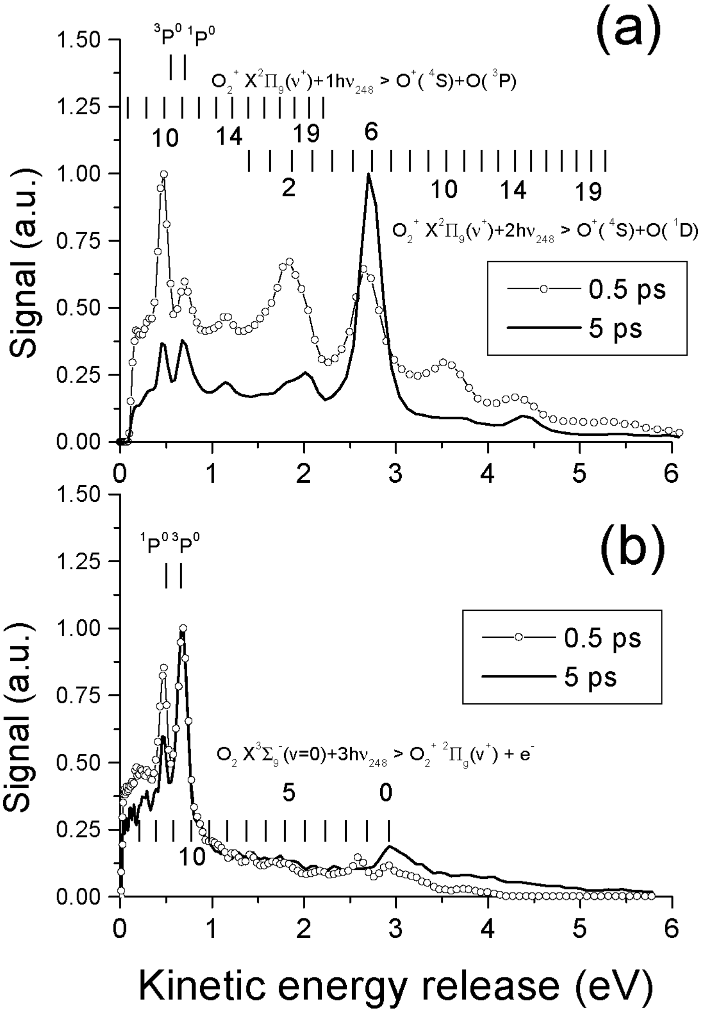

Figure 7.2: *Kinetic energy distributions for the images shown in Fig. 7.1: (a) O^+ kinetic energy spectrum for 5 ps and 0.5 ps pulses (b) e^- kinetic energy spectrum for 5 ps and 0.5 ps pulses.*

7.4.1 One-, two-, and three-photon absorption

The first photon can excite the molecule from the X$^3\Sigma_g^-$ ground electronic state into the region of high vibrational levels of the Herzberg bands, the closest lying states being the A$^3\Sigma_u^+$ (v=8) and c$^1\Sigma_u^-$(v=14). These are both exceptionally weak transitions owing to selection rule violations, and in addition, for low N states neither the A(v=8)←X(v=0) rovibronic transitions [14], nor the much weaker c(v=14)←X(v=0) rovibronic transitions [15] are in resonance with the laser energy (4.987 eV). Fluorescence is the only relaxation pathway following one-photon absorption.

Two-photon absorption brings the molecule to 10 eV and nearly resonant with the c$^1\Pi_g$ (3$s\sigma_u$) (v=8) Rydberg state [16], which is strongly predissociative, producing mainly O(^{1}D) + O(^{1}D) fragments. These neutral atom fragments are not detected in this work, but have been

Table 7.1: *Angular distributions parameters*^{a}β *and* γ *for the different dissociation / ionization pathways producing* O^+.

peak	β 5ps	γ 5ps	β 0.5ps	γ 0.5 ps
PDI (^{3}P)	1.61±0.03	0.27±0.02	1.63±0.02	0.29±0.02
PDI (^{1}P)	1.47±0.03	0.47±0.02	1.79±0.03	0.54±0.02
$v^+ = 14$ (1hν)	1.82±0.06	0.42±0.04	1.96±0.09	0.82±0.07
$v^+ = 2$ (2hν)	2.09±0.05	0.57±0.05	2.62±0.07	1.41±0.04
$v^+ = 6$	1.71±0.03	-0.27±0.05	1.84±0.06	0.05±0.06
$v^+ = 10$	2.04±0.07	0.83±0.07	2.75±0.11	1.74±0.09
$v^+ = 14$	2.06±0.09	0.67±0.09	2.35±0.13	0.88±0.09

^{a}errors represent 1σ of fitted expression

characterized in other studies [16, 17]. Dissociation is likely to be a strong quenching mechanism that competes with further absorption to higher energy levels. In fact, no ions are observed when using lower intensity nanosecond laser excitation at this wavelength.

Three-photon absorption brings the molecule above the ionization potential at 12.08 eV. Because three-photon absorption and one-photon absorption follow the same g↔u selection rules, information from optical studies at 14.96 eV could give some indication of the photophysics possible when using 248 nm light. The I' $4s\sigma_g{}^3\Pi_u$ (v=3) Rydberg state, which lies at 14.96 eV, is relatively stable compared to other states in the same energy region in that it shows rotational structure. Measurements of atomic fluorescence show that molecular Rydberg states lying in this region decay predominantly to an excited O*(3p ^{3}S ^{0}) atom, i.e., dissociation to the O(^{3}P) + O*(2p^{3}3s ^{3}S^0) channel at 14.64 eV. With the intense 5 eV photon flux present the ^{3}S^0 and lower lying ^{5}S^0 atoms will be immediately ionized. No evidence is seen for dissociation from this I' Rydberg state, which should create equal amounts of photoelectrons (0.89 and 0.52 eV KER) and O^+ (0.35 and 0.73 eV KER) for the ^{3}S and ^{5}S state, respectively. This state could act as a doorway for four-photon absorption, which is the strongest process observed.

Direct ionization or autoionization can also take place at 14.96 eV, and a small amount of production of the resulting photoelectrons is seen in Figures 7.1(c), 7.1(d) and 7.2(b), where the largest fraction of signal in this channel corresponds to v^+=0-2 (direct ionization). Autoionization producing X $^2\Pi_g$ O_2^+ vibrational levels up to v^+= 14 is also possible. Molecular (auto)ionization following three-photon absorption is a minor channel compared to other ionization processes observed in this study, in contrast to the results of studies using nanosecond lasers in the 240-193 nm region [18]. Instead, the major channel following three-photon absorption with short-pulse 248 nm radiation appears to be absorption of one additional photon.

7.4.2 Four-photon absorption

Four-photon non-resonant excitation at 248 nm, equivalent to 19.948 eV, produces the majority of the observed O^+ signal. At this energy neutral Rydberg states which converge on the $B^2\Sigma_g^-$ electronic state of the ion at 20.3 eV are present above an underlying dissociative ion-

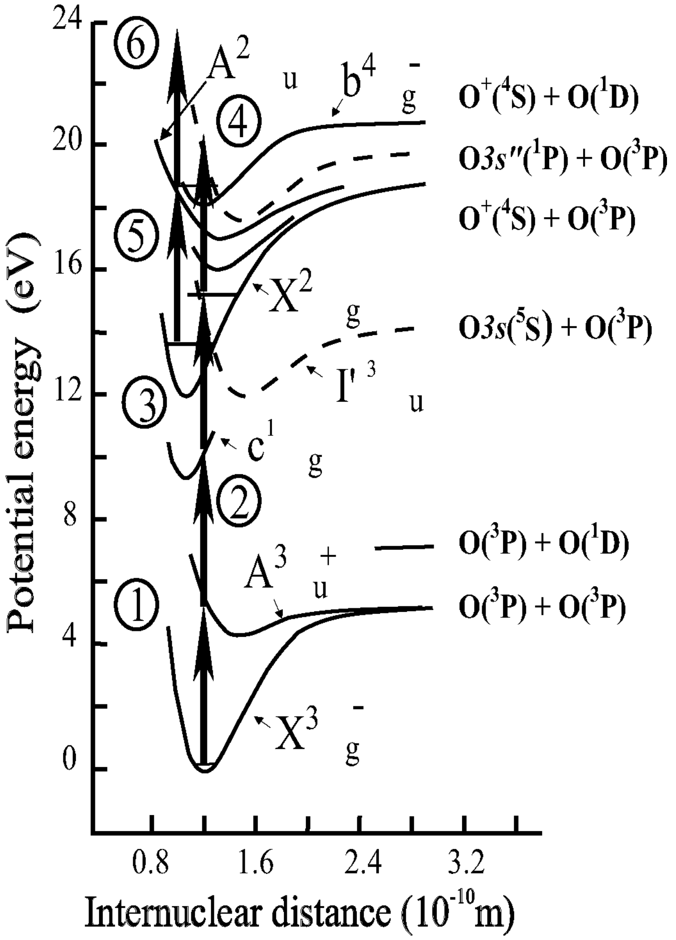

Figure 7.3: *Schematic potential energy curves of O_2 (solid lines) and O_2^+ (dashed lines) relevant to this study.*

ization continuum [19]. These Rydberg states, as studied by direct absorption, are known to decay rapidly by various processes, including direct or autoionization [20] to form $O_2^+(X^2\Pi_g$, and $b^4\Sigma_g^-)$ electronic states [21], or dissociate to a range of $O(^3P, ^1D$, or $^1S)$ atoms with electronically excited atomic partners $O^*(2p^3,nl)$, some of which have been detected by fluorescence [22]. No strong evidence is seen in this study for production of O* atoms following four-photon absorption. Several groups have found that the dominant channel forming O^+ at 20 eV is post dissociative ionization [23, 24, 25] (PDI) due to the process $O_2 \rightarrow O_2^* \rightarrow O + (O^{**} \rightarrow O^+ + e^-)$. These O** species are excited atoms with energies above the first atomic ionization potential and will rapidly autoionize to the lower lying ^4S continuum, producing equal amounts of O^+ and electrons.

In both electron and ion spectra at relatively low kinetic energy release two distinct peaks are seen that can be assigned to the production O^3P and O**(^3P and ^1P), with thresholds at 19.15 and 19.45 eV. These highly excited O** atoms have 0.72 and 0.48 eV KER and autoionize, yielding 0.50 eV and 0.75 eV photoelectrons. One-photon studies by Wills *et al.* [26] found that equal amounts of 3p'(^1P,^3D,^3F) and 3s"(^1P,^3P) atoms are formed at 20 eV. In this study, employing four-photon excitation, only the 3s"(^1P,^3P) atoms are observed.

A dissociative ionization continuum is also present in the 20 eV energy region. The kinetic energy release in the O atom fragments ($O^+(^4S^0)+O(^3P)$ at 18.733 eV) will be near zero in this case, with a width reflecting the width of the O_2 ground state vibrational wavefunction. The intense zero energy signal, which has been masked off in the images shown in Fig. 7.1, is likely due to dissociative ionization. The kinetic energy of the photoelectrons in this process will form a continuous distribution at low energies and may account for the rise in the baseline seen in the KER distribution of Fig. 7.2(b).

Autoionization to form higher vibrational levels of the O_2^+ $b^4\Sigma_g^-$ electronically excited state has also been indicated in measurements of O^+ KER at 20 eV by Erman *et al.* [27]. Vibrational levels above v^+=4 in this state are highly predissociative to the $O^+(^4S^0)+O(^3P)$ limit at 18.733 eV. Some of the low energy, unresolved structure in the O^+ and e^- KER distributions could also be due to this process, but it should be noted that no strong signal in the photoelectron image corresponding to formation of O_2^+ $b^4\Sigma_g^-$ in v^+=0-4 is observed. These signals are very strong in the one-photon excited photoelectron KER distributions reported by Wills *et al.* [26].

Autoionization to the O_2^+ $X^2\Pi_g$ ground state following four-photon excitation, which is then followed by one and two-photon dissociation of the same species, is responsible for the largest fraction of the O^+ signal. Wills *et al.* [26] also observed this autoionization process at 20 eV excitation energy. In this case the photoelectrons created have kinetic energies higher than the photon energy. Note that O_2^+ $X^2\Pi_g(v^+ > 14)$ can only be produced by four-photon ionization. Electrons corresponding to X state vibrational levels with $v^+ > 17$ created by four-photon excitation have kinetic energies above the maximum measurable value in the photoelectron image. This process is above-threshold ionization (ATI) [7] and has been observed in studies [1] involving very high intensity laser fields ($I > 10^{13}$W/cm^2). The laser intensity is lower in this experiment and other high-field effects such as double ionization [28] are not observed. Apparently, (auto)ionization is particularly slow at the three-photon level compared to photoabsorption at 15 eV, allowing the occurrence of ATI.

Inspection of the O^+ KER distributions for photodissociation of O_2^+, discussed in the next section, indicates that autoionization following four-photon excitation produces O_2^+ $X^2\Pi_g(v^+)$ in a wide vibrational distribution with peaks at v^+ = 2, 6, 10, 14, and 19. Autoionization from a Rydberg state in the v=4 vibrational level would give this nodal Franck-Condon pattern. The n=5,v=4 $p\sigma_u{}^3\Sigma_u^-$ state converging on the $B^2\Sigma_g^-$ state lies at ~19.95 eV in the one-photon spectrum [29], but unfortunately nothing is known of the two-photon allowed Rydberg states that should fall in the same energy region.

Summarizing, of the many processes possible after excitation to 20 eV, autoionization to the $X^2\Pi_g$ state, dissociative ionization, post-dissociative ionization to form (3s"(^3P,^1P) atoms), and possibly autoionization followed by predissociation of O_2^+ b $^4\Sigma_g^-(v^+ > 4)$ are observed, in descending order of importance. Quite striking is that very little signal is seen for the photoelectrons from three-photon ionization while the O^+ signal indicates formation of copious amounts of vibrationally excited O_2^+. The sensitivity and resolution of the apparatus is sufficient to observe electrons from three-photon ionization, and the electron: O^+ signal strengths are reliably scaled using the two PDI peaks for O^+ and electrons. From this scaling it is apparent that the electron signal for O_2^+ X($^2\Pi_g$) formation is much less than the signal corresponding to O_2^+ X($^2\Pi_g$) dissociation. This discrepancy is due to four-photon ionization (ATI) producing photoelectrons with energies $>$ 7 eV that are undetectable for our setup.

7.4.3 Photodissociation of O_2^+ $X^2\Pi_g$

Molecular oxygen ions subjected to intense 248 nm laser radiation can also absorb one or more photons during the laser pulselength. Using 5 eV photons, O_2^+ ions in vibrational levels higher than v^+=7 can directly photodissociate to the 18.733 eV limit producing O(^{3}P)+O^+(^{4}S) ions. This pathway is labeled in Fig. 7.2(a) for levels v^+=8-20, where v^+=15-20 can only be produced by four-photon dissociation.

Vibrational states lying lower than v^+=8 can form O^+ by two-photon dissociation, with the first photon inducing bound-bound transitions via the allowed $A^2\Pi_u \leftarrow X^2\Pi_g$, the so-called second negative system [30]. Transitions can take place through the A state continuum or through bound levels of other higher-lying states. The ground state of the oxygen molecular ion is $^2\Pi_g$ so any upper state with $(^2\Sigma,^2\Pi,^2\Delta)_u$ symmetry is a candidate. Molecules excited to the upper state can then absorb a second photon and dissociate, producing O^+ ions. Resonance enhanced two-photon dissociation of O_2^+ $X^2\Pi_g(v^+)$ at 248 nm provides enough energy to make O^+(^{4}S)+O(^{3}P,^{1}D) and O^+(^{2}D)+O(^{3}P,^{1}D) products. The remaining O^+ peaks in the spectrum can be explained by two-photon dissociation of O_2^+ $X^2\Pi_g$ (v^+) molecules to the O^+(^{4}S)+O(^{1}D) dissociation limit at 20.700 eV, with particularly strong signals corresponding to dissociation of v^+= 2, 6, 10, 14, and 19. Dissociation to the 18.733 eV limit is not observed following two-photon dissociation.

Interesting differences are observed in the O^+ KER distributions for 0.5 and 5 ps pulses. A very strong enhancement of the v^+= 6 two-photon dissociation peak is seen when using the 5 ps pulse, while (relative to the PDI signals) the v^+=2 and v^+=10 peaks stand out in the two-photon dissociation channel for 0.5 psec pulses. The v^+=10 peak, which overlaps the $^3P^0$ PDI peak in the one-photon dissociation channel, also appears to be enhanced with 0.5 ps pulses. This suggests that the enhancement (for v^+=10 at least) arises in the neutral O_2 four-photon excitation instead of the competition between one and two photon dissociation of O_2^+.

Near-resonance enhancement of the A $\leftarrow$ X(v^+=2,v^+=6) transitions is also possible with 248 nm photons. Using the spectroscopic constants from Prasad *et al.* [31] or Akohori *et al.* [32] we find that the (5'-2") and (17'-6") transitions are nearly resonant with one 248 nm photon. This is only for the higher spin-orbit $^2\Pi_{g3/2}$ state, this state is known to be the favored state by autoionization [33]. Unfortunately, consistent and accurate rotational constants are not available for the higher vibrational levels of the A state, thus a quantitative comparison is not possible. Ignoring rotation, the (5'-2") transition lies closer to the laser wavelength than the (17'-6") transition, but, considering the high laser field strength, the A $\leftarrow$ X transitions are likely to be shifted into and out of resonance due to the AC Stark effect [34]. The differences between the 0.5 and 5 ps pulses are thus likely to be due both to the multiphoton pathway for production of O_2^+ and to resonance effects in the O_2^+ A$\leftarrow$X transitions.

Only the $O^+(^4S)$+$O(^1D)$ limit is observed to be active following two-photon excitation of O_2^+. This limit correlates only molecular electronic states with quartet spin symmetry, while it could be expected that the initial optically excited state is a doublet state, like the X and A electronic states of O_2^+. Photodissociation of $a^4\Pi_u(v^+)$ states directly accesses this limit [17], but no evidence is seen for $a^4\Pi_u$ production in the photoelectron image, and the KER is not correct for $a^4\Pi_u$ state photodissociation. Electronic curve crossing after excitation of the X state thus must take place very efficiently to the nearest dissociation limit, an effect that is often observed in the dissociative ionization of neutral O_2. Only a few studies have been reported [35] on the photodissociation of O_2^+, and these have been limited to predissociation to the first dissociation limit.

7.4.4 O^+ angular distributions

Angular distributions also reveal information on the photophysics. While the quality of the electron images is not sufficient to extract angular distribution parameters, the O^+ images do yield meaningful data, presented in Table 7.1. Both β and γ are needed to simulate the measured O^+ angular distributions. The overall trends resemble a parallel-parallel two-step transition with β near the limiting value of 20/7 and γ near 8/7. This suggests that the two-step absorption terminates at a $^2\Pi_g$ state after excitation through the $A^2\Pi_u$ state. Curve crossing to a quartet state correlating with the 20.700 eV limit then takes place. Even the one-photon dissociation angular distribution of the $X^2\Pi_g(v^+=14)$ presented in Figure 7.4(a) needs a two-photon angular distribution fit, however. In addition, the maximum value of γ=8/7 is exceeded in the 0.5 ps case with two-photon dissociation for the $X^2\Pi_g(v^+=2$ and 10) states shown in Figure 7.4(b) and 7.4(c). These results suggest that other effects have to be incorporated. One of these effects can be axis alignment of the formed O_2^+ by the multiphoton excitation of the neutral O_2. The rotational period of O_2 is in the order of ps and similar to the laser pulselengths, thus alignment anisotropy can be diminished, but not eliminated by the rotation of the O_2^+ parent ion.

Another possible effect causing alignment is the interaction of the strong electric laser field with molecule causing an induced dipole moment. This induced dipole moment creates pendular states, where libration of the molecular axis about the electric field vector is aligning the molecules with respect to the laser polarization [36]. This effect is more profound with higher laser intensity and this is also seen in Figures 7.4(a), 7.4(b) and 7.4(c), where the 0.5 ps angular distributions are more anisotropic than the 5 ps case. We have also seen these effects with the 248 nm shortpulse photodissociation of CH_3I [3] and therefore conclude again that this effect will also need to be accounted for in interpreting the product angular distributions.

Finally, the results of Walker *et al.* [1] for photodissociation / ionization of O_2 at 532 and 355 nm can be compared with the present results. In their study laser fields in the 10^{11-13} W/cm^2 range were employed and photoelectron kinetic energy distributions were measured. For 532 nm photons these authors found that the vibrational distribution for formation of O_2^+ varied with laser intensity. This was ascribed to three competing processes: direct 6-photon ionization, 5-photon resonance enhanced 1-photon ionization via a high Rydberg state converging on the ionic ground state, and 5-photon resonance enhancement with a mixed valence state followed by 2-photon ATI. In the present study less intense laser fields are used and the higher photon energy allows resonance enhancement to take place at the three- and four-photon level.

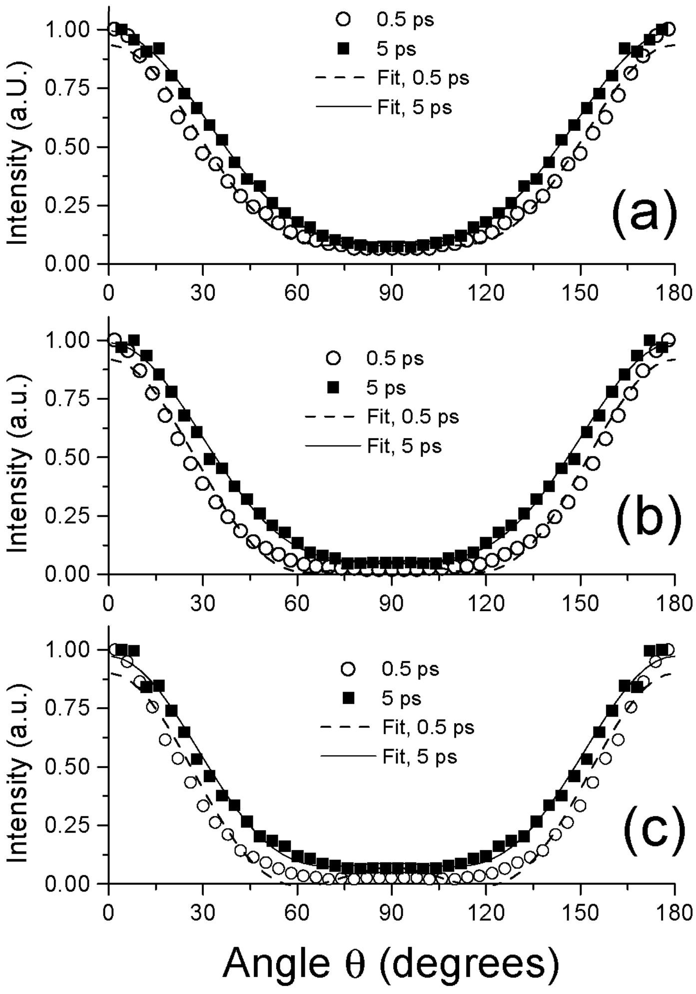

Figure 7.4: *Angular distributions for O^+ photofragments with 0.5 ps and 5 ps laserpulses and fits for different peaks of Figure 7.3 and Table 7.1: (a) $v^+=14$ (1hν), (b) $v^+=2$ (2hν), (c) $v^+=10$ (2hν).*

7.5 Conclusions

The main events seen in this experiment can be attributed to absorption of four 248 nm photon from the ground state of O_2. One distinguishable process is the photodissociation of highly excited Rydberg states that produce groundstate atoms O^3P and highly excited oxygen atoms 3s"^{1}P and 3s"^{3}P. These highly excited atoms autoionize towards the ionic atom ground state $O^+(^4S)$ and produce equal amounts of electrons and O^+ ions with a specified kinetic energy.

Another important pathway is autoionization into vibrational levels of the $X^2\Pi_g$ground state molecular ion. No signal is seen in the electron and ion signal that suggests autoionization to the higher ionic states $a^4\Pi$, $b^4\Sigma_g^-$ and $B^2\Sigma_g^-$. Also, only very small signals are seen for three-photon ionization processes. The kinetic energy spectra suggest that the ions are formed mainly in the vibrational states $X^2\Pi_g$ (v^+ = 2,6,10,14,19) which subsequently photodissociate in two pathways. The first pathway is one-photon dissociation towards the $O^+(^4S)+O(^3P)$ limit for levels $v^+ > 7$, the second pathway is two-photon dissociation towards the $O^+(^4S)+O(^1D)$ limit. This pathway shows enhancement for the $v^+=2$ signal for 0.5 ps and $v^+=6$ for 5 ps, that could be explained by possible resonances with ro-vibrational levels of the $A^2\Pi_u$ state.

The angular distributions of all the products tend towards the maximum possible anisotropy. The values of $\beta \approx 2$ and $\gamma \approx 1$ suggest that the two-photon dissociation of the $X^2\Pi_g(v^+)$ states occurs via the $A^2\Pi_u$ state to a $^2\Pi_g$ upper state. Alignment of the molecules by the photo-preparation steps and by the interaction with the strong laser light field is also indicated.

Acknowledgments

The authors thank Mr. Apostolis Egglezis for expert maintenance of the fs-ps KrF laser system. This work was done at the Ultraviolet Laser Facility at FORTH-IESL (TMR, Access to Large Scale Facilities EU program, Contract No. ERBFMGECT 950021) and was also supported by TMR Network *IMAGINE* ERB 4061 PL-97-0264 and the Stichting FOM.

References

[1] B. Walker, M. Saeed, T. Breeden, B. Yang and L.F. DiMauro, Phys. Rev. A **44**, 4493 (1991).
[2] T. Gougousi, P.C. Samartzis and T.N. Kisopoulos, J. Chem. Phys. **108**, 5742 (1998).
[3] P.C. Samartzis, B.L.G. Bakker, D.H. Parker, and T.N. Kitsopoulos, J. Phys. Chem. A **103,** 6106 (1999).
[4] F.P. Schafer and S. Szatmari, Optics Comm. **68**, 196 (1988).
[5] A.G. Suits, R.L. Miller, L.S. Bontuyan, and P.L. Houston, J. Chem. Soc. Farad. Trans. II **89**, 1443 (1993).
[6] A.T.J.B Eppink and D.H. Parker, Rev. Sci. Instrum. **68**, 3477 (1998).
[7] P. Agostini, F. Fabre, G. Mainfray, G. Petite, and N.K. Rahman, Phys. Rev. Lett. **42**, 1127 (1979).
[8] R.N. Zare, Mol. Photochem. **4**, 1 (1972).
[9] K. Chen and E.S. Yeung, J. Chem. Phys. **72**, 4723 (1980).
[10] R.K. Sanders and K.R. Wilson, J. Chem. Phys. **63**, 4242 (1975).
[11] P.C. Samartzis, B.L.G. Bakker, T.P. Rakitzis, D.H. Parker and T.N. Kisopoulos, J. Chem. Phys. **110**, 5201 (1999).
[12] B.L.G. Bakker, D.H. Parker, P.C. Samartzis and T.N. Kitsopoulos, work in progress.
[13] A.T.J.B. Eppink, B. Bakker and D.H. Parker, SPIE Vol. **3271**, 177 (1998).
[14] D.L. Heustis, R.A. Copeland, K. Knutsen, T.G. Slanger, R.T. Jongma, M.G.H. Boogaarts, G.Meijer, Can. J. Phys. **72**, 1109 (1994).
[15] K. Yoshino, J.R. Esmond, W.H. Parkinson, A.P. Thorne, R. C. M. Learner, and G. Cox, J. Chem. Phys. **111**, 2960 (1999).
[16] W.J. van der Zande, W. Koot, J. R. Peterson, J. Los, Chem. Phys. Lett. **140**, 175 (1987).
[17] B.L.G. Bakker, A.T.J.B. Eppink, and D.H. Parker, work in progress.

[18] D.H. Parker and A.T.J.B. Eppink, J.Chem. Phys. **107,** 2357 (1997); B.L.G. Bakker and D.H. Parker, work in progress.
[19] P.M. Dehmer and W.A. Chupka, J. Chem. Phys. **62**, 4525 (1975).
[20] A. Tabche-Fouhaile, I. Nenner, P. Guyon and J. Delwiche, J. Chem. Phys. **75,** 1129 (1981).
[21] A.A. Cafolla, T. Reddish, A.A. Wills, and J. Comer, J. Phys. B **23**, 1433 (1990).
[22] M. Ukai, N. Kouchi, K. Kameta, N. Terazawa, Y. Chikahiro, Y. Hatano and K. Tanaka, Chem. Phys. Lett. **195,** 298 (1992).
[23] A.A. Cafolla, T. Reddish and J. Comer, J. Phys. B **22**, L273 (1989).
[24] A.A. Wills, A.A. Cofolla and J. Comer, J. Phys. B **24**, 3989 (1991).
[25] M. Ukai, S. Machida, K. Kameta, M. Kitajima, N. Kouchi, Y. Hatano and K. Ito, Phys. Rev. Lett. **74**, 239 (1995).
[26] A.A. Wills, A.A. Cofolla and J. Comer, J. Phys. B **24**, 3989 (1991).
[27] P. Erman, A. Karawajcyk, E. Rachlew-Kallne, M. Stankiewicz and K. Yoshiki Franzen, J. Phys. B **29**, 5785 (1996).
[28] C. Gou, M. Li, J.P. Nibarger, and G.N. Gibson, Phys. Rev. A **58**, R4271 (1998).
[29] D.M.P Holland, D.A. Shaw, S.M. McSweeney, M.A. MacDonald, A. Hopkirk and M.A. Hayes, Chem. Phys. 173, 315 (1993).
[30] P.H. Krupenie, J. Phys. Chem. Ref. Data **1**, 423 (1972).
[31] C.V.V. Prasad, D. Lacombe, K. Walker, W. Kong, P. Bernath and J. Hepburn, Mol. Phys. **91**, 1059 (1997).
[32] T. Akahori, Y. Morioka, T. Tanaka, H. Yoskii, T. Hayaishi and K. Ito, J. Chem. Phys. **107**, 4875 (1997).
[33] K. Ellis, R. Hall, L. Avaldi, G. Dawbert, A. McConkey, L. Andric and G. C. King, J. Phys. B **27**, 3415 (1994).
[34] M.A. Quesada, A.M.F. Lau, D.H. Parker, and D.W. Chandler, Phys. Rev. A **36**, 4107 (1987).
[35] J.C. Hanssen, M.M. Graff, J.T. Moseley, P.C. Cosby, J. Chem. Phys. **74**, 2195 (1981).
[36] B. Friedrich and D. Herschbach, Phys. Rev. Lett. **74**, 4623 (1995).

Chapter 8

Multiphoton dynamics of H_2 with 248 nm picosecond and femtosecond pulses

Abstract

Non-resonant excitation of H_2 at 248 nm using 5 ps and 0.5 ps laser pulses with intensities 5×10^{11} W/cm^2 and 5×10^{12} W/cm^2, respectively, is studied by measurement of the angle-speed distributions of the H^+photofragment using velocity map imaging. Three main H^+ production channels are observed: a) three-photon dissociation to H(n=1) + H(n=2) followed by photoionization of H(n=2); b) dissociative (auto)ionization following four-photon absorption to form H(n=1) + H^++ e^- and; c) autoionization from a doubly excited state producing an H_2^+ vibrational distribution peaking at (v^+=2,7,13) and subsequent photodissociation of these vibrationally excited ions. In the neighborhood of the energy sum of three 248 nm photons lie transitions to the B' $^1\Sigma_u^+(3p\sigma)$ vibrational continuum and the two bound states B" $^1\Sigma_u^+(4p\sigma)$ (v=2) and D $^1\Pi_u^+(3p\pi)$ (v=4). These states are believed to play an important role in three-photon absorption and at the subsequent fourth photon level. Their effect on the observed kinetic energy and angular distributions is discussed.

8.1 Introduction

Laser ionization is a general and informative means of studying the interaction of molecules with high intensity light fields and a prime detection method for probing nascent species. In fact, as the laser intensity increases Multi Photon Ionization (MPI) becomes the dominant process. As the simplest molecules, H_2 and H_2^+ are good test cases for understanding MPI. Furthermore, short-pulse, intense laser light is becoming increasingly popular as a 'universal' ionization source, i.e., a source that ionizes with equal efficiency all internal states of the target molecule. Ideally, MPI should produce only the parent molecule ion, but in practice this is not always the case. To investigate these concepts we have studied the MPI/dissociation process for H_2 using short pulse UV light at 248 nm. This wavelength is not directly resonant with any bound states of the neutral or ion, even for multiphoton absorption. Several studies of H_2 MPI at 248 nm [1, 2], 390/780 nm [3], 532/527 nm [4] and 600 nm [2] have been reported and also at 532 nm in D_2 [5], mostly at intensities above 10^{14}W/cm^2, where ATD, ATI, bond-softening, and other higher-order effects take place. These effects also occur during the interaction of intense laser light with the product hydrogen ion H_2^+ [6]. In this study intensities below 10^{14}W/cm^2 are used, in the range where significant H_2^+ and H^+ production is observed, but where the more exotic effects are not expected.

The photodynamics of the hydrogen molecule are special due to the existence of well-characterized doubly-excited repulsive states, which have been described in detail by Guberman [7]. These states determine the decay pathways of the stable singly excited Rydberg states: the hydrogen molecule can dissociate into neutrals or autoionize. If the hydrogen molecule is excited above the $^2\Sigma_u^+$ ionic dissociation limit at 18.07 eV above the ground state another important decay pathway is possible, namely dissociative ionization. This process fragments H_2 into three products: H(n=1) + H^+ + e^-. The photodynamics of hydrogen is therefore not straightforward and extensive investigations have been reported on the dynamical behavior of the H_2 double excited states. Most of the experiments are done by MPI via a resonant intermediate state, i.e., by Resonance Enhanced Multi Photon Ionization (REMPI). The choice of the intermediate resonant state often determines which final state will be excited. The dynamics of this final excited state can be examined. Several groups have reported REMPI via the states B $^1\Sigma_u^+$ [8, 9, 10, 11, 12, 13, 14, 15] C $^1\Pi_u$ [9, 16, 17, 18, 19], EF$^1\Sigma_g^+$ [20, 21, 22, 23, 24, 25] B' $^1\Sigma_u^+$ [25, 26], B" $^1\Sigma_u^+$ [25], D $^1\Pi_u$ [25, 26]. Most relevant to the present work are experimental studies by Rottke *et al.* [13] of (3+2) REMPI via the B $^1\Sigma_u^+$ state and by Buntine *et al.* [25] of (1+1) REMPI ion-imaging studies via the B" $^1\Sigma_u^+$ and D $^1\Pi_u$states, starting from the E,F $^1\Sigma_g^+$state.

The method used in this experiment "velocity map imaging" [27] is an excellent means for studying photodissociation processes. It provides not only the kinetic energy of the formed fragments but also their angular distributions with respect to the laser polarization. The kinetic energy resolution (~20 meV at 1 eV) is sufficient that different dissociation pathways can usually be identified regardless of the number of photons absorbed. The angular distribution I(θ) is dependent on the angle θ between the laser polarization direction and the velocity of the fragments. This obtained angular distribution I(θ) reveals the symmetry of the electronic states involved in the initial photon steps. For a stepwise N-photon dissociation this can be given by [28, 29, 30]:

$$I(\theta) \propto 1 + \sum_{n=2,4,..}^{n=N} \beta_n \cdot P_n(\cos\theta) \tag{8.1}$$

where $P_n(\theta)$ are n^{th} order Legendre polynomials For a two-step process two parallel transitions result in β_2=20/7 and β_4=8/7, two perpendicular transitions gives β_2=-10/7 and β_4=3/7, and a parallel-perpendicular combination can be described by β_2=5/7 and β_4=-12/7. The angular distributions in these three limiting cases are respectively $\cos^4\theta$, $\sin^4\theta$ and $\cos^2\theta\sin^2\theta$.

In case of a one photon transition β_4=0 and β_2 has a limiting value of 2, giving a $\cos^2\theta$ distribution for a parallel transition ($\Pi \leftrightarrow \Pi$, $\Sigma \leftrightarrow \Sigma$). For a perpendicular transition ($\Pi \leftrightarrow \Sigma$) this value of β_2 is -1 and the angular distribution is a $\sin^2\theta$ function. If the measured β_2 has a value in between these two extreme values then a mixture in symmetry of the transitions has occurred. Another possibility for non-extreme β_2 values is the washing out of anisotropy due to rotation of the excited state before dissociation.

If a single electronic state is excited and the parent molecule angular rotational period T is similar to the lifetime τ of the excited state, less extreme values in β are expected. The anisotropy parameter is given by the classical (high J state) formula:

$$\beta_{||}(\tau) = 2 \cdot \frac{(\tau/T)^2+1}{4(\tau/T)^2+1} \tag{8.2}$$

for a parallel transition and

$$\beta_{\perp}(\tau) = -1 \cdot \frac{(\tau/T)^2+1}{4(\tau/T)^2+1} \tag{8.3}$$

for a perpendicular transition. The slow dissociation limiting values for these anisotropy parameters are $\beta_{2||}$ = 0.5 and $\beta_{2\perp}$= -0.25. Measurement of β for each channel thus provides information on the symmetry of the electronic states involved in the absorption process and their lifetimes with respect to rotation.

8.2 Experimental

The velocity map imaging apparatus has been described in detail elsewhere [31] so only a brief overview will be given here. A piezoelectric driven nozzle produces a pulsed supersonic beam of pure H_2 that is skimmed and collimated then directed down the axis of a time-of-flight (TOF) mass spectrometer. The excitation laser is focussed with a 19 cm lens onto the molecular beam and ions are extracted toward a pulsed MCP with phosphor screen detector read by a CCD camera. The 248 nm laser [32] produces a selectable pulsewidth of 5 or 0.5 ps. The laser intensity is estimated to be 5×10^{11}W/cm^2 for the 5 ps laser pulse and a factor of ten higher for the 0.5 ps laser. The obtained 2D images were inverted to 3D with an inverse Abel transformation from which the velocity and angular distributions were extracted. It was not possible to obtain electron images in this experiment due to an overwhelming background signal due presumably to pump oil.

8.3 Results and Discussion

8.3.1 Multiphoton dynamics

The energy of one 248 nm photon is greater than the binding energy (4.48 eV) of the $X^1\Sigma_g^+$ ground state of H_2, but far too low in energy to reach the repulsive $b^3\Sigma_u^+$ state. The Franck-Condon factors for a one-photon transition to the dissociation continuum are expected to be zero. Two-photon absorption is also non-resonant with bound states of H_2, and transition to the $b^3\Sigma_u^+$ repulsive state is forbidden due to $g \leftrightarrow g$ and $\Delta S=0$ selection rules. Only by absorption of three 248 nm photons are the regions of bound and continuum states accessible in H_2, as seen in Figure 8.1. This three-photon energy, 14.96 eV, exceeds the binding energy of states correlating with the H(n=1) + H(n=2) dissociation limit, at 14.68 eV. While no bound states fall at exactly the three-photon energy, bound-free transitions to the repulsive inner wall (vibrational continuum) of lower-lying bound states such as $B^1\Sigma_u^+$ (2pσ) $B'^1\Sigma_u^+$ (3pσ) or $C^1\Pi_u$ (2pπ) could then produce H(n=2) atoms which will be immediately ionized in the strong laser fields, forming electrons, and H^+ atoms with 0.28 eV total kinetic energy release.

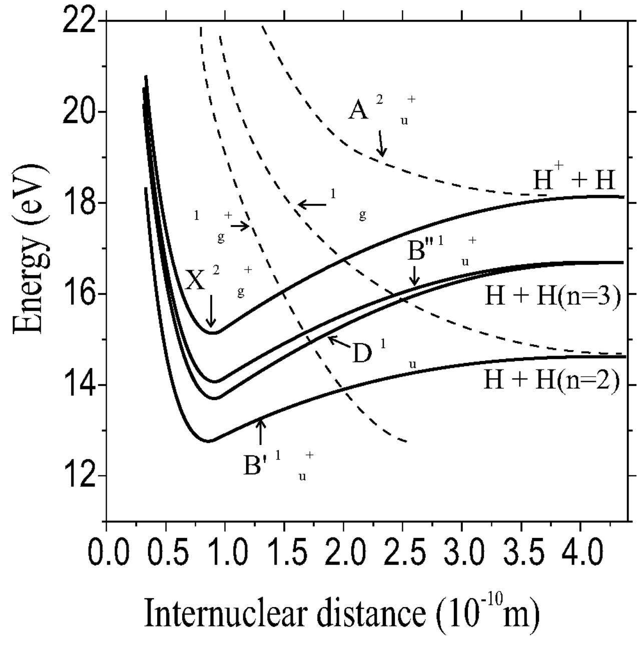

Figure 8.1: *Schematic potential energy diagram of the electronic states of H_2 and H_2^+ relevant for this study.*

This three-photon transition can also be nearly resonant with a bound Rydberg state of H_2. A three-photon bound-bound transition is similar to a one-photon transition regarding selection rules of electronic state parity and spin multiplicity. Starting from the molecular hydrogen ground state X $^1\Sigma_g^+$ one would expect the final state to be of $^1\Sigma_u$ or $^1\Pi_u$ symmetry. The parity selection rule $+ \leftrightarrow -$ is less strict, as confirmed in previous experiments using (3+1) REMPI via the B

[8, 9, 10, 11, 12, 13, 14, 16], B' [25, 26] and B" [25] states. This is similar for transitions to a $^1\Pi_u^+$ or $^1\Pi_u^-$ state, but it is noted that these different parity states show different behavior in dissociation and ionization dynamics [26]. The equivalent three-photon final state at 14.96 eV of H_2 can be compared with the XUV one-photon studies by Arai *et al.* [33] and Glass-Maujean *et al.* [34]. The high-resolution absorption spectra of Glass-Maujean *et al.* [34] show different rotational transitions to the $D^1\Pi_u$(v=4) and the $B"^1\Sigma_u^+$(v=2) state in the 14.96 eV region. Also, these two states are seen in the Lymann-α fluorescence excitation spectrum, which shows that they also pre-dissociate to the nearby H(n=1)+H(n=2) dissociation limit. Predissociation of Rydberg states of H_2 in this energy region has been analyzed in detail by Gao [35] using multichannel quantum defect theory.

Absorption of another photon, making it a (3+1) REMPI process, or non-resonant absorption of four 248 nm photons from the ground state, brings the molecule well above the ionization threshold (IP=15.5 eV). In this case several H^+ production processes are possible including direct ionization or excitation into double excited states. Two important double excited states for this study, $^1\Sigma_g^+$ and $^1\Pi_g$ are also shown in Fig. 8.1. The molecule can decay in the double excited state [36] via the processes of autoionization forming $H_2^+(v^+)$ and electrons, or dissociate to neutral fragments H(n=1) + H(n=2-∞), or undergo indirect dissociative ionization yielding H(n=1) + H^+ + e^- . The final process is possible because the photon energy of 19.95 eV is high above the ionic dissociation limit at 18.07 eV. Dissociative ionization yields protons with kinetic energy in the energy region 0-1.9 eV. These H^+ ions are expected to have a continuous energy distribution due to the three-body decay. This in contrast with the neutral dissociation that produces protons with discrete energies corresponding to the different n excited states of the H(n) atom. These discrete levels for H(n>1) result in H^+ kinetic energies in the energy region of 1.9-5.3 eV since any H(n>1) excited atoms produced by neutral dissociation will be immediately ionized by the intense laser field. Another possible production mechanism for n>1 H atoms is absorption at the fourth photon level to the vibrational continuum of high n Rydberg singly excited states in the four-photon (~20 eV) energy region [37].

In the present experiment it is difficult to determine how much H_2^+ is being formed by four-photon absorption. H_2^+ will appear mainly as a product H^+ ion due to photodissociation by the 248 nm photons, since the photon energy (4.987 eV) is larger than the H_2^+ bond energy of 2.65 eV. One-photon dissociation would produce H^+ in the 2.3-5 eV range of total kinetic energy release. Two-photon dissociation of H_2^+ would produce highly energetic H^+ atoms with kinetic energy exceeding our range of detection (7.3-10 eV). Two-photon dissociation is unlikely due to the lack of suitable final states at 10 eV for H_2^+.

8.3.2 Results

Velocity map images of H^+were taken using 5 ps and 0.5 ps pulses. Both images are very similar in appearance, thus only the 0.5 ps image is presented in Figure 8.2. Kinetic energy distributions (total energy release) from the 0.5 ps and 5 ps measurements are plotted in Fig. 8.3. Three main dissociation pathways are identified in the kinetic energy distribution.

The first channel is the three-photon dissociation of molecular hydrogen into H(n=1)+H(n=2). The second is the 4-photon dissociative ionization producing an energy continuum of protons

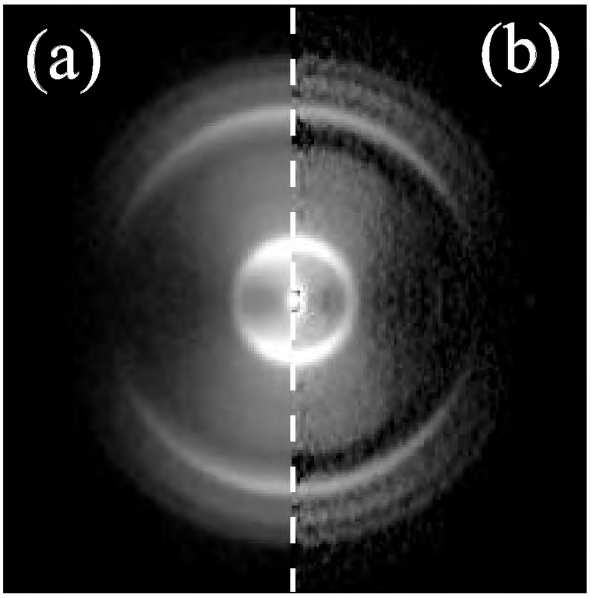

Figure 8.2: *Raw image (a) and inverted image (b) for 248 nm photodissociation of H_2 at 0.5 ps.*

with a cutoff at 1.9 eV corresponding to the four-photon energy minus the first dissociation limit of the hydrogen ion at 18.07 eV. The final observed pathway is one-photon dissociation of vibrational excited product molecular hydrogen ions. These signals arise from a vibrational distribution of ions peaking in the v^+=2,7,13 states. This means that the process of (auto)-ionization towards the distribution of vibrational states was a precursor for this last proton signal. Furthermore, there is no four-photon excitation resulting in neutral dissociation to n>1 H atoms seen in Fig. 8.3. It is also noted that no signal (due to non-resonant ionization of H(n=1)) is seen from dissociation at the one- and two-photon energy level.

Direct ionization following non-resonant four-photon excitation may be expected to produce a broad $H_2^+(v^+)$ Franck-Condon distribution peaking at v^+=2, similar to that from a He I (21.22eV) source. The fact that dissociative ionization and a multi-peaked $H_2^+(v^+)$ non-Franck-Condon distribution is seen indicates that an intermediate state at the three-photon level is important in determining H_2 multiphoton excitation at 248 nm.

8.3.3 Three photon intermediate level

Goa [35] has described the H_2 Rydberg states and their predissociation characteristics in the studied three-photon energy region. The major interaction is the coupling of the B' $^1\Sigma_u^+$ vibrational continuum with the B"$^1\Sigma_u^+$ and D$^1\Pi_u^+$ Rydberg states. According to the XUV one-photon spectra of Glass-Maujean *et al.* [34] and Arai *et al.* [33] transitions to two states, the B" $^1\Sigma_u^+$ (v=2) and the D$^1\Pi_u^+$ (v=4), lie in the energy region of the three photon level. These states predissociate to the second (H(n=1) + H(n=2)) dissociation limit, so this is consistent with the main observation of a three-photon dissociation towards this limit. The one-photon selection rules for the XUV spectra yield only P, Q and R rotational lines. However, in the three-photon case more rotational transitions are possible. The transition to the D$^1\Pi_u^+$ state from the X $^1\Sigma_g^+$ ground state

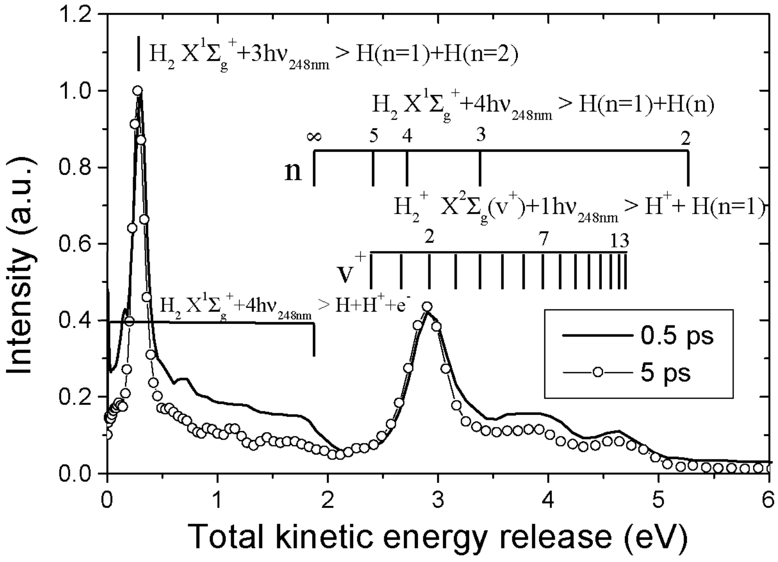

Figure 8.3: *Total kinetic energy release distributions of 248 nm photodissociation of* H_2.

yield N, O, P, Q, R, S and T branches while the transition B”$^1\Sigma_u^+$ $\leftarrow\leftarrow\leftarrow$X$^1\Sigma_g^+$ yield N, P, R and T lines. It also has been shown by Pratt *et al.* [26], that the strongest branches are the P, Q and R for the D$^1\Pi_u^+$ $\leftarrow\leftarrow\leftarrow$X$^1\Sigma_g^+$ and the P and R for the B’$^1\Sigma_u^+$ $\leftarrow\leftarrow\leftarrow$X$^1\Sigma_g^+$ transition. A rotational band analysis shows that the R(3) line of B” $^1\Sigma_u^+$ (v=2)$\leftarrow\leftarrow\leftarrow$X$^1\Sigma{+}_g$ (v=0) lies close to the three-photon energy, the next closest is P(2) of the D$^1\Pi_u^+$ (v=4)$\leftarrow\leftarrow\leftarrow$X$^1\Sigma_g^+$ (v=0) transition. The energy sum of three laser photons lies between the two peaks, ~25 cm^{-1} above B”(2’-0”)R(3) and ~30 cm^{-1} below D(4’-0”)P(2).

Spectroscopic studies [34, 38, 39] and theory [35] have shown that the dissociation rate of the D $^1\Pi_u^+$ (v=4) state is approximately 100 times higher than the B” $^1\Sigma_u^+$ (v=2) state. The linewidth for the J=2 of the D $^1\Pi_u^+$ (v=4) state [38] is 14.5 cm^{-1} and for the B” $^1\Sigma_u^+$ (v=2) state [39] J=1 0.3-0.7 cm^{-1} and J=2 < 0.2 cm^{-1}. Thus, while the intense short-pulse laser can have partial resonance overlap with the D $^1\Pi_u^+$ (v=4) state, resonance enhancement from the B” $^1\Sigma_u^+$ (v=2) state is unlikely. The lifetime for the D $^1\Pi_u^+$ (v=4) J=2 state is approximately 0.3 ps and is thus shorter than the laser pulsewidth of 0.5 ps or 5 ps.

Some experimental information is available on the photodissociation / ionization dynamics of H_2 following REMPI of the D state. Pratt *et al.* [26] at (3+1) REMPI from the ground electronic state via the D(v=0,1) states results primarily in H_2^+ ions the same vibrational state as the Rydberg precursor. Buntine *et al.* [25] found, however, that (1+1) REMPI via the 4pπ D $^1\Pi_u^+$ (v=2) state starting from the E,F $^1\Sigma_g^+$ (v=6) state yielded only H(n=3) atoms, although their experimental resolution was not sufficient to completely rule out other channels. The same authors also found that the product H^+ ions are ejected in a $\cos^2\theta$ distribution with respect to the laser polarization when the D state is excited via a P,R branch. For a simple $\Sigma \leftrightarrow \Pi$ transition a $\sin^2\theta$ distribution is expected, but as pointed out by Buntine *et al.* [25] and by Goa *et al.* [40], mixing of the B’ vibrational continuum with the Π^+ components produces a dominant parallel character in the transition. This same type of state mixing is expected to be even stronger for the D(v=4) levels [35].

Franck-Condon overlap of the D $^1\Pi_u^+$ Rydberg state with the H_2^+ ion is good for vibrational quantum number conserving transitions. This means that for direct ionization from the D state, ions should be formed mainly in the X $^2\Sigma_g^+$ (v^+=4). This behavior is also seen experimentally in REMPI studies of the 3pσ B' $^1\Sigma_u^+$, 4pπ D $^1\Pi_u^+$ (v=0,1) states [26] and the 3pπ C $^1\Pi_u^+$ state [16] excited by three-photon absorption from the ground electronic state. In our experiment no signal is seen at the equivalent H^+ position for H_2^+(v^+=4) that would indicate direct ionization of the D $^1\Pi_u^+$ (v=4) state. Instead, one of the most surprising observations in this study, a series of H_2^+ vibrational states peaking at v^+ = 2, 7 and 13 is observed. These peaks in the kinetic energy spectrum can only be attributed to one-photon dissociation of H_2^+ ionic levels.

The v^+=2 peak is strongest and it should also be noted from Fig. 8.1 that photoexcitation of the v^+=2 state to the A $^2\Sigma_u$ repulsive state has a very unfavorable Franck-Condon factor compared to dissociation of higher-lying vibrational states. It might be supposed that the B(v=2) state is responsible for the most intensity of this v^+=2 peak. The angular distributions for all three v^+ peaks, as discussed in the next section, however, are the same, which tends to rule out a mixed parentage for v^+=2.

The observed multi-mode H_2^+(v^+) distribution is indicative of extreme non-Franck-Condon behavior. Less extreme non-Franck-Condon behavior has been observed before experimentally for the C $^1\Pi_u$ (v=0-4) state [9, 16] and the D $^1\Pi_u$ (v=0,1) [26] and B' $^1\Sigma_u^+$ (v=0-2) [26] and the B' $^1\Sigma_u^+$ (v=4) [25]. This behavior has been theoretically treated by Chupka [41] and Hickmann [42] with the C $^1\Pi_u$ state of hydrogen as example. We have also seen similar multi-modal non Franck-Condon behavior in vibrational spacing in the photodissociation / ionization of O_2 with ps and fs pulses of 248 nm [43]. Chupka [41] and Hickmann [42] explain the non Franck-Condon effect in H_2 by the photoexcitation of a dissociating, autoionizing state. The time scale for autoionization is long enough for the nuclei to move, so the energy for dissociation can be transferred into the vibrational movement of the nuclei and therefore leaving the H_2^+ in different vibrational states. If the molecule did not autoionize during this dissociation pathway only dissociation into neutrals is possible. Note that in Fig. 8.3 no dissociation into neutrals at the fourth-photon level is seen, so no (four-photon excited) molecule survives autoionization. In the case of photodissociation of the D state one would expect that the major excited neutral hydrogen atoms formed correlate with the H(n=1)+H(n=3) limit. Even these pathways of special interest do not show up in the kinetic energy distributions of Fig. 8.3. It has recently been proven in other studies (Scheper *et al.* [14, 15]) of H_2 REMPI that the neutral dissociation channel, which has often been observed, can also arise by excitation of the Rydberg state to the vibrational continuum of higher lying (n>3) singly excited Rydberg states.

An important difference between our study and the previous REMPI studies through the D state is that short-pulse lasers are used and a higher vibrational level (v=4) (which is strongly predissociated) appears to be excited. Previous REMPI studies used nanosecond lasers and did not report REMPI above v=2. Indeed, an attempt to observe REMPI via D(v=4) with a nanosecond dye laser in our lab was not successful. Excitation via the higher vibrational level accesses higher energies in the doubly excited states, where new processes can take place. In particular, the total energy with four photons (19.87 eV) exceeds the dissociative ionization limit.

The excitation towards double excited states in our case could be as follows: the D state [$1\sigma_g$ $3p\pi_u^1\Pi_u$] can be core excited by the optically allowed transition $1\sigma_g \rightarrow 1\sigma_u$ that leaves the hydrogen in the double excited states Q_1 (in the nomenclature of Guberman [7]) in respectively the Q_1 $^1\Sigma_g^+$ and Q_1 $^1\Pi_g$. These states can either autoionize (dissociative or into different vibrational states of the ion) or dissociate in neutral excited hydrogen atoms.

Dastidar and Das [37] have theoretically treated the same process in H_2 following (3+2) REMPI via the B(v=4) state. While the intermediate state and the gerade-ungerade character differs from our study, the total energy is quite similar. Furthermore, the density of Q_1 states of gerade character is comparable to those of ungerade character treated by Dastidar and Das [37]. These authors were able to fully model the H^+ and photoelectron distributions measured experimentally by Rottke *et al.* [13]. Dastidar and Das [37] showed that autoionization, primarily via the Q_1 $^1\Sigma_g^+$ doubly excited state, gives rise to both dissociative ionization and vibrational autoionization with an extreme non Franck-Condon distribution. They were also able to account for oscillations in the dissociative ionization continuum which were observed by Rottke *et al.* [13].

In our study very weak peaks in the DI continuum are also seen (Fig. 8.3) at 0.2, 0.7, 1.2, and 1.7 eV, but considering the signal-noise ratio these can not be considered as quantitative evidence for oscillations. Dastidar and Das [37] predict equally spaced oscillations in the DI continuum which they assign to the structure in the overlap of the nuclear continuum wavefunction of the doubly excited state with that of the ionic ground state. More significantly for our study, extreme non FC behavior is also predicted by Dastidar and Das [37] for autoionization yielding $H_2^+(v^+)$.

As seen in Fig 8.3, the kinetic energy distributions are very similar for 0.5 ps and 5 ps pulses. Also quite striking is the relative signal for four-photon autoionization and three-photon dissociation is the same for both pulselengths. This indicates that competition between three-photon dissociation and further photoexcitation is not important. This may be expected if the three-photon excitation step is rate-limiting.

8.3.4 Angular distributions

The measured angular distributions are fitted to the expression of formula (8.1) and the corresponding anisotropy parameters for the main observed channels are presented in Table 8.1. The angular distribution for three-photon dissociation to form H(n=2) atoms at 0.28 eV, presented in Fig. 8.4, has higher order β values of $\beta_4 \approx 0$ and $\beta_6 \approx 0$, so it can be described with the one-photon expression using only β_2. The channels arising from one-photon dissociation of the hydrogen ion, however, have to be described with a two-photon expression, which suggests pre-alignment of the dissociating H_2^+ species. Therefore, a fit using β_2 and β_4 in formula (8.1) is shown. The according anisotropy parameters β_2 and β_4 are presented in Table 8.1 for the 0.5 ps and the 5 ps case.

For the three-photon dissociation channel (H(n=2) production) it was shown previously that the $D^1\Pi_u^+$ (v=4)$\leftarrow\leftarrow\leftarrow X^1\Sigma_g^+$ (v=0) P(2) transition is nearly resonant with the laser wavelength. Therefore we assume that the states occupied by the laser excitation are the B' vibrational continuum and the $D^1\Pi_u^+$ (v=4, J=1) state. The resulting product angular distribution will be a combination of the degree of mixing between the B' and D states and the finite lifetime of the D state. The transition to the B" continuum is parallel and direct dissociation yields β_2=2. While

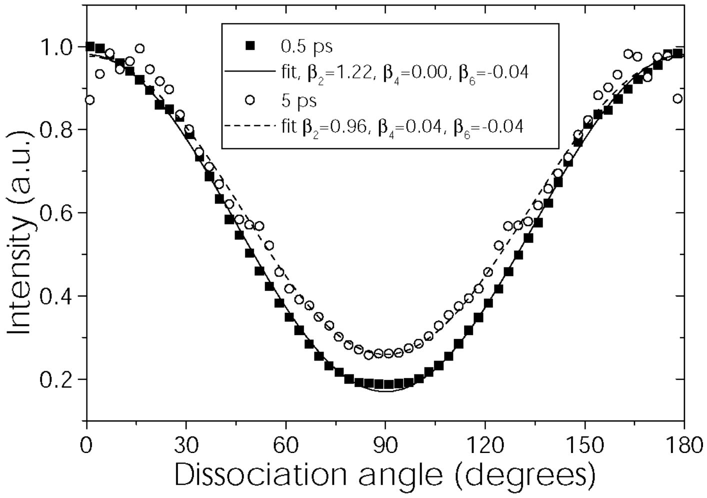

Figure 8.4: *Angular distributions for 248 nm three-photon dissociation of H_2 with 0.5 ps and 5 ps*

the D state has Π symmetry and is thus excited in a perpendicular transition, excitation of the D state via P,R branches, as in our experiment, is found to be predominately parallel [25] due to coupling with the B" continuum. The degree of coupling has not been calculated [35] for the D v=4 state, and a quantitative value of β was not reported in previous angular distribution measurements [25] for dissociation from this state. The D state lifetime is also not infinitely short, thus rotation could lower the β value for this transition as denoted in formula (8.2).

Table 8.1: *Measured angular distribution anisotropy parameters for 0.5 ps and 5 ps pulses.*

Peak	β_2@0.5 ps	β_4@0.5 ps	β_6@0.5 ps	β_2@5 ps	β_4@5 ps	β_6@5 ps
3-hν level	1.22±0.01	0.00±0.01	-0.04±0.01	0.96±0.01	0.04±0.01	-0.04±0.01
$H_2^+(v^+=2)$	2.39±0.06	0.74±0.04	n.a.	2.11±0.06	0.49±0.04	n.a.
$H_2^+(v^+=7)$	2.34±0.06	0.62±0.04	n.a.	1.98±0.10	0.62±0.08	n.a.
$H_2^+(v^+=13)$	2.39±0.10	0.60±0.07	n.a.	1.95±0.15	0.37±0.12	n.a.

The expected β_2 due to rotation of the $D^1\Pi_u^+$ (v=4, J=1) state can be estimated as follows. The expected anisotropy parameter β_{2calc} can be calculated using formula (8.2) and the experimental value of the lifetime determined previously for other rotational levels of the D state [38]. The angular rotation period T is needed in formula (8.2) and this is T= 4.38 ps for $D^1\Pi_u^+$ (v=4, J=1) using the spectroscopic constants of Herzberg [44] (B (v=4) = 23.9 cm^{-1}). Only a few specific J quantum state lifetimes have been measured for the D state, but it has been shown by several groups [35, 38] that the lifetime follows a J(J+1) lifetime dependency ascribed to Coriolis coupling. This J behavior is used to estimate the lifetime of other J states of the D v=4 state. The measured lifetime for the $D^1\Pi_u^+$ (v=4, J=2) τ=0.37 ps results in a calculated lifetime for the $D^1\Pi_u^+$ (v=4, J=1) of τ=1.11 ps. These data combined gives the anisotropy parameter of

β_{2calc}= 1.69 for $D^1\Pi_u^+$ (v=4, J=1). The values of β_2 in Table 8.1 (β_2@ 0.5ps=1.22, β_2@5ps= 0.96) are lower than that expected for a pure parallel transition with rotational predissociation. This suggests that β is determined mainly by the degree of coupling between the B' continuum and the D v=4 state.

A trend seen in Table 8.1 is that the angular distributions are more anisotropic for the 0.5 ps laser pulse than the 5 ps laser pulse. It has already been shown that the relative three-photon and four-photon yields are the same for both pulselengths. This suggests that the difference in the angular distributions is not due to competition between dissociation and photoexcitation at the three-photon level. Instead, an intensity-dependent process at the fourth photon level could be active. We have also seen this effect previously in O_2 [43] and CH_3I [45] photodissociation experiments with the short-pulse 248 nm laser. This behavior in angular distributions for H_2 dissociation can be ascribed, as in the other studies, to higher order effects caused by the interaction of the strong electric laser field with the molecular ion, resulting in an induced dipole moment creating pendular states. The molecules align with respect to the electric field vector due to libration of the internuclear axis about the laser polarization [46] resulting in higher values for the anisotropy parameters. This effect increases with increasing laser intensity, thus with decreasing laser pulsewidth. This is shown in Table I where the values of the anisotropy parameters are more extreme for the shorter pulsewidth.

8.4 Summary

The multiphoton excitation dynamics of H_2 with picosecond and femtosecond 248 nm pulses is characterized using velocity map imaging giving the full kinetic and angular distribution of the fragments. The primary event seen is three-photon excitation towards the D $^1\Pi_u^+$ (v=4) intermediate level which is mixed with the B' $^1\Sigma_u^+$ vibrational continuum. The D state dissociates towards the second neutral dissociation limit yielding H(n=1)+H(n=2). The degree of mixing appears to determine the product angular distribution following three-photon excitation. At the fourth-photon level autoionization from a doubly excited state leads to both dissociative ionization and a range of vibrationally excited hydrogen ions H_2^+ X $^2\Sigma_g^+$ (v^+=2,7,13) where v^+=2 is the strongest. This process is so fast that no hydrogen molecules survive autoionization, which prohibits dissociation into neutrals H(n=1)+H(n>1). Some evidence is also seen for oscillations in the dissociative ionization continuum, as predicted theoretically.

Acknowledgments

The authors thank Mr. Apostolis Egglezis for expert maintenance of the fs-ps KrF laser system. This work was done at the Ultraviolet Laser Facility at FORTH-IESL (TMR, Access to Large Scale Facilities EU program, Contract No. ERBFMGECT 950021) and was also supported by TMR Network *IMAGINE* ERB 4061 PL-97-0264 and the Stichting FOM. Helpful discussions with Prof. Wim van der Zande are also gratefully acknowledged.

References

[1] M.S. Pindzola and M. Dörr, Phys. Rev. A **43**, 439 (1991).
[2] K. Codling, L.J. Frasinski and P.A Hatherly, J. Phys. B **21**, L433 (1988).
[3] Y.L. Shao, D.J. Fraser, M.H.R. Hutchinson, J. Larsson, J.P Marangos and J.W.G. Tisch, J. Phys. B **29**, 5421 (1996).
[4] B. Yang, M. Saeed, L.F. DiMauro, A. Zavriyev and P.H. Bucksbaum, Phys. Rev. A **44**, R1458 (1991).
[5] D.W. Chandler and D.H. Parker, Adv. Photochem. **25,** 56 (1999).
[6] A. Guisti-Suzor, F.H. Miest, L.F. DiMauro, E.Charon and B. Yang, J. Phys. B **28**, 309 (1995).
[7] S.L. Guberman, J. Chem. Phys. **78**, 1404 (1983).
[8] S.T Pratt, P.M. Dehmer and J.L. Dehmer, J. Chem. Phys. **78**, 4315 (1983).
[9] E.Y. Xu, T. Tsuboi, R. Kachru and H. Helm, Phys. Rev. A **36**, 5645 (1987).
[10] J.W.J. Verschuur and H.B. van Linden van den Heuvell, Chem. Phys. **129**, 1 (1989).
[11] J.H.M Bonnie, J.W.J. Verschuur, H.J Hopman and H. B. van Linden van den Heuvell, Chem. Phys. Lett. **130**, 43 (1986).
[12] J. W.J. Verschuur, L.D. Noordam, J.H.M. Bonnie, and H.B. van Linden van den Heuvell, Chem. Phys. Lett. **146**, 283 (1988).
[13] H. Rottke, J. Ludwig and W. Sandner, J. Phys. B **30**, 4049 (1997).
[14] C.R. Scheper, W.J. Buma, C.A. de Lange and W.J. van der Zande, J. Chem. Phys. **109**, 8319 (1998).
[15] C.R. Scheper, C.A. de Lange, A. de Lange, E. Reinhold and W. Ubachs, Chem. Phys. Lett. **312**, 131 (1999).
[16] M.A. O'Halloran, S.T. Pratt, P.M. Dehmer and L.J. Dehmer, J. Chem. Phys. **87** , 3288 (1987).
[17] S.T Pratt, P.M. Dehmer and J.L. Dehmer, Chem. Phys. Lett. **105**, 28 (1984).
[18] S.T. Pratt, P.M. Dehmer and J.L. Dehmer, J. Chem. Phys. **87**, 4423 (1987).
[19] S.T Pratt, P.M. Dehmer and J.L. Dehmer, J. Chem. Phys. **85**, 3379 (1986).
[20] C. Cornaggia, D. Normand, J. Morellec, G. Mainfray and C. Manus, Phys. Rev. A **34**, 207 (1986).
[21] D. Normand, C. Cornaggia and J. Morellec, J. Phys. B **19**, 2881 (1986).
[22] E. Xu, A.P. Hickman, R. Kachru, T. Tsuboi and H. Helm, Phys. Rev. A **40**, 7031 (1989).
[23] E. Y. Xu, H. Helm and R. Kachru, Phys. Rev A. **39**, 3979 (1989).
[24] E.F. Cormack, S.T. Pratt, P.M. Dehmer and J.L. Dehmer, J. Chem. Phys. **98**, 8370 (1993).
[25] M.A. Buntine, D.P. Baldwin, and D.W. Chandler, J. Chem. Phys. **96**, 5843 (1992).
[26] S.T. Pratt, P.M. Dehmer and J.L. Dehmer, J. Chem. Phys. **86**, 1727 (1987).
[27] A.T.J.B Eppink and D.H. Parker, Rev. Sci. Instrum. **68**, 3477 (1998).
[28] R.N. Zare, Mol. Photochem. **4**, 1 (1972).
[29] K. Chen and E.S. Yeung, J. Chem. Phys. **72**, 4723 (1980).
[30] R.K. Sanders and K.R. Wilson, J. Chem. Phys. **63**, 4242 (1975).
[31] P.C. Samartzis, B.L.G. Bakker, T.P. Rakitzis, D.H. Parker and T.N. Kisopoulos, J. Chem. Phys. **110**, 5201 (1999).
[32] F.P. Schafer and S. Szatmari, Optics Comm. **68**, 196 (1988).

[33] S. Arai, T. Yoshimi, M. Morita, K. Hironka, T. Yoshida, H Koizumi, K. Shinsaka, Y. Hatano, A. Tagishita and K. Ito, Z. Phys. D **4**, 65 (1986).
[34] M. Glass-Maujean, J. Breton and P. M. Guyon, Z. Phys. D **5**, 189 (1987).
[35] H. Gao, J. Chem. Phys. **107**, 7278 (1997).
[36] N. Kouchi, M. Ukai and Y. Hatano, J. Phys. B **30**, 2319 (1997).
[37] K.R. Dastidar and R.K. Das, J. Chem. Phys. **112**, 3689 (2000).
[38] M. Glass-Maujean, J. Breton and P.M. Guyon, Chem. Phys. Lett. **63**, 591 (1979); M. Glass-Maujean, J. Breton and P.M. Guyon, ibid., **68**, 314 (1979).
[39] M. Rothschild, H. Egger, R.T. Hawkins, H. Pummer and C.K. Rhodes, Chem. Phys. Lett. **72**, 404 (1980).
[40] H. Goa, C. Jungen, and C.H. Greene, Phys. Rev. A, **47**, 4877 (1993).
[41] W. A. Chupka, J. Chem. Phys. **87**, 1488 (1987).
[42] A.P. Hickman, Phys. Rev. Lett. **59** , 1553 (1987).
[43] B.L.G. Bakker, D.H. Parker, P.C. Samartzis and T.N. Kitsopoulos, J. Chem. Phys. **112,** 5654 (2000).
[44] G. Herzberg, *Molecular Spectra and Molecular Structure, I. Spectra of Diatomic molecules;* Van Nostrand Reinhold Co: New York, (1950).
[45] P.C. Samartzis, B.L.G. Bakker, D.H. Parker, and T.N. Kitsopoulos, J. Phys. Chem. A **103,** 6106 (1999).
[46] B. Friedrich and D. Herschbach, Phys. Rev. Lett. **74**, 4623 (1995).

Chapter 9

Observation of direct dissociative ionization in molecular hydrogen

Abstract

Direct dissociative ionization is the simplest three-body break-up process in H_2. We describe the experimental verification of direct dissociative ionization by resolving the kinetic energy and angular distributions of the formed protons. A (2+1) REMPI process via the isotropic E,F $^1\Sigma_g^+$(v=6,J=0) level is employed. The structure in the kinetic energy spectrum is well described by a projection of the vibrational wave function of the E,F $^1\Sigma_g^+$(v=6,J=0) state onto the repulsive ionic state. The electronic character of the ionization continuum is revealed by the proton angular distribution.

9.1 Introduction

In excitation of molecular hydrogen above the H + H^+ dissociation limit molecular ions may be formed, or also two neutral H atom fragments, or three particles, an electron, proton and H atom, can be produced. This last process may involve two steps where the first step is the formation of a neutral doubly excited state from which molecular dissociation commences. The second step is then the autoionization of this dissociating state, forming an H- H^+ pair. Alternatively, dissociative ionization may be a direct process, in which H_2 is excited to the ionic dissociation continuum of H_2^+ (the $A^2\Sigma_u^+$ state). Dissociative photo-ionization, both *direct* and *indirect*, leads to three free particles (H,H^+,e^-). Hence, these processes are asymptotically non-distinguishable. Moreover, as the energy may be distributed over the three particles, neither the electron nor the heavy particle kinetic energy spectrum will reveal sharp distinctive structures. In order to distinguish the different three-body channels, it is thus necessary to obtain well-resolved kinetic energy *and* angular distributions of the ejected photo-fragments.

Photo-excitation of H_2 has been the subject of extensive experimental research using XUV one-photon excitation [1, 2, 3]. The introduction of strong laser systems made it possible to populate different intermediate high lying states via multiphoton excitation pathways, from which dissociation and ionization can be driven with less energetic photons. Experiments have been reported via the $B^1\Sigma_u^+$ state (using one or three photons) [4, 5] and via the E,$F^1\Sigma_g^+$ state (using two photons) [6, 7, 8]. Most theoretical treatments concentrated on ground state studies [9, 10, 11]. In many of these studies, doubly excited neutral states [12, 13] positioned in the ionization continuum have key roles, masking the observation of direct dissociative ionization.

In this letter we present kinetic energy distributions (KED) as well as the angular distributions (AD) of the protons formed in one-photon dissociative photo-ionization using the E,$F^1\Sigma_g^+$ (v=6,J=0) state as intermediate state. The oscillatory structure in the proton KED is explained only invoking *direct* dissociative ionization in the repulsive $A^2\Sigma_u^+$ state. The technique of velocity map imaging combines the simultaneous recording of KED and AD of the formed protons. Velocity map imaging has been used extensively in photodissociation studies, where fragments are ionized using multi-photon processes [14] . In this study, (2+1) resonant enhanced multiphoton dissociative ionization (REMP-DI) forms ions directly. In the following, we provide some details on the excitation step and the experimental setup followed by a description and discussion of the experimental results.

Figure 9.1 shows a potential diagram with the states of interest for this work. The E,F-state is shown as well as the first three doubly excited *ungerade* Q_1-states [12]. A condition for *direct* dissociative ionization with the first repulsive ionic state is a finite overlap with the H_2^+ $A^2\Sigma_u^+$ state. Starting from the ground state (equilibrium separation less then 0.1 nm) total excitation energies exceeding 25 eV are needed. By using the E,$F^1\Sigma_g^+$(v=6,J=0) state the internuclear separation in the H_2 molecule stretches from about 0.1 nm to 0.3 nm. This provides good Franck-Condon overlap factors to the repulsive ionic state with one 6.4 eV photon, allowing dissociative ionization. Photo-excitation from the E,F-state (see Figure 9.1) may also result in the formation of bound H_2^+ ions from the inner well region. The use of the rotationless J=0 level provides a complete isotropic intermediate population, facilitating the description of the AD of the resulting protons. The AD intensity I(θ) depends on the angle θ between the laser polarization direction and the velocity vector of the fragments and can be characterized [15] by one anisotropy parameter, β, which ranges between the limiting values -1 to 2. This parameter determines the symmetry of the transitions.

9.2 Experimental

The velocity map imaging apparatus used has already been described in detail elsewhere and a summary of the experimental details will be given here. A pulsed supersonic beam of pure H_2 is directed down the axis of a time-of-flight (TOF) mass spectrometer, and crossed at right angles by the counter propagating laser light of a line-narrowed ($\delta\nu \approx 0.5$ cm^{-1}) [16] tunable ArF excimer laser set on the E,F$^1\Sigma_g^+$(v=6,J=0)$\leftarrow\leftarrow$X $^1\Sigma_g^+$(v=0,J=0) two-photon transition in hydrogen. A subsequent photon can then excite the hydrogen above the H^+ + H dissociation limit at a total photon energy of 19.26 eV, forming protons. The 193 nm light (15 ns pulse width, 25 mJ per pulse) was focussed on to the molecular beam resulting in an intensity of $\approx 5\cdot 10^{10}$W/cm^2. The laser light was more than 99% vertically polarized. The formed protons were extracted from the ionization region into the grounded time-of-flight tube and detected onto a two-dimensional micro channel plate/phosphor screen detector read by a CCD camera. Mass selectivity was achieved by increasing the gain of the detector when the H^+ ions arrive. The image (sum of 25000 shots) is inverted (from the two dimensions of the detector to all three spatial dimensions) using an inverse Abel transformation. This is possible because of the presence of a symmetry axis (the polarization direction of the light, vertical to the TOF axis, parallel to the detector

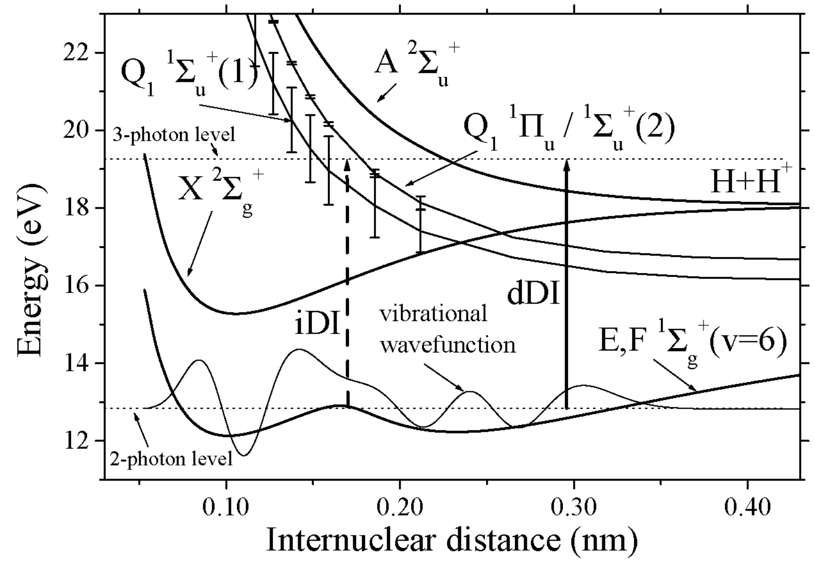

Figure 9.1: *Schematic potential energy diagram. The E,F potential is from Ref. [20]. The doubly excited states are presented including their autoionization linewidths as error bars, taken from Tennyson [13]. Also shown is the vibrational wave function of the intermediate state at the 2-photon level. The vertical arrows represent indirect Dissociative Ionization (iDI, dashed) and direct Dissociative Ionization (dDI, full) at the 3-photon level.*

surface). We note that even in the narrow band mode the laser intensity still consists out of 50% narrow band light on top of broad band background. Hence, the third-(one) photon step will be "polluted" with a broad band component. The resolution (ΔKE/KE) of the apparatus can be as high as 2% [14]. The excimer laser used has an unfavorable rectangular beam shape, resulting in a decreased resolution with a value of $\Delta E/E \approx 8\%$ [16].

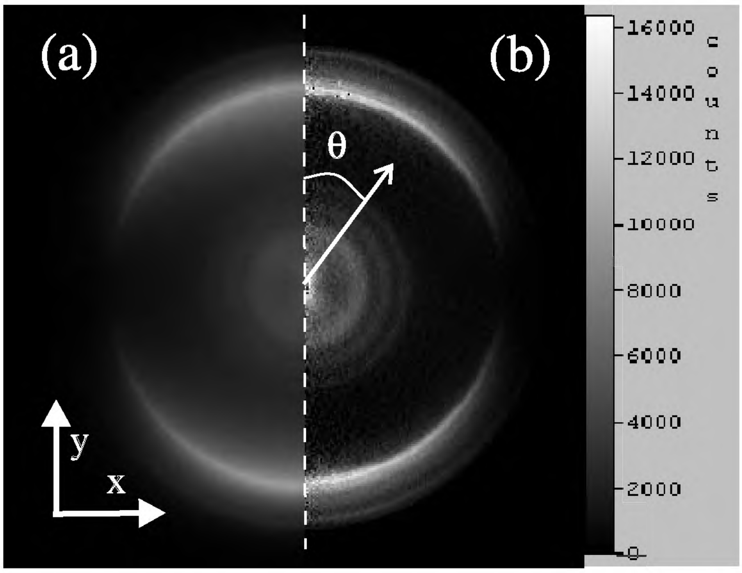

Figure 9.2: *(a) Measured image. (b) Abel transformed image. The angle θ is between the dotted line (presenting the laserpolarization) and the fragments. On the right side a intensity greyscale is presented*

9.3 Results and discussion

As mentioned above, after three-photon absorption at 19.26 eV, the hydrogen molecule can decay in three major pathways: dissociation into two neutrals (D), ionization forming an H_2^+ ion (I) and *direct* or *indirect* dissociative ionization (DI). For dissociative ionization (DI) the maximum kinetic energy release over the fragments is determined by the ionic dissociation limit at 18.07 eV and is therefore 1.19 eV (0.6 eV per fragment). In *direct* dissociative ionization the electron also carries away kinetic energy. Hence, the H^+ ions are expected in the energy range from 0 to 0.6 eV. In the case of molecular dissociation (D), a ground state H-atom is formed together with an excited fragment. These excited atoms are partially ionized by the strong 6.42 eV laser light. Their kinetic energy is determined by the dissociation limit of H(n=1)+H(n>1)and will have discrete values between 0.6 eV (H(n=∞)) and 2.29 eV (H(n=2)). Molecular ionization (I) produces initially, H_2^+ $X^2\Sigma_g^+$ (v^+) + e^-. The energy of the photon allows H_2^+ to be formed in all v^+ levels. A fraction of these molecular ions can be photo-dissociated, again yielding a proton. The kinetic energy of the protons is determined by the initial vibrational level, and ranges from 1.88 eV to 3.2 eV. Hence, in an energy resolved KED spectrum all pathways are distinguishable.

A measured image is presented in Figure 9.2 . The intensity of the signal from low to high corresponds to from black to white as denoted in the greyscale in Figure 9.2 . The direction of the laser polarization is along the y-axis. The image clearly shows rings with relatively large diameter (high KE values) and three fainter rings with small diameters (low KE values). The angular distribution can be observed directly. The outer rings show an intensity peaking along the laser polarization in accord with a $\cos^2\theta$ angular distributions (β=2) as expected for the $A^2\Sigma_u^+ \leftarrow X^2\Sigma_g^+$ ionic dissociation process. The inner rings are more isotropic. In the Figures 9.3 and 9.4 , these data are transformed into a KED (plotting the intensity as function of the radius of the ring) and into an AD (as function of θ for selected rings). Figure 9.3(a) reveals the full range and all three processes. Figure 9.3(b) concentrates on the energy region for DI. Structures are seen both in the DI region and the I-region. The structure in the ionization region (I) matches photodissociation of the hydrogen ion formed in a distribution peaked at the H_2^+ $X^2\Sigma_g^+$ (v^+=2) and H_2^+ $X^2\Sigma_g^+$ (v^+=13) states. Their production is enhanced in accord with the v^+ dependent Frank-Condon factors with the E,F(v=6) level. This has been seen in photo-electron spectra (the complement of our KED) by Xu *et al.* [7]. No evidence is found for the formation of H(n≥3) fragments from the dissociation (D) process. The H(n=2) could be hidden below the I-peak. Also Xu *et al.* [7] found no evidence for formation of excited H atoms due to dissociation [7]. Important for the discussion later, the absence of D-fragments suggests that the doubly excited states do not play a dominant role at this wavelength. The signal in the DI-region below 0.7 eV

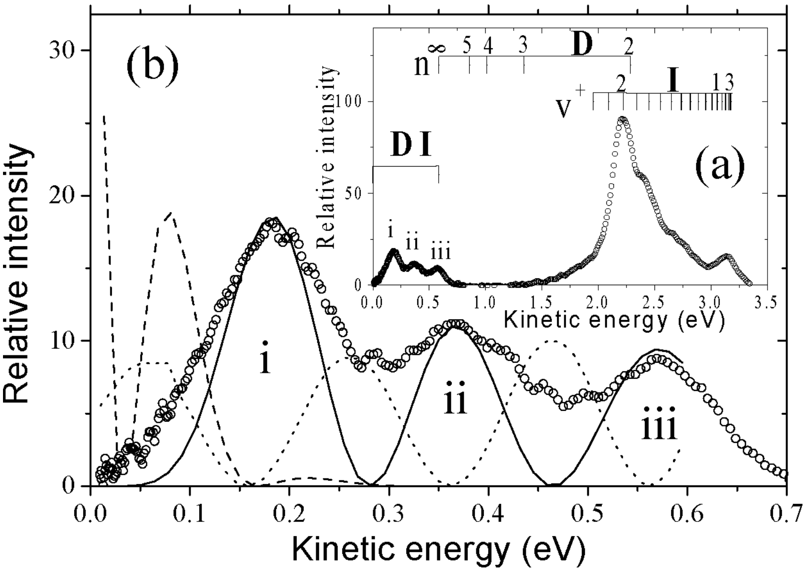

Figure 9.3: *Kinetic energy distributions. (a) The inset shows the full energy region, revealing DI, and I. (b) The main figure shows the region below 0.7 eV. A small background due to the inverse Abel transformation has been subtracted. The three peaks in the DI region are denoted with i,ii, and iii. The measured KED is presented by open circles (o o o). The lines are calculated KED distributions using different models. (——) Solid line (direct DI via the A-state), Dashed line (— — —) (direct DI via the X-state) (· · ·) Dotted line (approximate indirect DI via $Q_1\,^1\Pi_u$).*

in Figure 9.3 shows oscillatory structure, which cannot be assigned to known states or known dissociation limits. In the following we argue that this structure is the consequence of a *direct* DI process. Xu *et al.* [7] did not report oscillations in their photo electron spectrum, being not sensitive in the associated photo-electron energy region. The possible DI processes can be summarized as follows. From the E,F(v=6) state, the following states are one-photon allowed: the doubly excited $Q_1\ {}^1\Sigma_u^+$ and ${}^1\Pi_u$ states and the ionic dissociative continua of the $X^2\Sigma_g^+$ and $A^2\Sigma_u^+$ states. At the internuclear separations in the outer 'F'-well, the electron configuration of the E,F-state is dominated by the $(2p\sigma_u)^2$ configuration. As a consequence, at these internuclear separations excitation to the ionic $A^2\Sigma_u^+$ $[(2p\sigma_u)]$, and to the doubly excited ${}^1\Sigma_u^+[(2p\sigma_u)(2s\sigma_g)$, and $(2p\sigma_u)(3d\sigma_g)]$ and ${}^1\Pi_u[(2p\sigma_u)(2d\pi_g)]$ are all one-electron transitions. The process of *direct*

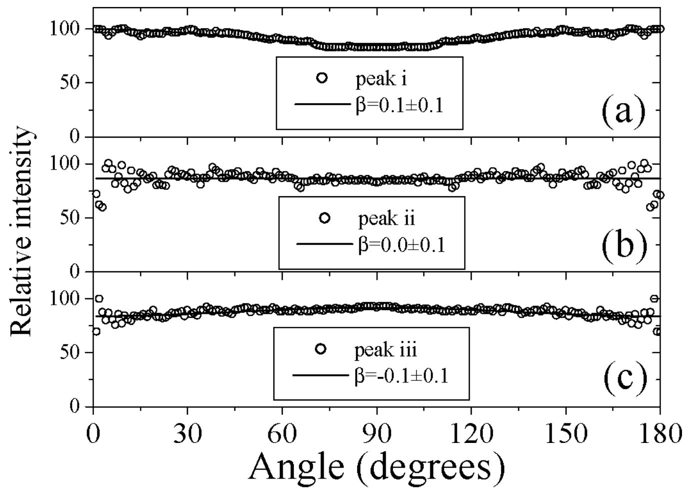

Figure 9.4: *Angular distributions for peaks i,ii and iii of Figure 9.3 . The observed distributions are fit using* $I(\theta)\propto 1+\beta P_2(\cos\theta)$, *where* $P_2(\cos\theta)=\frac{1}{2}[3\cos^2\theta-1]$ *is the second-order Legendre polynomial.*

DI leads to a KED of the proton given by $I(E_P)=P_{el}(E_{tot}-2E_P)\times \mid \langle\chi_{EF^2\Sigma_g^+}(R)\mid\chi_{A^2\Sigma_u^+}(R;2E_p)\rangle\mid^2$, with $P_{el}(E_{el})$ describing the probability of generating a photo-electron with energy E_{el}, E_{tot} is the three photon energy. This function has been approximated by the H(1S) photoionization curve which is finite at threshold, and then slowly decreasing with electron energy [17]. The factor 2 (in $2E_P$) comes from the fact that the kinetic energy is equally divided over the H and H^+ fragments. . As mentioned, the photons couple the outer (F) well with the dissociative ionization continuum in a one-electron transition $(2p\sigma_u \rightarrow \varepsilon(s \text{ or } d)\lambda_g)$. We therefore assume the excitation probability to be independent of internuclear separation. Figure 9.1(b) shows, a remarkably good agreement (solid line). The position and shape of the v=6 vibrational level is found by numerically solving the Schrödinger Equation using a Numerov method. The same procedure has been used to determine the FC factors.

The period and relative amplitude of the oscillations are well reproduced. However, the experimental results are not completely reproduced. We note that the loss of structure is due to the finite resolution of the apparatus due to an unfavorable laser beam geometry. The discrepancy could also be attributed to an alternative ionization pathway, such as *direct* DI into the continuum of the ionic ground state, or *indirect* DI via the doubly excited states. The former process has much smaller FC-factors in combination with a very different energy dependent behavior (see dashed line in Fig 9.1(b)). The second alternative may be autoionization of the [(2pσ_u)(2sσ_g) and (2pσ_u)(3dσ_g)] ${}^1\Sigma_u^+$ states and the [(2pσ_u)(3dπ_g)] ${}^1\Pi_u$ Q_1-states [12, 13]. Tennyson [13] has reported auto-ionization widths of all these states. The lowest ${}^1\Sigma_u^+$ state has a very large autoionization width ($\Gamma > 1$ eV) and will autoionize nearly completely before dissociation. The other two will predominantly dissociate into high H(n) fragments. The exact calculation of the auto-ionization signature is complicated, in that it has to treat autoionization and dissociation on an equal footing (see e.g. in Refs [10, 18]. It should be noted that oscillations in proton KED spectra using the $B^1\Sigma_u^+$ state as platform [5] have been assigned to autoionizing doubly excited states [18]. Exact calculations of this process for the E,F state is beyond the scope of this work. The limiting cases can be estimated, however. The case of slow autoionization is appropriate for the second ${}^1\Sigma_u^+$ and first ${}^1\Pi_u$ state. The KED is given by the FCF between the dissociative continuum states in the $Q_1\,{}^1\Pi_u\backslash{}^1\Sigma_u^+$ at the three-photon level and the H_2^+ $X^2\Sigma_g^+$ state at variable energy ($2E_p$) [19]: $I(E_p) \simeq \mid \langle \chi_{Q_1}(R;3h\nu) \mid \chi_{XH_2^+}(R;2E_p)\rangle \mid^2$ Figure 9.1(b) shows the results for all three doubly excited states, revealing a clear mismatch with experiment. As mentioned before, the absence of neutral (and ionized) H(n>2) fragments in the spectrum (process D), already suggest that these doubly excited states do not dominate. The case of very fast autoionization pertains to the lowest ${}^1\Sigma_u^+$ state, (see Figure 9.1). Here the structure is similar to the calculated *direct* DI to the ionic ground state.

Only one curve in Figure 9.3(b) describes the experiments satisfactorily, namely *direct* dissociative ionization to the continuum of the electronically excited ionic state. The oscillations then reflect the behavior of the wave function of the outer well (F-side) of the E,F ${}^1\Sigma_g^+$ (v=6,J=0) state. In the following we further corroborate this interpretation with the expected angular behavior. The angular distributions of the three dissociative ionization peaks i, ii and iii are presented in Figures 9.4(a), 9.4(b) and 9.4(c) respectively, along with the fitted angular distribution $I(\theta)$ and the associated β values. These values are around 0, *a priori* surprising in the case of one-photon bound-free transitions, where limiting values are expected. The *direct* DI transition is $A^2\Sigma_u^+$ [(2pσ_u, ε(s or d)λ_g)]$\leftarrow F^1\Sigma_g^+$ [(2pσ_u)^2]. Theoretically the angular distribution is easily estimated. The initial state is the rotationally completely isotropic ${}^1\Sigma_g^+$ (J=0) state. In the case of s-wave character of the continuum electron, the nuclei carry the angular momentum of the dipolar excitation. This would indeed lead to a purely parallel of β=2 parameter as follows from elementary angular momentum algebra. [15] In the case of the continuum electron being a d-wave, the electron carries away the photon angular momentum leading resulting in a β-parameter of β=0.2. In both cases, the dissociation continuum consists of one rotational state only, being the N^+=1 state. We note that the N^+=0 and N^+=2 states are not possible as ortho-hydrogen is not converted into para-hydrogen and *vice versa*. Finally, it is possible for the d-electron to leave the H_2^+ core with three units of angular momentum (N^+=3). This channel would give an angular distribution characterized by $\beta \approx 0.8$, but is expected to be weak on dynamical grounds.

The observed angular distributions are very close to β=0.2. We conclude that in *direct* DI the ion is left in a dissociative state with N^+=1 (note: N^+ is not an observable) and that a d-wave electron is emitted. Indeed, it is well known that atomic like *p-d* transitions are 30 times stronger than *p-s* transitions. The small discrepancy between the β=0.2 and the observed slightly negative values may be attributed to instrumental effects connected to the background subtraction. Excitation of the autoionizing $^1\Pi_u$ doubly excited state would reduce the anisotropy parameter, as this adds perpendicular (β=-1) character. This effect is diminished by the simultaneous parallel excitation to the $^1\Sigma_u$ state. The associated KED does not fit, however, and it has been argued before that this channel is unlikely because of the absence of detectable neutral H(n=3) fragments. In conclusion, we have shown that oscillatory structure directly reflecting the outer well vibrational wave function of the E,F state in *direct* dissociative ionization of H_2. This identification of this process is further corroborated by the angular distributions of the observed protons. Hence, two continua are simultaneously excited, with a resulting structure in the KED and also in the associated photo-electron spectra characteristic of direct dissociative ionization.

Acknowledgments

This work was part of the research program of the “Stichting voor Fundamenteel Onderzoek der Materie (FOM)” and is financially supported by the “Nederlandse Organisatie voor Wetenschappelijk Onderzoek (NWO)”. The authors thank M.C. van Beek, N.J. Dam and J.J. ter Meulen for help and use of the tunable excimer laser. The authors also thank C. Sikkens and C. Timmer for technical support. Dr. F. Robicheaux is thanked for clarifying discussions.

References

[1] S. Strathdee and R. Browning, J. Phys. B **12** , 1789 (1979).
[2] K. Ito, R.I. Hall, and M. Ukai, J. Chem. Phys. **104**, 8449 (1996).
[3] Z.X. He, J.N. Cutler, S. H. Southworth, L.R. Hughey, and J.A.R. Samson, J. Chem. Phys. **103**, 3912 (1995).
[4] J.W.J. Verschuur and H.B. van Linden-van den Heuvell, Chem. Phys. **129**, 1 (1989).
[5] H. Rottke, J. Ludwig, and W. Sandner, J. Phys. B **30**, 4049 (1997).
[6] S. Yang, and W.T. Hill III, Phys. Rev. **51**, 2301 (1995).
[7] E. Xu, A.P. Hickman, R. Kachru, T. Tsuboi, and H. Helm, Phys. Rev. **40**, 7031 (1989).
[8] W.T. Hill III, B.P. Turner, S. Yang, J. Zhu, and D.L. Hatten, Phys. Rev. **43**, 3668 (1991).
[9] A.P. Hickman, Phys. Rev. Lett. **59** , 1553 (1987).
[10] K. Kirby, T. Ulzer, A.C. Allison, and A. Dalgano, J. Chem. Phys. **75**, 2820 (1981).
[11] F. Sánchez and F. Martín, Phys. Rev. Lett. **79**, 1654, (1997).
[12] S.L. Guberman, J. Chem. Phys. **78**, 1404 (1983).
[13] J. Tennyson, Atomic and Nuclear Data Tables **64**, 253 (1999).
[14] A.T.J.B Eppink and D.H. Parker, Rev. Sci. Instrum. **68**, 3477 (1998).
[15] R.N. Zare, Mol. Photochem. **4**, 1 (1972).
[16] B.L.G. Bakker and D.H. Parker, J. Chem. Phys. **112**, 4037 (2000).
[17] T.F. Gallagher, *Rydberg atoms*, (Cambridge Univ. Press, 1994) p.41
[18] K.R. Dastidar and R.K. Das, J. Chem. Phys. **112**, 3689 (2000).
[19] This FC-factor does not converge but oscillates. The mean value of this oscillation is used.
[20] L. Wolniewicz and K. Dressler, J. Chem. Phys. **100**, 444 (1994).

Samenvatting

In dit proefschrift worden fotofragmentatieprocessen bestudeerd bij moleculen, die met verschillende soorten licht worden geëxciteerd. Hierbij wordt gebruik gemaakt van de “Velocity Map Imaging” techniek, oftewel de “snelheidsafbeelding” methode, waarbij een afbeelding (ook wel image genoemd) wordt gemaakt van het fragmentatieproces. De waargenomen fotofragmentatieprocessen spelen een belangrijke rol bij de fotochemie in verbrandingsprocessen, in de atmosfeer en in de ruimte. De initiële snelheidsverdeling van de fragmenten wordt geprojecteerd op een detector, waarbij een afbeelding ontstaat die de snelheids- en hoekverdeling van de ontstane fragmenten bevat. Met deze snelheidsverdeling kan achterhaald worden hoeveel fotonen het molecuul heeft geabsorbeerd en naar welke dissociatielimieten het uiteen is gevallen. De hoekverdelingen vertellen iets over de symmetrie van de fotonovergangen. Als deze hoekverdelingen niet-extreme waarden aannemen, kan men deze eigenschappen gebruiken om de levensduur van de aangeslagen toestand af te schatten.

In hoofdstuk 2 wordt een studie naar de fotodissociatie van het molecuul chloor ($\mathrm{Cl_2}$) beschreven, waarbij de dissociatiegolflengte van het licht varieert van 310 nm tot 410 nm. Het molecuul kan uiteenvallen via de repulsieve $1_u(^1\Pi_u)$ toestand, die twee grondtoestand chloor atomen $\mathrm{Cl_2}(^2P_{3/2})$ oplevert of via de $0_u^+(\mathrm{B}^3\Pi_u)$, dat resulteert in zowel een chlooratoom in de grondtoestand $\mathrm{Cl_2}(^2P_{3/2})$ als een geëxciteerd atoom $\mathrm{Cl_2}(^2P_{1/2})$. De hoek- en snelheidsverdelingen van elk van beide zijn gemeten. Hiermee is de onderlinge interactie van de $1_u(^1\Pi_u)$ toestand met de $0_u^+(\mathrm{B}^3\Pi_u)$ toestand bepaald. Er is tevens waargenomen, dat er een gemiddelde voorkeursrichting voor de chlooratomen in de grondtoestand bestaat.

De hoofdstukken 3 en 4 behandelen de fotodissociatie van het molecuul stikstofmonoxide (NO). In hoofdstuk wordt 3 bekeken hoe het molecuul predissocieert nadat het, via de $\mathrm{A}^2\Sigma^+$ geëxciteerd te zijn geweest, nog een lichtdeeltje absorbeert. Hierbij zijn de eerste en de derde dissociatielimieten geobserveerd via het gemeenschappelijke fragment, het zuurstofatoom in de grondtoestand ($\mathrm{O}(^3P_2)$). Deze metingen correleren met respectievelijk het grondtoestand stikstofatoom ($\mathrm{N}(^4\mathrm{S})$) en het aangeslagen stikstofatoom ($\mathrm{N}(^2\mathrm{D})$). De laatste is gedetecteerd en vergeleken met het resultaat van het zuurstofatoom.

In hoofdstuk 4 wordt de predissociatie van NO gekarakteriseerd na de absorptie van twee fotonen van circa 275 nm. In dit energiegebiedje worden de hoek- en snelheidsverdelingen bepaald van zuurstofatomen in de grondtoestand, die correleren met de belangrijke eerste en derde dissociatielimieten van NO: respectievelijk de stikstofatomen in de grondtoestand en aangeslagen stikstofatomen. Hierbij is de verhouding van deze twee limieten bepaald over het gescande golflengtegebied. Ook zijn de hoekverdelingsparameters van deze fragmenten bepaald.

Hoofdstuk 5 behandelt de fotofragmentatie van een isotoop van het molecuul koolstofmonoxide ($^{13}\mathrm{C}^{16}\mathrm{O}$). Hierbij is gebruik gemaakt van een afstembare ArF excimer laser, die licht maakt met een golflengte rond de 193 nm. Dit licht is resonant met de $\mathrm{a}^3\Pi(\mathrm{v}{=}2)\leftarrow\mathrm{X}\ ^1\Sigma^+(\mathrm{v}{=}0)$

overgang in het molecuul en twee 193 nm fotonen zijn resonant met een overgang in het aangeslagen koolstofatoom C(^{1}D). Dit laatste gegeven wordt gebruikt om deze atomen te detecteren, via het resonante foto-ionisatie proces. De waarneming van een minder extreme β_2^2 kan verklaart worden met een predissociatie van een Rydberg toestand op het niveau van twee fotonen.

Door middel van hetzelfde soort licht dat gebruikt werd in het vorige hoofdstuk, wordt in hoofdstuk 6 de atmosferisch relevante Schumann-Runge band geëxciteerd in moleculair zuurstof (O_2). Hierbij wordt het zuurstofatoom in de grondstoestand (O($^3P_2$)) gedetecteerd. De gemeten hoekverdelingen van deze fragmenten worden gebruikt om de daaruit volgende levensduren van de $B^3\Sigma_u^-$(v=4) toestand te vergelijken met literatuurwaarden, waarbij de overeenstemming goed was. Ook is met behulp van deze meting een gemiddelde waarde verkregen van β=0.48 voor het onderliggende Herzberg continuüm. De gemeten snelheidsverdelingen, als functie van de excitatielasergolflengte, geven bepaalde resonanties weer die overeenkomen met eerdere gemeten spectra. Deze onverklaarbare resonanties worden in dit proefschrift toegeschreven aan componenten van de nsσ_g(n-1)dπ_g $^1\Sigma_g^+$ Rydberg reeksen. Ook vindt er op het energieniveau van twee fotonen ionisatie plaats, waarbij de gevormde moleculaire zuurstof-ionen met één en twee fotonen worden gefotodissocieert.

In de volgende twee hoofdstukken is gebruik gemaakt van een KrF excimer laser die 248 nm licht geeft met een pulsduur van 0.5 ps of 5 ps. In hoofdstuk 7 wordt dit licht toegepast om moleculair zuurstof te fotofragmenteren. Hierbij worden de hoek- en snelheidsverdelingen gemeten, van de bij dit proces ontstane elektronen en geïoniseerde zuurstof atomen. De geobserveerde fragmentatieprocessen vinden voornamelijk plaats op het energieniveau van vier fotonen. Hierbij is zowel post-dissociatieve ionisatie als autoionisatie, een belangrijk proces. Bij het eerste proces ontstaan zuurstofatomen in de grondtoestand tezamen met extreem aangeslagen zuurstofatomen die auto-ioniseren naar de gedetecteerde zuurstof-ionen. Het tweede proces creëert moleculaire zuurstof-ionen in verschillende vibrationele toestanden, die op hun beurt weer fotodissocieren via absorptie van één of twee fotonen. Hierbij wijken de 5 ps en 0.5 ps resultaten van elkaar af, wat toegeschreven kan worden aan de verschillen in overgangen binnen het ion.

Deze speciale 248 nm lichtbron wordt in hoofdstuk 8 gebruikt om de fotofragmentatie van moleculair waterstof (H_2) te onderzoeken. Hierbij worden drie belangrijke fotofragmentatie processen geconstateerd. Ten eerste blijkt het waterstofmolecuul te predissociëren op het energieniveau van drie fotonen. Ten tweede vindt er na absorptie van vier fotonen dissociatieve ionisatie plaats. Tenslotte vindt op hetzelfde energieniveau directe en indirecte ionisatie plaats. Dit resulteert in een vibrationele distributie van het waterstof ion, dat piekt op v^+=2,7,13. Dit gedrag wordt toegeschreven aan de dubbel aangeslagen toestanden van waterstof.

In het laatste hoofdstuk wordt directe dissociatieve ionisatie van moleculair waterstof geobserveerd. Hiertoe wordt het waterstofmolecuul geëxciteerd met licht afkomstig van de eerder genoemde afstembare ArF laser. Dit licht is met twee fotonen resonant met een hogere toestand in het waterstofmolecuul, namelijk de E,F $^1\Sigma_g^+$(v=6,J=0) toestand. Een derde foton brengt het molecuul in energie hoger dan de dissociatie limiet van het ion, zodat vele fragmentatie processen energetisch mogelijk zijn. Zo worden de protonen gedetecteerd die afkomstig zijn van de fotodissociatie van daarvoor gefoto-ioniseerde moleculen in verschillende vibrationele toestanden. Een verrassende observatie is het bestaan van directe dissociative ionisatie dat verklaard kan worden met de eigenschappen van de tussenliggende E,F $^1\Sigma_g^+$(v=6,J=0) toestand.

Curriculum Vitae

Op 21 december 1973 ben ik geboren in Nijmegen. Mijn middelbare school periode heb ik doorgebracht op de Scholengemeenschap “Oost-Betuwe” te Bemmel, waar ik mijn Atheneum diploma behaalde. Hierna ging ik in 1992 Natuurkunde studeren aan de Katholieke Universiteit Nijmegen. In februari 1996 begon ik met mijn afstudeerstage bij de afdeling Molecuul- en Laserfysica aan de velocity map imaging opstelling van André Eppink en Prof. David Parker. Ik studeerde af als experimenteel natuurkundige in mei 1997. De maand erna ben ik begonnen als OIO (Onderzoeker In Opleiding) werkzaam via Stichting FOM (Fundamenteel Onderzoek der Materie) op het velocity map imaging onderzoek. Ik bestudeerde tevens in mei 1998 fotofragmentatieprocesssen van kleine moleculen op het FORTH instituut te Heraklion (Griekenland), waarbij ik gebruik maakte van lasers met een korte pulsduur.

Publications

- Chapter 2
  Spin-orbit branching ratios for the Cl atom photofragments following the excitation of Cl_2 *from 310 to 470 nm*
  P.C. Samartzis, B.L.G. Bakker, T.P. Rakitzis, D.H. Parker, T.N. Kitsopoulos,
  J. Chem. Phys. **110**, 5201 (1999).

- Chapter 3
  The sequential two-photon dissociation of NO as a source of aligned $N(^2D)$, $N(^4S)$ *and* $O(^3P)$ *atoms*
  B.L.G. Bakker, A.T.J.B. Eppink, D.H. Parker, M.L. Costen, G. Hancock, G.A.D. Ritchie,
  Chem. Phys. Lett. **283**, 319 (1998).

- Chapter 4
  Two-photon dissociation of NO near 275 nm investigated by velocity map imaging
  B.L.G. Bakker, D.H. Parker, G. Hancock, G.A.D. Ritchie
  Chem. Phys. Lett. **294**, 565 (1998).

- Chapter 5
  Photodissociation dynamics of $^{13}C^{16}O$ *excited by 193 nm light*
  B.L.G. Bakker and D.H. Parker,
  Chem. Phys. Lett. **330**, 293 (2000).

- Chapter 6
  Photophysics of O_2 *excited by tunable laser radiation around 193 nm*
  B.L.G. Bakker and D.H. Parker,
  J. Chem. Phys. **112**, 4037 (2000).

- Chapter 7
  Nonresonant photofragmentation/ionization dynamics of O_2 *using picosecond and femtosecond laser pulses at 248 nm*
  B.L.G. Bakker, D.H. Parker, P.C. Samartzis and T.N. Kitsopoulos,
  J. Chem. Phys. **112**, 5654 (2000).

- Chapter 8
  Multiphoton dynamics of H_2 *with 248 nm picosecond and femtosecond pulses*
  B.L.G. Bakker and D.H. Parker,
  J. Chem. Phys. **113**, 9044 (2000).

- Chapter 9
  Observation of direct dissociative ionization in molecular hydrogen
  B.L.G. Bakker, D.H. Parker and W.J. van der Zande,
  submitted to Phys. Rev. Lett.

- *Velocity imaging - applications in molecular oxygen photophysics*
  A.T.J.B. Eppink, B.L.G. Bakker and D.H. Parker,
  SPIE Vol. **3271** 177 (1998).

- *Photoelectron and photofragment velocity imaging following the excitation of* CH_3I *to the A-band using fs, ps and ns laser pulses*
  P.C. Samartzis, B.L.G. Bakker, D.H. Parker and T.N. Kitsopoulos,
  J. Phys. Chem. **103**, 6106 (1999).

- *Completely inverted ClO vibrational distribution from* $OClO(^2A_2$ *24,0,0)*
  R.F. Delmdahl, B.L.G. Bakker and D.H. Parker,
  J. Chem. Phys. **112**, 5298 (2000).

- *Crossed-beam velocity map imaging of collisional autoionization processes*
  R.F. Delmdahl, B.L.G. Bakker and D.H. Parker,
  J. Chem. Phys. **113**, 7728 (2000).

- *Photodissociation of hydrogen iodide in the A-band region 272 nm - 288 nm*
  S. Manzhos, H.-P. Loock, B.L.G. Bakker and D.H. Parker,
  accepted for Can. J. Phys.

- *Photodissociation of superexcited states of hydrogen iodide: A photofragment imaging study using resonant multiphoton excitation at 13.39 eV and 15.59 eV*
  H.-P. Loock, B.L.G. Bakker and D.H. Parker,
  submitted to J. Chem. Phys.

- *Velocity map imaging: technique and applications to* O_2 *photodissociation.*
  D.H. Parker, B.L.G. Bakker, R.F. Delmdahl, T. Berg and A.T.J.B. Eppink,
  ACS Symposium Series 770; Imaging in Chemical Dynamics (American Chemical Society, Washington DC), 56 (2000).